

---

Electronic Thesis and Dissertation Repository

---

8-29-2016 12:00 AM

# Evaluation of the UAV-Based Multispectral Imagery and Its Application for Crop Intra-Field Nitrogen Monitoring and Yield Prediction in Ontario

Yang Song  
*The University of Western Ontario*

Supervisor  
Jinfei Wang  
*The University of Western Ontario*

Graduate Program in Geography  
A thesis submitted in partial fulfillment of the requirements for the degree in Master of Science  
© Yang Song 2016

Follow this and additional works at: <https://ir.lib.uwo.ca/etd>



Part of the [Remote Sensing Commons](#)

---

## Recommended Citation

Song, Yang, "Evaluation of the UAV-Based Multispectral Imagery and Its Application for Crop Intra-Field Nitrogen Monitoring and Yield Prediction in Ontario" (2016). *Electronic Thesis and Dissertation Repository*. 4085.  
<https://ir.lib.uwo.ca/etd/4085>

This Dissertation/Thesis is brought to you for free and open access by Scholarship@Western. It has been accepted for inclusion in Electronic Thesis and Dissertation Repository by an authorized administrator of Scholarship@Western. For more information, please contact [wlsadmin@uwo.ca](mailto:wlsadmin@uwo.ca).

## Abstract

Unmanned Aerial Vehicle (UAV) has the capability of acquiring high spatial and temporal resolution images. This new technology fills the data gap between satellite and ground survey in agriculture. In addition, UAV-based crop monitoring and methods are new challenge of remote sensing application in agriculture.

First, in my thesis the potential of UAV-based imagery was investigated to monitor spatial and temporal variation of crop status in comparison with RapidEye. The correlation between red-edge indices and LAI and biomass are higher for UAV-based imagery than that of RapidEye. Secondly, the nitrogen weight and yield in wheat was predicted using the UAV-based imagery. The intra-field nitrogen prediction model performs well at wheat early growth stage. Additionally, the best data collection time for yield prediction is at the end of booting stage. The results demonstrate the UAV-based data could be an alternative effective and affordable approach for farmers on intra-field management.

## Keywords

Remote sensing, UAV, intra-field, crop nitrogen, crop yield, agriculture.

## Acknowledgments

First of all, I would like to sincerely thank my supervisor Dr. Jinfei Wang, for her encouragement, guidance, advice and support. I have been extremely lucky to become her student and under her supervision. She gave me this great opportunity and support me to work on my research idea and direction. Her warm-hearted and modest personality and stringent academic attitude have kept inspiring me in my entire research.

I would like to thank Dr. Jiali Shang and Dr. Jiangui Liu from the Agriculture and Agri-food Canada for their support in providing the UAV and RapidEye data in Chapter 2. They both kept providing valuable suggestions and comments on my paper writing. Their encouragement and kindness will always be remembered.

I would also like to thank all the members in our Geographic Information Technology & Applications Lab, Chunhua Liao, Boyu Feng, Ian Pritchard, Dr. Zhenpei Li and Dr. Xiaodong Huang for supporting me during my two years research. The visiting scholar Dr. Minfeng Xing from University of Electronic Science and Technology of China provided helpful agricultural suggestions and field work experiences in my research. Also thanks to A&L Canada Laboratories which I worked more than six years, they provided me the UAV imagery and yield spatial distribution data for my research in Chapter 3. Great appreciate to Dr. Haifeng Song from A&L Canada for providing helpful suggestions and comments to inspire me to keep moving forward.

I also thank the Department of Geography, Dan Shrubsole, Lori Johnson, Angelica Lucaci, Peter Ashmore, Jeff Hopkins, Micha Pazner, and Erika Hill for their teaching and support of my research.

Finally, I would like to thank my parents for their support and encouragement. I would like to thank my wife, Ziqi Lin, for her understanding and sacrifice throughout my study. Your love and support gave me the confidence and motivation on my thesis.

# Table of Contents

Abstract .....	i
Acknowledgments.....	ii
Table of Contents .....	iii
List of Tables .....	vi
List of Figures .....	vii
List of Appendices .....	xii
Glossary .....	xiii
Chapter 1 .....	1
1 Introduction .....	1
1.1 Remote sensing in precision farming.....	1
1.2 Optical satellite remote sensing .....	2
1.3 UAV-based remote sensing .....	3
1.4 Research objectives and structure.....	4
1.5 References:.....	6
Chapter 2.....	11
2 Comparisons between UAV-based and RapidEye Data for Mapping Intra-Field Spatial Variation of Corn Status and Monitoring Multi-Temporal Corn Growth.....	11
2.1 Introduction.....	11
2.2 Methods.....	14
2.2.1 Study site.....	14
2.2.2 Field data collection .....	18
2.2.3 UAV and RapidEye multispectral data preprocessing.....	18
2.2.4 Radiometric calibration for UAV imagery .....	21
2.2.5 Comparison of Remotely sensed products, LAI and biomass .....	23

2.3	Results and discussion .....	25
2.3.1	UAV and RapidEye imagery NDVI histograms and basic statistics .....	25
2.3.2	Intra-field crop monitoring using UAV and RapidEye.....	29
2.3.3	Comparison of LAI and biomass between UAV and RapidEye imagery	32
2.4	Conclusions.....	39
2.5	References:.....	41
Chapter 3	.....	46
3	Estimation of Winter Wheat Nitrogen Weight and Yield Using UAV-Based Imagery and Ground Calculated Biomass .....	46
3.1	Introduction.....	46
3.2	Materials and Methods.....	50
3.2.1	Study sites .....	50
3.2.2	Field data collection .....	52
3.2.3	UAV-based blue-green-NIR imagery processing.....	53
3.2.4	Spatial yield distribution .....	55
3.2.5	Model development .....	56
3.3	Results.....	59
3.3.1	UAV-based imagery normalization and GNDVI calculation .....	59
3.3.2	Winter wheat biomass vs. plant height and fCover and PAI .....	62
3.3.3	Relationship between winter wheat foliage nitrogen and GNDVI; total nitrogen weight and GNDVI.....	63
3.3.4	Estimation of winter wheat final yield using temporal GNDVI.....	68
3.4	Discussion .....	73
3.4.1	Relationship between Nitrogen content and GNDVI .....	73
3.4.2	Nitrogen weight model with May and June data .....	74
3.4.3	PAI vs. fCover for biomass estimation .....	76
3.4.4	Discussion of estimated yield data.....	77

3.5	Conclusions.....	79
3.6	References:.....	81
4	Conclusions.....	85
4.1	Summary.....	85
4.2	Conclusion and results.....	86
4.3	Research contributions.....	86
4.4	Possible future research.....	87
4.4.1	Multispectral camera.....	87
4.4.2	Plant height and fraction of vegetation cover.....	88
	Appendices.....	89
	Appendix A Temporal UAV imagery in corn field.....	89
	Appendix B UAV-based imagery calibration results.....	95
	Appendix C Cumulative Vegetation Index Theorem and Results.....	96
	Appendix D Vegetation index and cumulative vegetation index for corn field in 2014 .....	97
	Appendix E Ground reference data.....	100
	Appendix F UAV system and ground station.....	104
	Appendix G Temporal UAV-based blue-green-NIR imagery processing.....	106
	Curriculum Vitae.....	111

## List of Tables

Table 2.1 Specification comparison between sensors in UAV and RapidEye. ....	19
Table 2.2 Overview of UAV imagery acquisition dates and number of ground measurements. .....	21
Table 2.3 Vegetation indices used in the study.....	24
Table 2.4 UAV and RapidEye derived NDVI value statistics at original resolution in June and July. ....	26
Table 3.1 Date and total sample number for data collection. ....	55
Table 3.2 Data combinations and results using linear regression .....	70
Table D-1 UAV-based imagery Vegetation index values .....	97
Table D-2 RapidEye imagery vegetation index values.....	97
Table D-3 UAV-imagery cumulative vegetation index values.....	98
Table D-4 RapidEye imagery cumulative vegetation index values.....	98
Table E-1 Corn field ground reference data, LAI, averagey height and biomass, in 2014 ..	100
Table E-2 Wheat ground reference data, PAI and average height, vegetation cover fraction and nitrogen content in 2015.....	100
Table E-3 Ground reference biomass for wheat fields in 2015 .....	103

## List of Figures

Figure 2.1 Map of corn study site in St. Isidore Ontario. ....	15
Figure 2.2 The true color image of the experimental corn field on July 24. The mosaicked UAV image composited from blue, green, and red bands was showing the corn field.....	16
Figure 2.3 50% (red zone) and 100% (blue zone) nitrogen treatment zones in the corn field. Six sampling points were deployed within the field, three in the 50% zone and three in the 100% zone.....	17
Figure 2.4 Reference tarps on the ground. (a) Both white and grey tarp, (b) 45% white tarp, (c) 5% grey tarp. ....	20
Figure 2.5 The average reflectance curve for all reference targets on June 23. ....	22
Figure 2.6 Ground reference targets in green band of UAV images on June 23. Red box is bare soil; yellow box is black tarp; blue box is white tarp; and green box is asphalt road.....	23
Figure 2.7 Corn field NDVI histogram as percentage of total values. UAV NDVI rescaled to the same resolution as RapidEye. (a) RapidEye NDVI histogram for corn on June 19, (b) UAV NDVI histogram for corn on June 23, (c) RapidEye NDVI histogram for corn on July 25, (d) UAV NDVI histogram for corn on July 24.....	27
Figure 2.8 Relationship of vegetation indices between UAV and RapidEye imagery at each sampling point. (a) NDVI, (b) green NDVI, (c) MTVI2, (d) SR. ....	29
Figure 2.9 Different NDVI maps for 50% and 100% nitrogen treatment zones in UAV and RapidEye imagery on July 24 and July 25. (a) 50% and 100% nitrogen treatment NDVI map from UAV imagery, (b) 50% and 100% nitrogen treatment NDVI map from RapidEye imagery. ....	30
Figure 2.10 NDVI histogram for 50% and 100% nitrogen treatment zones in the UAV and RapidEye imagery. (a) NDVI histogram for 50% N treatment zone of RapidEye, (b) NDVI	



histogram for 100% N treatment zone of RapidEye, (c) NDVI histogram for 50% N treatment zone of UAV, (d) NDVI histogram for 100% N treatment zone of UAV.....	31
Figure 2.11 Scatterplot between LAI ( $\text{m}^2/\text{m}^2$ ) and UAV derived vegetation indices: (a) NDVI, (b) gNDVI, (c) MTVI2, (d) NDVI <sub>re</sub> , (e) SR, (f) SR <sub>re</sub> . The solid line is the best-fit function between all LAI measurements and vegetation indices.....	33
Figure 2.12 Relationship between LAI ( $\text{m}^2/\text{m}^2$ ) and RapidEye derived vegetation indices: (a) NDVI, (b) gNDVI, (c) MTVI2, (d) NDVI <sub>re</sub> , (e) SR, (f) SR <sub>re</sub> . The solid line is the best-fit function between all LAI measurements and vegetation indices.....	35
Figure 2.13 Relationship between biomass and UAV cumulative vegetation indices: (a) cumulative NDVI, (b) cumulative GNDVI, (c) cumulative MTVI2, (d) cumulative NDVI <sub>re</sub> , (e) cumulative SR, (f) cumulative SR <sub>re</sub> . The solid line is the best-fit function between all biomass measurements and cumulative vegetation indices. ....	37
Figure 2.14 Relationship between biomass and RapidEye cumulative vegetation indices: (a) cumulative NDVI, (b) cumulative GNDVI, (c) cumulative MTVI2, (d) cumulative NDVI <sub>re</sub> , (e) cumulative SR, (f) cumulative SR <sub>re</sub> . The solid line is the best-fit function between all biomass measurements and cumulative vegetation indices. ....	38
Figure 3.1 Map of study sites and sample points. Eight points were sampled in each field. .	51
Figure 3.2 Mosaicked UAV-based aerial images (NIR shows as red, blue shows as blue, green shows as green) for all test field, (a) field one, (b) field two, (c) field three, (d) field four. ....	54
Figure 3.3 Map of spatial yield. All data were in a point format, with the unit bushels/acre.	56
Figure 3.4 The flowchart for data processing and models establishment. Left side is flowchart of yield prediction model; middle is general images processing; right side is flowchart of total nitrogen weight model. ....	58
Figure 3.5 Ground reference targets, roof and road (red boxes) selection in the UAV-based imagery. (a) image captured on May 21, (b) image captured on May 29, (c) images captured on June 19, (d) image captured on July 2. ....	60

Figure 3.6 GNDVI images before and after image normalization on May 29. (a) GNDVI image before normalization, (b) GNDVI image after normalization. ....	61
Figure 3.7 Scatter plot for fCover and reference dry biomass for all samples in wheat collected during the entire season (n = 16). $R^2$ is the coefficient of determination.....	62
Figure 3.8 Scatter plot for PAI and reference dry biomass for all samples in wheat collected during the entire season (n = 16). $R^2$ is the coefficient of determination. ....	63
Figure 3.9 Scatter plot for GNDVI and Nitrogen content for all sample points in wheat (n = 113). ....	64
Figure 3.10 Scatter plot for GNDVI and estimated nitrogen weight with fCover (n = 71)....	65
Figure 3.11 Scatter plot for GNDVI and estimated nitrogen weight with PAI (n = 71). ....	65
Figure 3.12 Scatter plot for GNDVI and estimated nitrogen weight with fCover in wheat (n = 41). ....	66
Figure 3.13 Scatter plot for GNDVI and estimated nitrogen weight with PAI in wheat (n = 41). ....	67
Figure 3.14 Map of total nitrogen weight for test field one.....	68
Figure 3.15 Scatter plot for GNDVI and estimated biomass <sub>fCover</sub> .....	69
Figure 3.16 Scatter plot for GNDVI and estimated biomass <sub>PAI</sub> .....	69
Figure 3.17 Scatter plot for predicted yield and reference yield map using the fraction vegetation cover model. ....	71
Figure 3.18 Scatter plot for predicted yield and reference yield map using the fraction vegetation cover model, with bare area removed. ....	71
Figure 3.19 Scatter plot for predicted yield and reference yield using the PAI model.....	72
Figure 3.20 Scatter plot for predicted yield and reference yield map using the PAI model, with bare area removed. ....	72

Figure 3.21 Map of predicted yield and true spatial yield (bushels/acre), (a) fCover model, (b) PAI model, (c) True spatial yield. The blank part in (c) were bare area in the wheat field for which the harvester had no measurements. ....	73
Figure 3.22 Photographs of wheat fields at different BBCH. (a) May 21 at BBCH 42; (b) May 29 at BBCH 48; (c) June 19 at BBCH 65; (d) July 2 at BBCH 79; (e) July 27 at BBCH 99.....	75
Figure 3.23 Bare areas in wheat field. ....	78
Figure A-1 True color UAV image for corn field on June 9, 2014 in St. Isidore.....	89
Figure A-2 True color UAV image for corn field on June 23, 2014 in St. Isidore.....	90
Figure A-3 True color UAV image for corn field on July 24, 2014 in St. Isidore. ....	91
Figure A-4 True color RapidEye image for corn field on May 31, 2014 in St. Isidore.....	92
Figure A-5 True color RapidEye image for corn field on June 19, 2014 in St. Isidore.....	93
Figure A-6 True color RapidEye image for corn field on July 25, 2014 in St. Isidore. ....	94
Figure B-1 Relationship between reflectance and DN <sub>s</sub> for green, red, red-edge, and NIR band.....	95
Figure C-1 Annual vegetation index distribution curve. ....	96
Figure F-1 Fixed wing UAV for image collection in this study. ....	104
Figure F-2 Control panel of the Mission Planner software.....	105
Figure F-3 Different flight path showed at the same field.....	105
Figure G-1 UAV-based images processing in Agisoft. ....	106
Figure G-2 UAV-based blue-green-NIR imagery on May 21, 2015 .....	107
Figure G-3 UAV-based blue-green-NIR imagery on May 29, 2015 .....	108

Figure G-4 UAV-based blue-green-NIR imagery on June 19, 2015 .....	109
Figure G-5 UAV-based blue-green-NIR imagery on July 2, 2015.....	110

## List of Appendices

Appendix A Temporal UAV imagery in corn field .....	89
Appendix B UAV-based imagery calibration results .....	95
Appendix C Cumulative Vegetation Index Theorem and Results.....	96
Appendix D Vegetation index and cumulative vegetation index for corn field in 2014 .....	97
Appendix E Ground reference data.....	100
Appendix F UAV system and ground station .....	104
Appendix G Temporal UAV-based blue-green-NIR imagery processing.....	106

## Glossary

**Agrisoft PhotoScan** - is a professional tool for a photogrammetry pipeline, which photogrammetric processing of digital images and generates 3D spatial data to be used in GIS applications.

**ASD** – (Analytical Spectral Devices) is a high performance single-beam field spectroradiometer measuring over the visible to short-wave infrared wavelength range. The instrument is very rapid scanning, acquiring single spectra in milliseconds via its fiber-optic input.

**BBCH** – is a scale used to identify the phenological development stages of a plant. It used a decimal code system which is divided into principal and secondary growth stages.

**BRDF** – (Bidirectional reflectance distribution function) is a function of four real variables that defines how light is reflected at an opaque surface.

**Bushel** – is a measure of capacity, used for dry goods. 1 bushel wheat is 24 kg.

**CAN-EYE software** – is an imaging software used to extract the canopy structure characteristics from true-color images, which includes LAI, ALA, FAPAR, FCOVER, bidirectional gap fraction.

**Coefficient of variation (CV)** – also known as relative standard deviation, is a standardized measure of dispersion of a probability distribution or frequency distribution.

**fCover** – (fraction of green vegetation cover) corresponds to the fraction of ground covered by green vegetation.

**GPS** – is a global navigation satellite system that provides location and time information in all weather conditions.

**LAI** – calculated one-side area of leaves per ground surface, is a parameter of canopy structure.

**Levenberg-Marquardt algorithm** – is used to solve non-linear least squares problems.

**Matlab** –is a multi-paradigm numerical computing environment and fourth-generation programming language.

**PAI** – Plant area index calculated the one-side area of leaves and stems per ground surface, is a parameter of canopy structure.

**Pix4D** – Advanced photogrammetry software uses images to create professional orthomosaics, point clouds, models and more.

**Tetracam** – An array multispectral imaging system with light weight and adjustable filters of lens.

## Chapter 1

### 1 Introduction

#### 1.1 Remote sensing in precision farming

Agriculture in Canada is a well-established and advanced industry, making Canada 5th among agricultural producers and exporters in the world (Agriculture and Agri-Food Canada, 2015). This long-standing lead in the global marketplace is inseparable from technological innovations and practices in agricultural production. Precision farming is an information and technology based farm management system which helps to identify, analyze and manage variability within fields for optimum profitability, sustainability and protection of the farm field (Banu, 2015). Nowadays, precision farming activities that are aided by Geographical Information System and remote sensing technique such as GPS precise sampling, crop health and yield monitoring, and variable rate fertilizer application, help farmers to make better decisions, reduce inputs and improve yields efficiently.

One of the biggest concerns in farmers' farming management is the precise nitrogen fertilizing and final yield prediction. Nitrogen content is an important factor to indicate crop health status and affects the final yield. Farmers tend to apply nitrogen fertilizer efficiently to yield a profitable crop production. Excessive nitrogen fertilizer inputs, not only increase the agricultural costs, can also damage the groundwater and pose a threat to environment (Ribaud et al., 2011). Meanwhile, crop yield determines individual farmer's income and provides important information for government to guide crop price and manage crop production. Remote sensing, as one of the most important elements in precision farming, acquires information about the crop characteristics without making physical contact with the crop (Jensen, 2016), which offers an essential alternative to crop data collection, analysis and interpretation. Remote sensing products can be used by government to make agricultural policies and track agriculture activities, and provide valuable guidance for individual farmers on aspects such as health status of crops.



## 1.2 Optical satellite remote sensing

Current remotely sensed crop nitrogen monitoring and yield estimation methods have been using optical satellite or airborne imagery for models establishment (Boegh et al., 2013; El-Shikha et al., 2008; Ribaud et al., 2011; Singh, Semwal, Rai, & Chhikara, 2002; Thorp et al., 2012). The essential idea of crop nitrogen monitoring and final yield estimation is the measurement of long-term vegetation vigour as represented by multiple temporal vegetation indices. The vegetation indices, as the products after satellite image enhancement, such as normalized difference vegetation index (NDVI), green NDVI, and modified chlorophyll absorption ratio index (MCARI) had been developed and applied in crop canopy or chlorophyll content estimation (El-Shikha et al., 2008; Feng et al., 2014; Thenkabail, Smith, & Pauw, 2002; Wu, Niu, Tang, & Huang, 2008). Nitrogen is a primary component of chlorophyll that absorbs 70% to 90% of blue and red bands in incident light and reflects light in green and near infrared (NIR) bands (Inman, Khosla, & Mayfield, 2005). Therefore, remote sensing studies can use spectral vegetation indices to quantitatively evaluate the concentrations of chlorophyll and nitrogen in crop canopies. Crop yield prediction can be achieved using remote sensing products such as LAI combined with a crop growth model to simulate the final yield (Clevers, 1997; Doraiswamy, Moulin, Cook, & Stern, 2003; Jing-feng Huang, Tang, Ousama, & Wang, 2002).

Nowadays, many optical satellite systems have been launched due to an increase demand of accurate, real-time, and cost-effective information about earth observation, such as Landsat 8 (2013), RapidEye (2008), GeoEye-1 (2008), WorldView-2 (2009), SPOT-7 (2014), and Sentinel-2A (2015). For instance, the longest-running earth observation program, Landsat, provides continuous free remote sensing data for research and applications in many fields through six Landsat missions spanning nearly 44 years (Powell, Pflugmacher, Kirschbaum, Kim, & Cohen, 2007). The most recent Landsat-8 provides nine spectral bands with spatial resolution range from 15 to 60 meters and a 16 day revisit time. Past research have demonstrated the application capability of Landsat in leaf area index (LAI) (Cohen, Maersperger, Gower, & Turner, 2003; Liu, Pattey, & Jégo, 2012) and crop yield estimation (Doraiswamy et al., 2003; Ferencz et al., 2004) for large

areas. Another satellite system, RapidEye constellation that contains five satellites, was developed in Germany and launched in 2008. Its constellation system can offer a one day revisit time on the same area with spatial resolution of 5 meters and provide crop monitoring with rapidly changing conditions. In addition, the RapidEye, the multispectral satellite system that first offer the red-edge band, has great potential in crop classification and chlorophyll or nitrogen measurement (Ramoelo et al., 2012; Schuster, Förster, & Kleinschmit, 2012). Airborne and satellite hyperspectral data has also been used in crop nitrogen monitoring (Basso, Fiorentino, Cammarano, & Schulthess, 2015; Chen et al., 2010; Jain, Ray, Singh, & Panigrahy, 2007). Some researchers developed specific vegetation indices to estimate plant nitrogen and chlorophyll based on ground hyperspectral measurement (Barnes et al., 2000; Ye, Sakai, Okamoto, & Garciano, 2008).

Given the great potential of application in agriculture, remote sensing is restricted to regional and national scales due to the restriction of spatial and temporal resolution in optical imagery. Optical satellite imagery always has problem with revisit time and cloud cover during crop monitoring which poses difficulties to provide high quality multiple temporal images. Additionally, the cost of high temporal resolution airborne imagery is too high to achieve frequent monitoring in one crop season for individual users. Data collection of ground based methods in large fields like in Canada where farmers usually have several hundred acre farms can be time-consuming and cost inefficient. Therefore the current methods based on multispectral and hyperspectral data, even capable of providing crop information at regional and national scales, is difficult to apply on real time and intra-field crop management. An alternative remote sensing solution is needed to provide the flexible and accurate intra-field crop monitoring.

### 1.3 UAV-based remote sensing

One of the most important requirements for intra-field crop monitoring is high spatial and temporal resolution imagery. In terms of remote sensing data collection, the UAV is a reliable platform that can fly by following a pre-programed route and capture the centimeter resolution images at specific locations. UAV operation has few restrictions except in inclement weather, which gives the UAV a higher capability in high frequency image collection than that of satellites. Compare to airborne remote sensing, an UAV can

easily achieve over 90% overlap images which is useful for homogeneous canopy mosaicking in image processing. Currently, UAV can be classified into two categories: a fix-wing plane which has a large area coverage and a long flight duration, but a less payload; and a multicopter which has a larger payload, but a shorter flight duration. In Chapter 2, the experiment used the multicopter and a heavy multispectral camera, while in Chapter 3 a fix-wing plane was used with a light camera in order to cover a larger area. The overall time of image processing after acquisition in UAV is shorter than that of satellites. All images can be pre-processed in the same day, can provide real-time results for deliver to individual users instantly. In addition, the cost including UAV system, data collection, and data processing is much lower than that of airborne and satellites. With the rapid development of the UAV technique in recent years, many researchers have attempted to use different types of sensors attached to an UAV to monitor crops and predict yields (Bendig et al., 2014; J. Berni, Zarco-Tejada, Suarez, & Fereres, 2009; Hunt et al., 2010; Kalisperakis, Stentoumis, Grammatikopoulos, & Karantzalos, 2015; Zarco-Tejada, González-Dugo, & Berni, 2012).

## 1.4 Research objectives and structure

The objectives of this research are to evaluate the UAV-based multispectral imagery for usage in crop intra-field status monitoring and application in crop nitrogen and yield prediction in Ontario. As mentioned above, nitrogen content monitoring and final yield precision are the factors of most concern. Optical satellite and airborne imagery do not meet individual farmer's need for crop real-time and intra-field monitoring. UAV-based multispectral imagery provides a potential opportunity to fill in gaps between remotely sensed precision farming management and individual farmers.

The objectives of this thesis are to:

1. Compare the ability to detect intra-field spatial crop status variations between the UAV-based multispectral imagery and optical satellite imagery in corn field.
2. Evaluate the accuracy of multiple temporal UAV-based multispectral imagery in the estimation of LAI and biomass.

3. Develop and evaluate a total nitrogen weight model for wheat using UAV-based blue-green-NIR imagery, in order to estimate total nitrogen in the early growth stage and provide a nitrogen weight map.
4. Develop and evaluate a final yield model for wheat using UAV-based blue-green-NIR imagery, in order to predict the final yield and determine the best data collection time for wheat yield prediction.

Two study sites were employed to evaluate and develop methods for crop status monitoring and yield estimation from UAV-based imagery. One of the study sites is a corn field in St. Isidore in Eastern Ontario. The other study site is a wheat field in Melbourne in Southwestern Ontario.

This thesis is presented in integrated-article format. In Chapter 1, a brief review of the literature on the research problems and the objectives of research given. Chapter 2 is the detection sensitivity in spatial crop status variations between the UAV-based multispectral imagery and optical satellite imagery and evaluate the multi-temporal remotely sensed products, LAI and biomass, in terms of accuracy. Chapter 3 develops wheat total nitrogen and biomass prediction models from an alternative biomass estimate method. In Chapter 4, a summary of this thesis is given to answer the research problems and objectives. Possible future research directions is discussed at the end.

## 1.5 References:

- Agriculture and Agri-Food Canada. (2015). We grow a lot more than you may think. *Government of Canada*. Retrieved from <http://www.agr.gc.ca/eng/about-us/publications/economic-publications/?id=1366724330959>
- Banu, S. (2015). Precision agriculture: Tomorrow's technology for today's Farmer. *Journal of Food Processing & Technology*, 06(08), 468. <http://doi.org/10.4172/2157-7110.1000468>
- Barnes, E., Clarke, T., Richards, S., Colaizzi, P. D., Haberland, J., Kostrzewski, M., ... Moran, M. S. (2000). Coincident detection of crop water stress, nitrogen status and canopy density using ground-based multispectral data. *Proceedings of the Fifth International Conference on Precision Agriculture*. Retrieved from [http://www.cprl.ars.usda.gov/wmru/pdfs/Barnes-coincident detection.pdf](http://www.cprl.ars.usda.gov/wmru/pdfs/Barnes-coincident%20detection.pdf)
- Basso, B., Fiorentino, C., Cammarano, D., & Schulthess, U. (2015). Variable rate nitrogen fertilizer response in wheat using remote sensing. *Precision Agriculture*, 17(2), 168–182. <http://doi.org/10.1007/s11119-015-9414-9>
- Bendig, J., Bolten, A., Bennertz, S., Broscheit, J., Eichfuss, S., & Bareth, G. (2014). Estimating biomass of barley using crop surface models (CSMs) derived from UAV-based RGB imaging. *Remote Sensing*, 6(11), 10395–10412. <http://doi.org/10.3390/rs61110395>
- Berni, J., Zarco-Tejada, P. J., Suarez, L., & Fereres, E. (2009). Thermal and narrowband multispectral remote sensing for vegetation monitoring from an unmanned aerial vehicle. *IEEE Transactions on Geoscience and Remote Sensing*, 47(3), 722–738. <http://doi.org/10.1109/TGRS.2008.2010457>
- Boegh, E., Houborg, R., Bienkowski, J., Braban, C. F., Dalgaard, T., Van Dijk, N., ... Sutton, M. A. (2013). Remote sensing of LAI, chlorophyll and leaf nitrogen pools of crop- and grasslands in five European landscapes. *Biogeosciences* (Vol. 10). <http://doi.org/10.5194/bg-10-6279-2013>

- Chen, P., Haboudane, D., Tremblay, N., Wang, J., Vigneault, P., & Li, B. (2010). New spectral indicator assessing the efficiency of crop nitrogen treatment in corn and wheat. *Remote Sensing of Environment*, 114(9), 1987–1997.  
<http://doi.org/10.1016/j.rse.2010.04.006>
- Clevers, J. G. P. . (1997). A simplified approach for yield prediction of sugar beet based on optical remote sensing data. *Remote Sensing of Environment*, 61(2), 221–228.  
[http://doi.org/10.1016/S0034-4257\(97\)00004-7](http://doi.org/10.1016/S0034-4257(97)00004-7)
- Cohen, W. B., Maersperger, T. K., Gower, S. T., & Turner, D. P. (2003). An improved strategy for regression of biophysical variables and Landsat ETM+ data. *Remote Sensing of Environment*, 84(4), 561–571. [http://doi.org/10.1016/S0034-4257\(02\)00173-6](http://doi.org/10.1016/S0034-4257(02)00173-6)
- Doraiswamy, P. C., Moulin, S., Cook, P. W., & Stern, A. (2003). Crop Yield Assessment from Remote Sensing. *Photogrammetric Engineering and Remote Sensing*, 69, 665–674. <http://doi.org/10.14358/PERS.69.6.665>
- El-Shikha, D. M., Barnes, E. M., Clarke, T. R., Hunsaker, D. J., a., H. J., Pinter, P. J., ... Thompson, T. L. (2008). Remote sensing of cotton nitrogen status using the canopy chlorophyll content index (CCCI). *Transactions of the ASABE*, 51(1), 73–82.  
 Retrieved from <http://hdl.handle.net/10113/19609>
- Feng, W., Guo, B. Bin, Wang, Z. J., He, L., Song, X., Wang, Y. H., & Guo, T. C. (2014). Measuring leaf nitrogen concentration in winter wheat using double-peak spectral reflection remote sensing data. *Field Crops Research*, 159, 43–52.  
<http://doi.org/10.1016/j.fcr.2014.01.010>
- Ferencz, C., Bognár, P., Lichtenberger, J., Hamar, D., Tarcsai†, G., Timár, G., ... Ferencz-Árkos, I. (2004). Crop yield estimation by satellite remote sensing. *International Journal of Remote Sensing*, 25(20), 4113–4149.  
<http://doi.org/10.1080/01431160410001698870>
- Huang, J., Tang, S., Ousama, A.-I., & Wang, R. (2002). Rice yield estimation using

- remote sensing and simulation model. *Journal of Zhejiang University SCIENCE*, 3(4), 461–466. <http://doi.org/10.1631/jzus.2002.0461>
- Hunt, E. R., Dean Hively, W., Fujikawa, S. J., Linden, D. S., Daughtry, C. S. T., & McCarty, G. W. (2010). Acquisition of NIR-green-blue digital photographs from unmanned aircraft for crop monitoring. *Remote Sensing*, 2(1), 290–305. <http://doi.org/10.3390/rs2010290>
- Inman, D., Khosla, R., & Mayfield, T. (2005). On-the-go active remote sensing for efficient crop nitrogen management. *Sensor Review*, 25(3), 209–214. <http://doi.org/10.1108/02602280510606499>
- Jain, N., Ray, S. S., Singh, J. P., & Panigrahy, S. (2007). Use of hyperspectral data to assess the effects of different nitrogen applications on a potato crop. *Precision Agriculture*, 8(4-5), 225–239. <http://doi.org/10.1007/s11119-007-9042-0>
- Jensen, J. R. (2016). *Introductory Digital Image Processing: A Remote Sensing Perspective* (4th ed.). Pearson.
- Kalisperakis, I., Stentoumis, C., Grammatikopoulos, L., & Karantzalos, K. (2015). Leaf area index estimation in vineyards from UAV hyperspectral data, 2D image mosaics and 3D canopy surface models. *ISPRS - International Archives of the Photogrammetry, Remote Sensing and Spatial Information Sciences*, XL-1/W4, 299–303. <http://doi.org/10.5194/isprsarchives-XL-1-W4-299-2015>
- Liu, J., Pattey, E., & Jégo, G. (2012). Assessment of vegetation indices for regional crop green LAI estimation from Landsat images over multiple growing seasons. *Remote Sensing of Environment*, 123, 347–358. <http://doi.org/10.1016/j.rse.2012.04.002>
- Powell, S. L., Pflugmacher, D., Kirschbaum, A. a., Kim, Y., & Cohen, W. B. (2007). Moderate resolution remote sensing alternatives: a review of Landsat-like sensors and their applications. *Journal of Applied Remote Sensing*, 1(1), 012506. <http://doi.org/10.1117/1.2819342>
- Ramoelo, A., Skidmore, A. K., Cho, M. A., Schlerf, M., Mathieu, R., & Heitkonig, I. M.

- A. (2012). Regional estimation of savanna grass nitrogen using the red-edge band of the spaceborne rapideye sensor. *International Journal of Applied Earth Observation and Geoinformation*, 19(1), 151–162. <http://doi.org/10.1016/j.jag.2012.05.009>
- Ribaudo, M., Delgado, J., Hansen, L., Livingston, M., Mosheim, R., & Williamson, J. (2011). Nitrogen in agricultural systems: Implications for conservation policy. *Environmental Protection*, (127), 89.
- Schuster, C., Förster, M., & Kleinschmit, B. (2012). Testing the red edge channel for improving land-use classifications based on high-resolution multi-spectral satellite data. *International Journal of Remote Sensing*, 33(17), 5583–5599. <http://doi.org/10.1080/01431161.2012.666812>
- Singh, R., Semwal, D. P., Rai, A., & Chhikara, R. S. (2002). Small area estimation of crop yield using remote sensing satellite data. *International Journal of Remote Sensing*, 23(February 2014), 49–56. <http://doi.org/10.1080/01431160010014756>
- Thenkabail, P., Smith, R., & Pauw, E. De. (2002). Evaluation of narrowband and broadband vegetation indices for determining optimal hyperspectral wavebands for agricultural crop characterization. *Photogrammetric Engineering and*, 68(6), 607–621. Retrieved from <http://citeseerx.ist.psu.edu/viewdoc/download?doi=10.1.1.469.1097&rep=rep1&type=pdf>
- Thorp, K. R., Wang, G., West, A. L., Moran, M. S., Bronson, K. F., White, J. W., & Mon, J. (2012). Estimating crop biophysical properties from remote sensing data by inverting linked radiative transfer and ecophysiological models. *Remote Sensing of Environment*, 124, 224–233. <http://doi.org/10.1016/j.rse.2012.05.013>
- Wu, C., Niu, Z., Tang, Q., & Huang, W. (2008). Estimating chlorophyll content from hyperspectral vegetation indices: Modeling and validation. *Agricultural and Forest Meteorology*, 148(8-9), 1230–1241. <http://doi.org/10.1016/j.agrformet.2008.03.005>
- Ye, X., Sakai, K., Okamoto, H., & Garciano, L. O. (2008). A ground-based hyperspectral



imaging system for characterizing vegetation spectral features. *Computers and Electronics in Agriculture*, 63(1), 13–21.

<http://doi.org/10.1016/j.compag.2008.01.011>

Zarco-Tejada, P. J., González-Dugo, V., & Berni, J. A. J. (2012). Fluorescence, temperature and narrow-band indices acquired from a UAV platform for water stress detection using a micro-hyperspectral imager and a thermal camera. *Remote Sensing of Environment*, 117, 322–337. <http://doi.org/10.1016/j.rse.2011.10.007>

## Chapter 2

# 2 Comparisons between UAV-based and RapidEye Data for Intra-Field Spatial Variation Mapping and Multi-Temporal Monitoring of Corn Growth Status

## 2.1 Introduction

The monitoring of intra-field variability in crop development and health status during the growing season can help to optimize and forecast crop production. High temporal and spatial resolution crop status data can provide accurate, near-real-time information for farmers to make well-informed decision on farming activities, as well as maximizing the efficiency of farming procedures (Jingfeng Huang, Wang, Li, Tian, & Pan, 2013).

Nowadays, UAVs have been used in many studies for agricultural crop status monitoring (Kelcey & Lucieer, 2012) (Zarco-Tejada et al., 2012) (J. Berni et al., 2009). Since the UAV is capable of high temporal and spatial resolution imagery collection, it is able to meet the crop monitoring requirements at specific growth stages and regions of interest. The traditional space-borne optical sensors are frequently affected by unfavorable weather conditions. For instance, although the RapidEye constellation system has five identical satellites, the successful image acquisition is still hindered by cloud cover issue. The UAV, on the contrary, is less affected by cloudy conditions. In addition, the data cost for UAV is comparatively lower than high-resolution satellite imagery.

Given the many advantages of the UAV, it is limited by spatial coverage and payload due to both power supply and safety considerations. Therefore, light weight sensors play an important role in crop monitoring using UAVs. In today's market, light weight sensors for crop monitoring could be classified into two groups, the broad-band and narrow-band multispectral sensors. Some researchers have used a modified near-infrared (NIR)-green-blue digital camera and the UAV system for crop monitoring and examined the relationship between the green NDVI and LAI (Hunt et al., 2008; Lelong et al., 2008). This modified camera block red light using a red filter on a digital camera to collect

broadband NIR data. Some other studies used the Tetracam ADC lite camera to collect crop optical information in red, green and NIR bands to derive crop NDVI (Agüera, Carvajal, & Pérez, 2012). Both cameras were equipped with broad-band multispectral sensors which could only provide simple green NDVI (GNDVI) or NDVI; they cannot generate vegetation indices that incorporated the red-edge bands. More recently, many studies used a narrow-band multispectral camera or hyperspectral camera with red-edge bands on a UAV system for monitoring crop growth condition and field management practices (J. A. J. Berni, Zarco-Tejada, Suárez, González-Dugo, & Fereres, 2009; Gevaert, Tang, Suomalainen, & Kooistra, 2014)

The application of UAVs to precision farming has experienced rapid growth over the past decade, but the reflectance retrieval and geometric correction of the data remain a challenge. As most of the vegetation indices (VIs) require reflectance, the digital numbers (DNs) collected by the UAV need to be converted to reflectance. A widely used approach was the empirical line method (Dean, Warner, & McGraw, 2000) (Levin, Bendor, & Singer, 2005). The gray gradient calibration panel with the range of reflectance from 0% to 100% (Wang & Myint, 2015) was also used to establish the relationship between the surface reflectance and the raw image DNs. However, most commercial reference reflectance targets are very expensive and hard to maintain during heavy fieldwork (Buchhorn, Petereit, & Heim, 2013; Weidner & Hsia, 1981). Some researchers calculated vegetation indices directly from DNs (Nebiker, Annen, Scherrer, & Oesch, 2008). Unfortunately, this relative vegetation index is hard to apply to long-term quantitative analysis and cross-site comparisons. Meanwhile, in order to apply UAV-based remotely sensed images in long-term crop monitoring, the biophysical products derived from UAV-based images need to be accurate and reliable in practices.

Leaf area index (LAI) is a key crop biophysical variable used in crop growth modeling for estimating crop phenological stage and forecasting crop final yield (Haboudane, Miller, Pattey, Zarco-Tejada, & Strachan, 2004). LAI has been demonstrated to have significant relationship with canopy vegetation indices (Kalisperakis et al., 2015; Kross, McNairn, Lapen, Sunohara, & Champagne, 2015). The commonly used vegetation indices were calculated based on the reflectance in visual and NIR bands, such as the

NDVI and green NDVI. These vegetation indices are only sensitive to low LAI (less than 3) and start to saturate at medium and high LAI (Nguy-Robertson et al., 2012). Beside the saturation problem, vegetation indices are also sensitive to the background soil; therefore, Soil Adjusted Vegetation Index was used to eliminate the influence of soil (Huete, 1988). Vegetation Indices combined with the reflectance of the red-edge bands, such as SR<sub>re</sub>, NDVI<sub>re</sub>, and MCARI2 (Kross et al., 2015), have shown increased potential for estimating LAI. The red-edge indices in RapidEye had been evaluated for corn LAI retrieval with mixed results (Kross et al., 2015). In this study, a different narrow range of red-edge band (745-755nm) was selected for the Tetracam MCA 6 camera other than the RapidEye red-edge band (690-730nm), and the Tetracam red-edge indices will be evaluated in this study.

In addition to the LAI, biomass is another biophysical parameter in crop modeling which helps estimate crop yield (Bendig et al., 2014). Traditional biomass measurements are carried out via a destructive method which measures the above ground plant weight over a unit area. The time-consuming and destructive nature of this method deems it unfeasible for large sample collection, hence it has promoted the development and application of remotely sensed data for biomass estimation (Gunlu, Ercanli, Baskent, & G., 2014; Jin et al., 2014). Many studies adopted a simple regression method to estimate the above ground biomass through vegetation indices (Chen et al., 2010; Jin et al., 2014). However, this method always has VI saturation problems at medium to high biomass. Contrarily, the cumulative method has the capability to eliminate the saturation problem in biomass estimation (Hou, Gao, Niu, & Xu, 2014; Kross et al., 2015; Liu et al., 2004).

In terms of data comparison for different sensors, some studies used a statistical approach to compare results of VIs from UAV and satellite at the same day (Kross et al., 2015)(Coast, McCabe, Houborg, & Rosas, 2015)(Shang et al., 2015). This approach of images statistical comparison was used to evaluate the capability of different platforms and sensors for intra-field crop monitoring. Beside the statistical comparison for sensors self-characterizes, the long-term performance on crop monitoring is also an important factor for different platforms and sensors. The comparison of products derived from remotely sensed data of different platforms and sensors could be another approach to

analyze the accuracy and tendency of remotely sensed data. This study aimed to compare the UAV and RapidEye remote sensing data using a statistical approach to evaluate the detection capability for crop status and a long-term LAI and biomass comparison approach to evaluate the accuracy and tendency of UAV-based imagery in agriculture application. This study was carried out at St. Isidore, eastern Ontario, Canada. This area has consistently frequent cloud cover during the crop growing season. Therefore, a UAV system with a narrow-band multispectral camera was used to collect multi-temporal imagery in 2014. The purpose of the study was to evaluate the performance of the UAV system and the multispectral camera on crop growth monitoring through an experiment over a corn field.

## 2.2 Methods

### 2.2.1 Study site

The study site was located south of St. Isidore, eastern Ontario, Canada (45.3°, -74.9°) (Figure 2.1). The farmland in this area is privately owned. It supports non-irrigated dry land farming with one harvest during the relatively short May to September growing season. This site is typical of the crop mix found in this part of Canada. Corn is one of the main crop types in this region and the farm following a corn-soybean-wheat rotation. The study was carried out during the 2014 growing season over a corn field. The corn was seeded in early May and harvested in early October. A nitrogen treatment experiment was conducted in this field with two levels of applications, at 50% and 100% of the recommended fertilizer applications at planting (Figure 2.2& 2.3).

Map of corn study site in St. Isidore in eastern Ontario

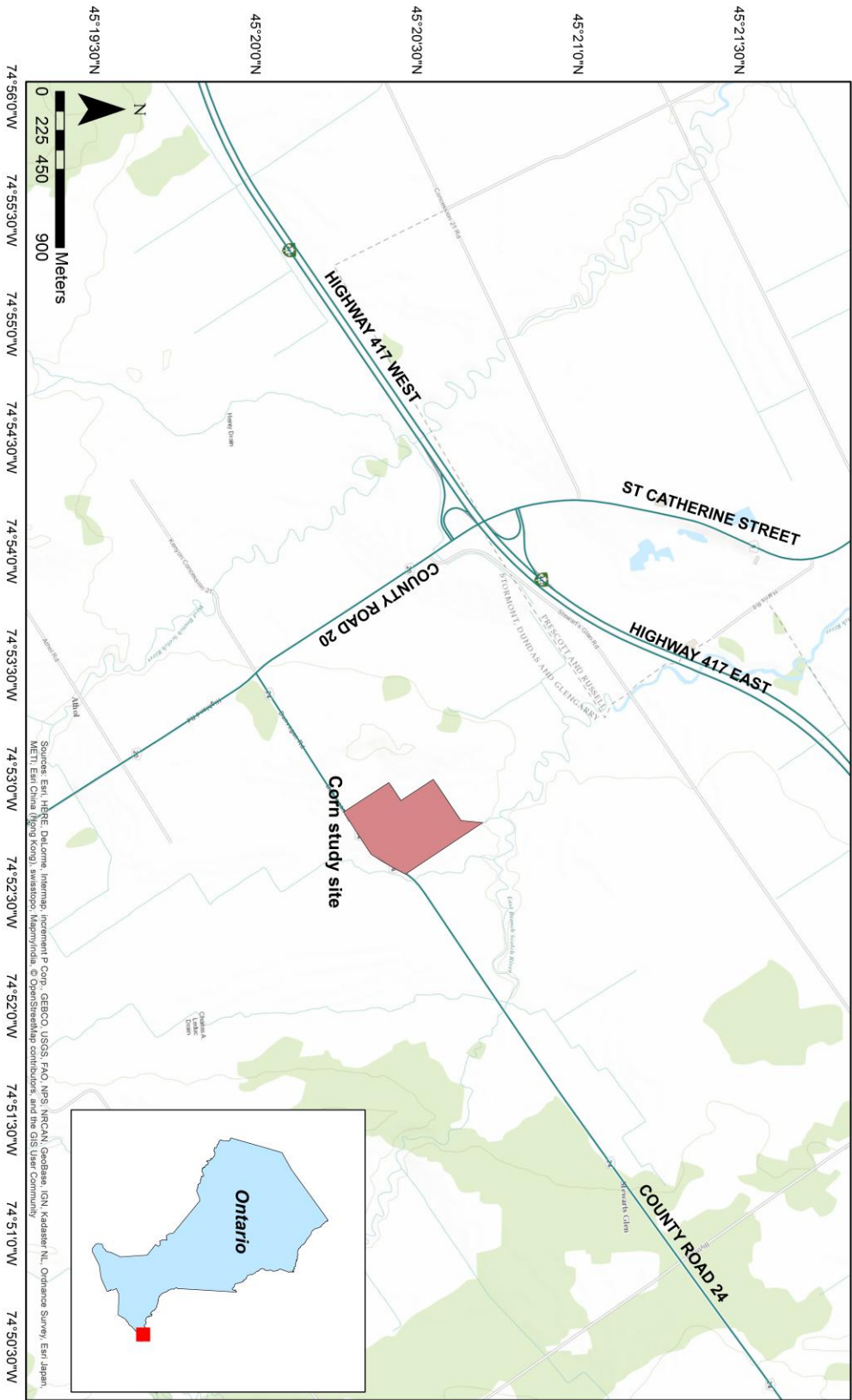
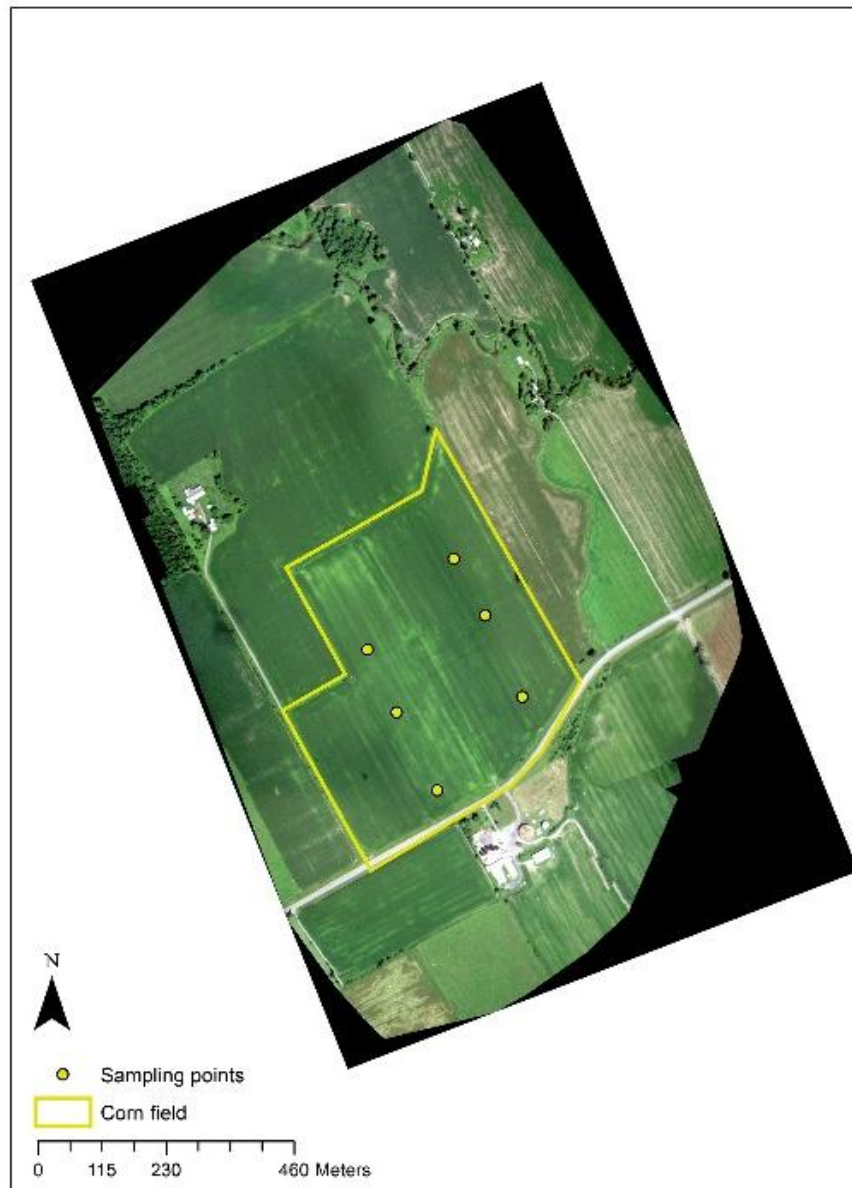


Figure 2.1 Map of corn study site in St. Isidore, eastern Ontario.

### Mosaiced UAV RGB Image for Corn Field on July 24



**Figure 2.2 The true color image of the experimental corn field on July 24. The mosaicked UAV image composited from blue, green, and red bands was showing the corn field.**

### 50% and 100% Nitrogen Treatment Zone in Corn Field



**Figure 2.3 50% (red zone) and 100% (blue zone) nitrogen treatment zones in the corn field. Six sampling points were deployed within the field, three in the 50% zone and three in the 100% zone.**



### 2.2.2 Field data collection

Six sampling points were selected in the experimental field (Figure 2.2), three on 50% nitrogen treatment zone and three on 100% nitrogen treatment zone. Measurements were taken at during each UAV flight (June 6, June 23, July 24, and September 9). At each sampling point, 14 upward digital hemispherical photos were taken on the ground using a Nikon D300s camera with 10.5mm fisheye lens were collected every 5 m along two parallel transects, with seven photos per transect. These photos were used to estimate LAI with the CAN-EYE software (Version 6.2) by an indirect LAI estimation method (Shang et al., 2015). Above-ground corn biomass was collected at each sampling point right after each UAV flight. At each sampling location, five random plants were collected within a 5m by 5m area. The corn plants were partitioned into leaves, stem and seeds and weighed separately for fresh weight, and then oven dried at 80°C for 3 days. Average corn row distance was 75cm and plant distance was 12cm within the row; these measurements were used to calculate the plant density. The oven-dried corn biomass was weighed again and converted to total weight per square meter using the plant density. Average plant height was also measured at each sampling point from three random corn plants.

### 2.2.3 UAV and RapidEye multispectral data preprocessing

The RapidEye constellation contains five identical satellites which could provide regional and global scale crop monitoring with a high frequent revisit time. Moreover, the RapidEye contains a specific red-edge band for agriculture application and provides 5 meter high spatial resolution images which contains more information in crop monitoring than other satellites. Our UAV system with the Tetracam camera has similar bands design as the RapidEye for crop monitoring and could achieve similar vegetation indices with RapidEye, and higher spatial resolution imagery than RapidEye. In terms of the comparison between UAV and satellite images, the RapidEye has the most representative and comparability which has most potential application in crop intra-field monitoring. Four RapidEye satellite images (May 31, June 19, July 25, and September 5) and four UAV-base images (June 9, June 23, July 24, and September 9) were obtained during the corn growing season to compare the single date spatial variations in crop status and

temporal dates variations in LAI and biomass estimation. All RapidEye images were processed in ENVI for radiometric and atmosphere correction.

**Table 2.1 Specification comparison between sensors in UAV and RapidEye.**

Data		UAV (Tetracam)	RapidEye
Spectral Bands (nm)	Blue	485-495	440-510
	Green	545-555	520-590
	Red	640-660	630-685
	Red Edge	745-755	690-730
	NIR	845-855	760-850
Resolution (m)		Depends on height (0.5 in this study)	5

A total of four UAV flights were carried out during the corn growing season. A hexarotor multicopter UAV that had maximum 5kg payload and 18-minute flight time at 3.2kg payload was used in this study. A Tetracam MCA-6 multispectral array camera was mounted on the UAV to collect corn spectral information at the wavelength of 490nm (band width 10nm), 550nm (10nm), 650nm (20nm), 700nm (10nm), 740nm (10nm), and 850nm (40nm). The specification comparison between UAV and RapidEye was shown in Table 2.1. Before each flight, the exposure time of the multispectral camera was adjusted based on the illumination condition while capturing the images. All UAV flights were carried out between 10am to 2pm. The images were retrieved and pre-processed using the Tetracam PixelWrench-2 software to remove lens distortion and vignette of images. Mosaicked images are shown in Appendix A. After the pre-processing, the images were mosaicked by the PIX4D software (Figure 2.1) and the resolution was 0.5 m. The mosaicked UAV images were converted to reflectance for each band based on the empirical line method. A white and a grey reference tarp were placed on the ground while the UAV was capturing images over the study site (Figure 2.3). The alternative reference targets, bare soil and asphalt road, used in this empirical line method in this study due to most calibration panel is hard to maintain and transport during heavy duty fieldwork. The reflectance of the white tarp, gray tarp, bare soil, and the asphalt road were used for the UAV image radiometric correction, the white and gray tarps were known reference targets; the bare soil and asphalt road had homogeneous surfaces and neat spectra. An Analytical Spectral Devices (ASD) spectroradiometer was used to

collect 5 measurements of spectra for all targets in the range between 325nm and 1075nm with a sampling interval of 1.6nm. All targets were measured before and after each UAV flight to calculate the average reflectance for all reference targets to reduce the bidirectional reflectance distribution function (BRDF) effects. The selection on the reflectance of white (45%) and gray (5%) tarps were based on the fact that most vegetation reflectance measurements for all bands between 400nm and 900nm were concentrated between 5% and 60% in practice. The reflectance of the bare soil and asphalt road in all bands were also concentrated between 5% and 45%.



**Figure 2.4 Reference tarps on the ground. (a) Both white and grey tarp, (b) 45% white tarp, (c) 5% grey tarp.**

**Table 2.2 Overview of UAV imagery acquisition dates and number of ground measurements.**

UAV imagery dates	RapidEye imagery dates	LAI samples	Biomass samples
6-Jun-14	31-May-14	6	6
23-Jun-14	19-Jun-14	6	6
24-Jul-14	25-Jul-14	6	6
9-Sep-14	5-Sep-14	-	6

#### 2.2.4 Radiometric calibration for UAV imagery

Before and after the UAV flight, all reference targets, white tarp, grey tarp, bare soil, and asphalt road were measured by ASD. The average reflectance curves for all reference targets are shown in Figure 2.4. The average reflectance of all targets for all six bands in the Tetracam were calculated based on the band width of each camera and ASD measurements, including measurements before and after the UAV flight. In the UAV images, the edge of the grey tarp (5%) had higher DN than the center (Figure 2.5). This may have caused by the diffused reflection of the targets around the tarp. Additionally, the black tarp has very low reflectance which was influenced easily by other objects. In order to eliminate the influence on the black tarp, a lower flight altitude and a bigger tarp will be needed to provide more pure pixels in future work. After removing the black tarp, the reference reflectance value of other targets had a linear relationship between DNs in green, red, red-edge, and NIR bands. These results demonstrated the feasibility of using bare soil and asphalt road as targets to convert DNs into reflectance. The calibration equations are shown in Appendix B.

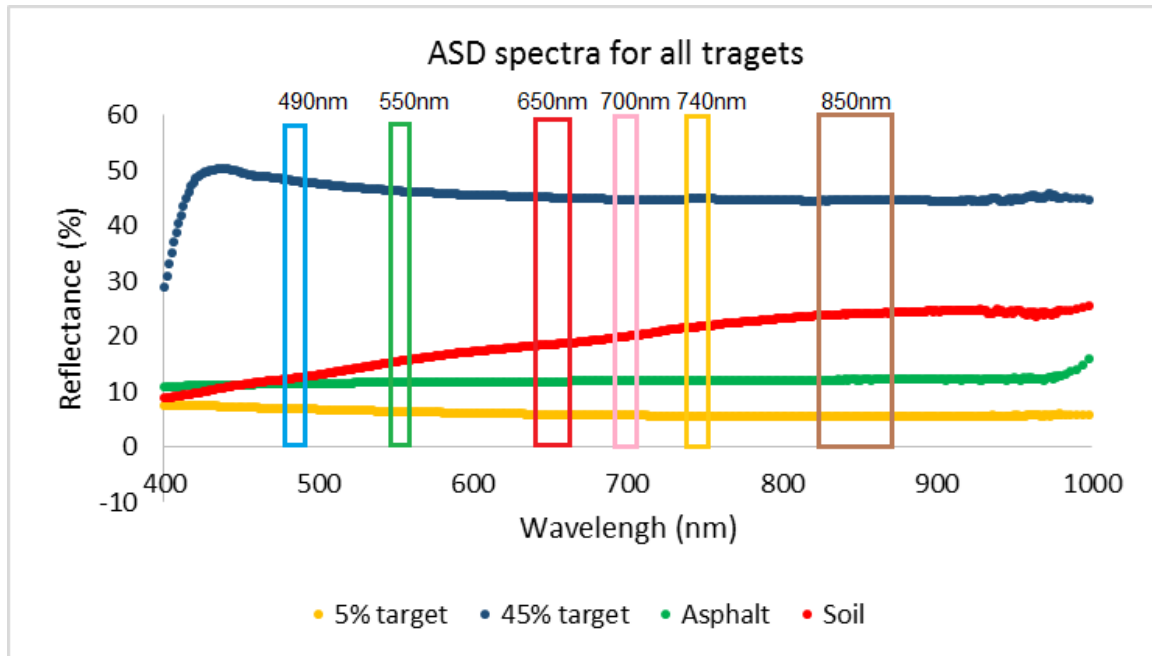


**Figure 2.5 The average reflectance curve for all reference targets on June 23.**

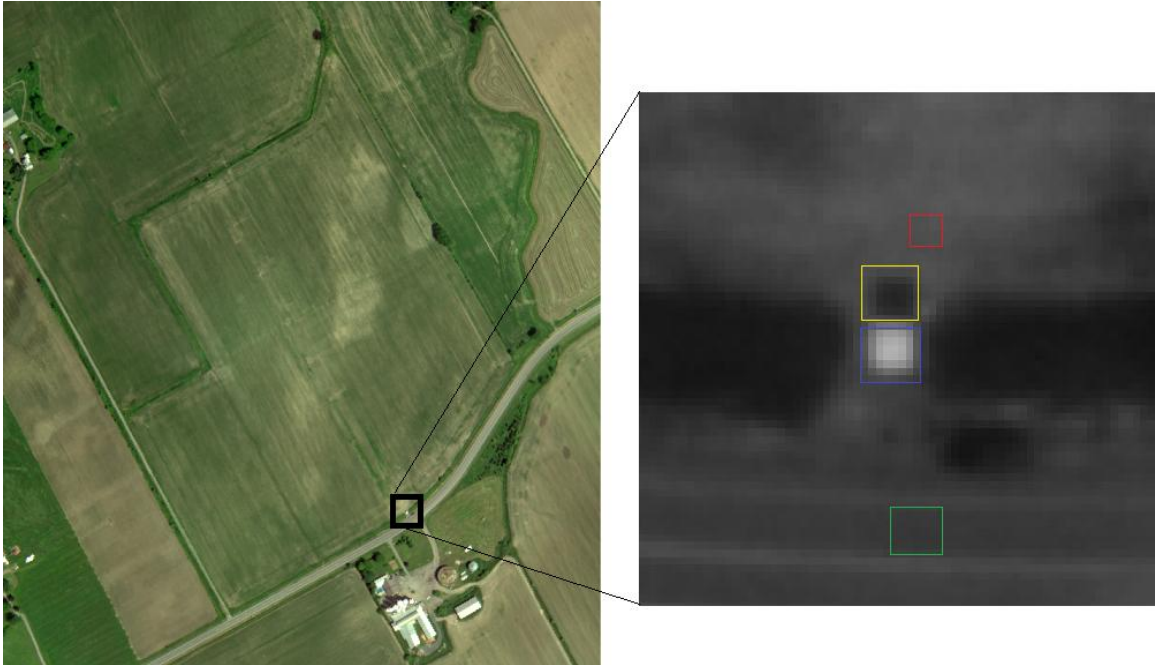


**Figure 2.6 Ground reference targets in green band of UAV images on June 23. Red box is bare soil; yellow box is black tarp; blue box is white tarp; and green box is asphalt road.**

### 2.2.5 Comparison of Remotely sensed products, LAI and biomass

The relationships between vegetation indices and LAI and biomass were used to evaluate the accuracy of remote sensing data in this study. The vegetation indices include: normalized difference vegetation index (NDVI), green normalized difference vegetation (GNDVI), modified triangular vegetation index 2 (MTVI2), red edge normalized difference vegetation index (NDVI<sub>re</sub>), simple ration (SR), and red edge simple ratio (SR<sub>re</sub>). These VIs were evaluated for the estimation of corn LAI at each sampling point. The best-fit linear and non-linear relationships between the VIs and LAI and biomass were evaluated in Matlab v. R2013a. The cumulative VIs were used to evaluate the estimation of total dry biomass. Cumulative VI has been used extensively for the evaluation of plant phenology, total biomass and absorbed photo synthetically active radiation (APAR) (Hou et al., 2014)(Liu et al., 2004)(Kross et al., 2015). A temporal

plant vegetation index can easily be fitted using a logistic model; therefore, at each sampling point the cumulative VI value was calculated based on the logistic model that was determined by the multi-temporal UAV-based and RapidEye images with Levenberg-Marquardt method in Matlab v. R2013a. The logistic model used in this study is as follows (Equation 2.1) (see appendix C)

$$VI(DOY) = \frac{c}{1 + e^{\alpha + bDOY}} + d \quad \text{Equation 2.1}$$

where VI (DOY) is the fitted VI value at day of year (DOY),  $\alpha$ , and  $b$  are the fitting parameters,  $c + d$  is the maximum cumulative VI value, and  $d$  is the initial background VI value (Hou et al., 2014).

**Table 2.3 Vegetation indices used in the study.**

	Index	Equation	Reference
NDVI	Normalized difference vegetation index	$(R_{NIR} - R_{RED}) / (R_{NIR} + R_{RED})$	Gitelson et al. (1996)
gNDVI	Green NDVI	$(R_{NIR} - R_{GREEN}) / (R_{NIR} + R_{GREEN})$	Rouse et al. (1974)
SR	Simple ratio	$R_{NIR} / R_{RED}$	Jordan (1969)
NDVI <sub>re</sub>	Red edge normalized difference vegetation index	$(R_{NIR} - R_{RED-EDGE}) / (R_{NIR} + R_{RED-EDGE})$	Gitelson and Merzlyak (1994)
SR <sub>re</sub>	Red edge simple ratio	$R_{NIR} / R_{RED-EDGE}$	Gitelson and Merzlyak (1994)
MTVI2	Modified triangular vegetation index	$1.5[1.2(R_{NIR} - R_{GREEN}) - 2.5(R_{RED} - R_{GREEN})] / \sqrt{[(2R_{NIR} + 1)2 - (6R_{NIR} - 5\sqrt{(R_{RED}))} - 0.5]}$	Haboudane et al. (2004)

## 2.3 Results and discussion

### 2.3.1 UAV and RapidEye imagery NDVI histograms and basic statistics

The UAV and RapidEye NDVI histograms were used to assess the sensitivity of sensors for the entire corn field since NDVI is a common vegetation index used to analyze green vegetation in remote sensing studies. The range, mean and coefficient of variance (CV) of NDVI values were used to evaluate the detection capability in spatial variations for intra-field crop development and health status within one day measurement. Moreover, the NDVI value in 50% and 100% nitrogen treatment zones were also used to demonstrate the difference of intra-field detection capability in spatial variations between the UAV and RapidEye imagery in corn reproductive stage.

The histograms of the UAV and RapidEye derived NDVI of the corn field both showed a Gaussian distribution but with different range of values. For example, in June, the UAV NDVI values at original resolution (0.5m) had a broader range between 0.02 and 0.83; after rescaling the UAV resolution to 5m to match RapidEye resolution, the range between minimum and maximum value changed to 0.14 and 0.79. The RapidEye derived NDVI had a narrower range, between 0.25 and 0.62 (Table 2.3). In July, the original UAV derived NDVI ranged between 0.29 and 0.83, and the range of values became 0.67 to 0.82 after data were rescaled to 5m. The RapidEye derived NDVI had a much narrower range of values between 0.63 and 0.70. The different range of NDVI values between the two sensors were caused by the difference of images resolution. High resolution UAV images contained more pixels so that the images include more detail and information, such as shadow and bare soil between plants. In addition, offset in images acquisition between two sensors would lead to different reflectance in each band due to BRDF effect.

The basic statistics of the UAV and RapidEye derived NDVI values of the corn field in June and July revealed different behaviors between the UAV and the RapidEye sensors. In June, the mean NDVI values between the UAV and the RapidEye did not show substantial differences. However, the UAV derived NDVI exhibited a higher mean and

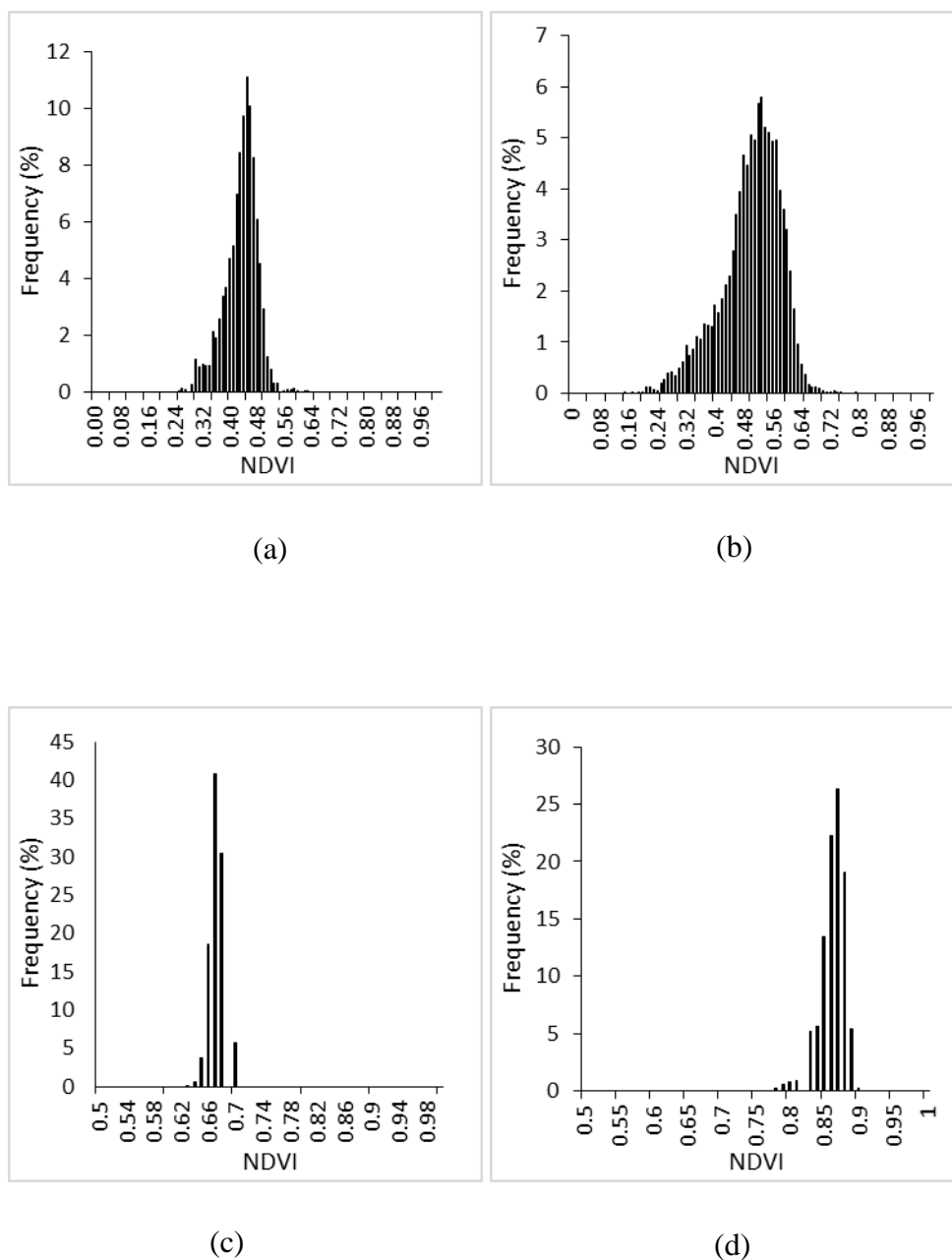


larger standard deviation compared with the RapidEye derived NDVI value. In July, the mean values between the UAV and RapidEye derived NDVI showed significant difference (Table 2.3). The UAV provided a much higher mean NDVI value and larger standard deviation again. Likewise, both dates of NDVI values showed that the CV for NDVI was greater in the UAV imagery (higher resolution) than RapidEye imagery (lower resolution) and more variations were detected by the UAV high resolution imagery.

**Table 2.4 UAV and RapidEye derived NDVI value statistics at original resolution in June and July.**

Date	Platform	Sample Number	Minimum	Maximum	Mean	Standard Deviation	CV (%)
23-Jun	UAV	332852	0.02	0.83	0.5	0.09	18
19-Jun	RapidEye	6991	0.25	0.62	0.43	0.05	11.62
24-Jul	UAV	1017959	0.29	0.9	0.77	0.02	2.32
24-Jul	RapidEye	6991	0.63	0.7	0.67	0.01	1.49

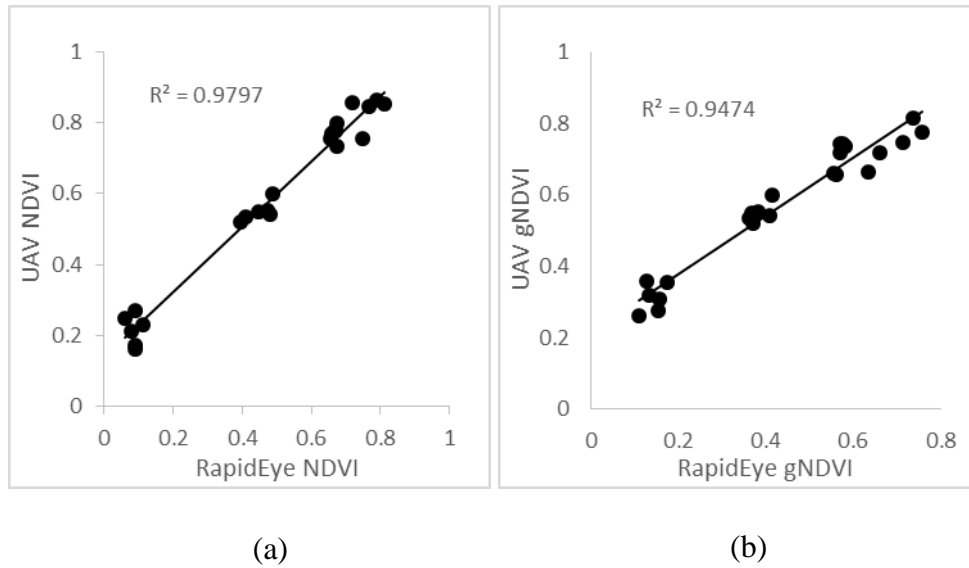
The higher spatial resolution of the UAV imagery provided a possibility for intra-field crop variations detection since it had a broader range of NDVI values and higher CV in this study. In June, the corn plant was going through rapid vegetative growth, and canopy was not closed at this time. The RapidEye pixel contained both soil and crop spectral information and provided a narrow range of NDVI values compare to UAV images. In July the corn canopy was almost completely closed, and the RapidEye NDVI showed a very narrow range of values mainly from the contribution of the corn canopy. However, the UAV derived NDVI showed a much broader range of values both in June and July which still was able to capture the plant canopies as well as the soil between the rows due to its higher spatial resolution.



**Figure 2.7 Corn field NDVI histogram as percentage of total values. UAV NDVI rescaled to the same resolution as RapidEye. (a) RapidEye NDVI histogram for corn on June 19, (b) UAV NDVI histogram for corn on June 23, (c) RapidEye NDVI histogram for corn on July 25, (d) UAV NDVI histogram for corn on July 24.**

The UAV imagery was rescaled to 5m resolution, the same as the RapidEye imagery. Figure 2.6 showed the histogram of the UAV derived NDVI for the corn field in June and July. On both dates, the UAV imagery had higher mean NDVI values than that of the

RapidEye. The Tetracam on the UAV had a narrower bandwidth which were blue (485-495nm), green (545-555nm), red (640-660nm), red-edge (745-755nm), and NIR (845-855nm). RapidEye had relative broader bandwidth which were blue (440-510nm), green (520-590nm), red (630-690nm), red edge (690-730nm), and NIR (760-880nm). For all bands the except red-edge band, the spectrum range of the Tetracam bands were narrower than the RapidEye spectrum range, which may provide a lower reflectance value at the trough of spectrum and higher reflectance value at the peak of spectrum. The relationship between temporal UAV and RapidEye derived VIs values were evaluated in this study (Figure 2.7). All VIs had a high correlation between the UAV and RapidEye imagery, the NDVI had the highest coefficient of determination. In addition, all relationships between temporal UAV and RapidEye derived VIs did not show the same slope values, which are caused by the different characteristics of the sensors and different image acquisition time. The SRre and NDVIre were not evaluated in this study since the Tetracam used different red-edge bands than the RapidEye; these two vegetation indices were evaluated using the LAI and biomass later on.



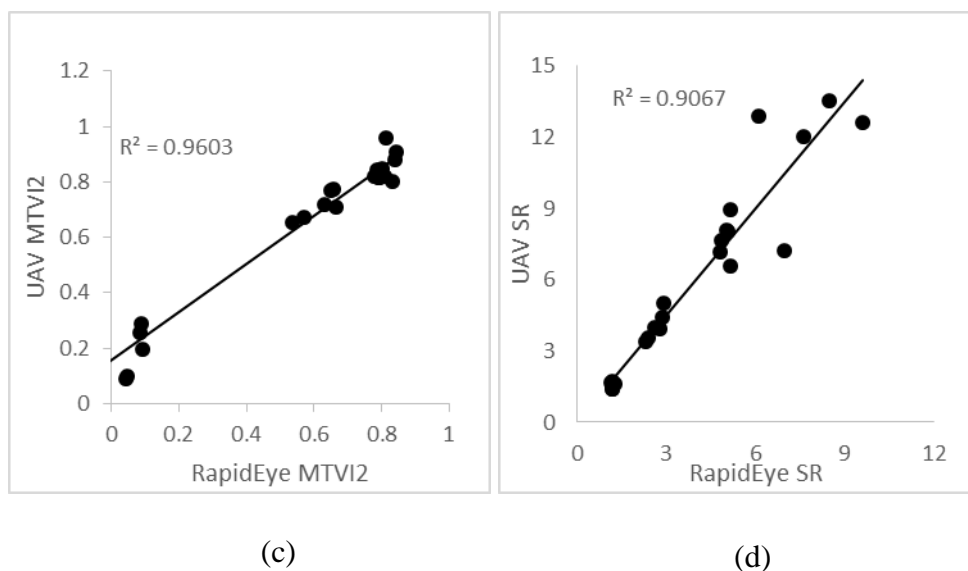


**Figure 2.8 Relationship of vegetation indices between UAV and RapidEye imagery at each sampling point. (a) NDVI, (b) green NDVI, (c) MTVI2, (d) SR.**

### 2.3.2 Intra-field crop monitoring using UAV and RapidEye

After rescaling the July 24 UAV imagery to 5m resolution, a visual inspection was carried out on 50% and 100% nitrogen treatment zones of the corn field. The imagery acquired on July 24 showed better results than that of the images acquired in the other day on the different nitrogen treatment zones. At this time, the corn plant had reached the maximum height. In the 50% nitrogen treatment zone, two areas of lower NDVI were observed on both the UAV and the RapidEye imagery. On the UAV imagery, the 50% and 100% nitrogen treatment zones had a significant difference in the range of the NDVI values. On the RapidEye imagery, however, these two different nitrogen treatment zones did not show a very clear difference (Figure 2.8).

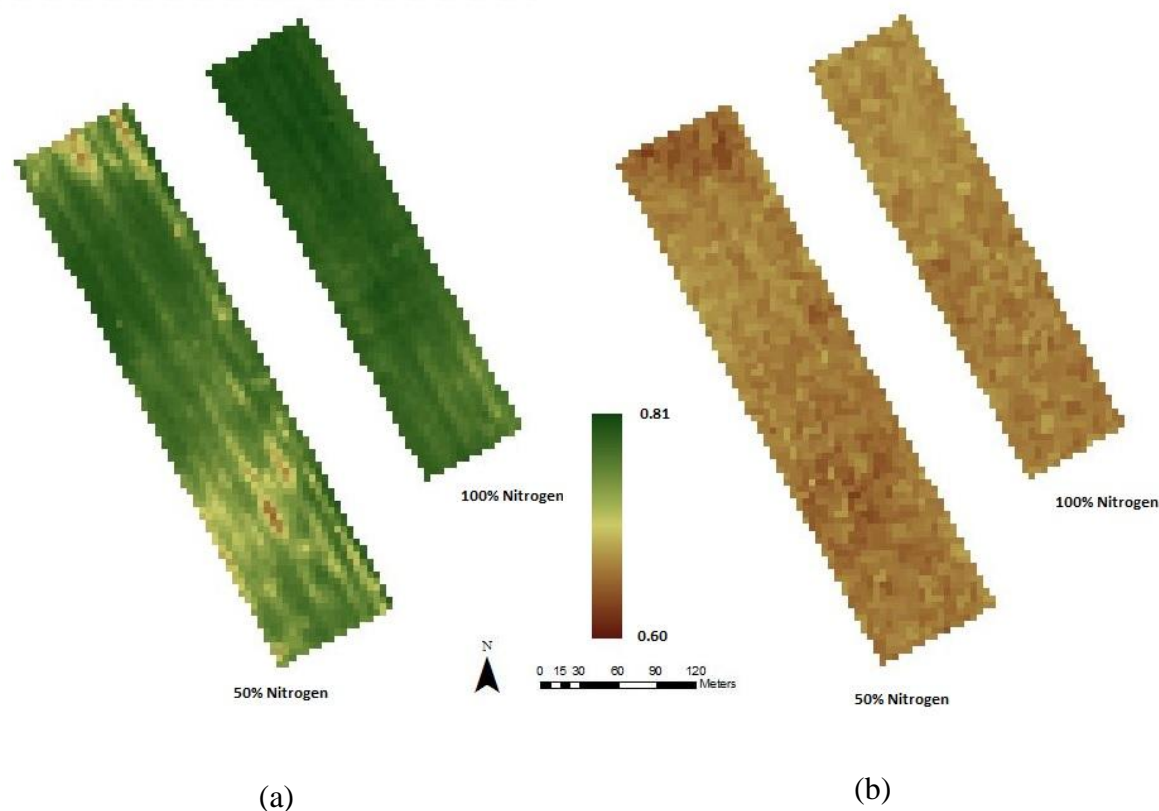


**Figure 2.9 Different NDVI maps for 50% and 100% nitrogen treatment zones in UAV and RapidEye imagery on July 24 and July 25. (a) 50% and 100% nitrogen treatment NDVI map from UAV imagery, (b) 50% and 100% nitrogen treatment NDVI map from RapidEye imagery.**

The histograms of the NDVI of 50% and 100% nitrogen treatment zones derived from the UAV and RapidEye imagery were used to compare the detection capability of within-field growth variations. In the RapidEye imagery, the range of NDVI values in 50% and 100% nitrogen treatment zones was between 0.63 -0.69 and 0.64 -0.69 respectively. In the UAV imagery, the range of NDVI values in 50% and 100% nitrogen treatment zones were 0.65-0.80 and 0.73-0.81 respectively (Figure 2.9). The major NDVI values in RapidEye images showed a 35% and 40% difference in overall data for two different nitrogen treatment zones. UAV images showed only an 18% and 30% difference of the major NDVI values. The boarder range of NDVI values and lower percentage of major values in the overall NDVI values made the intra-field variation to be detected by the

high resolution UAV imagery, suggests that the UAV had a better capability of monitoring intra-field crop growth variations.

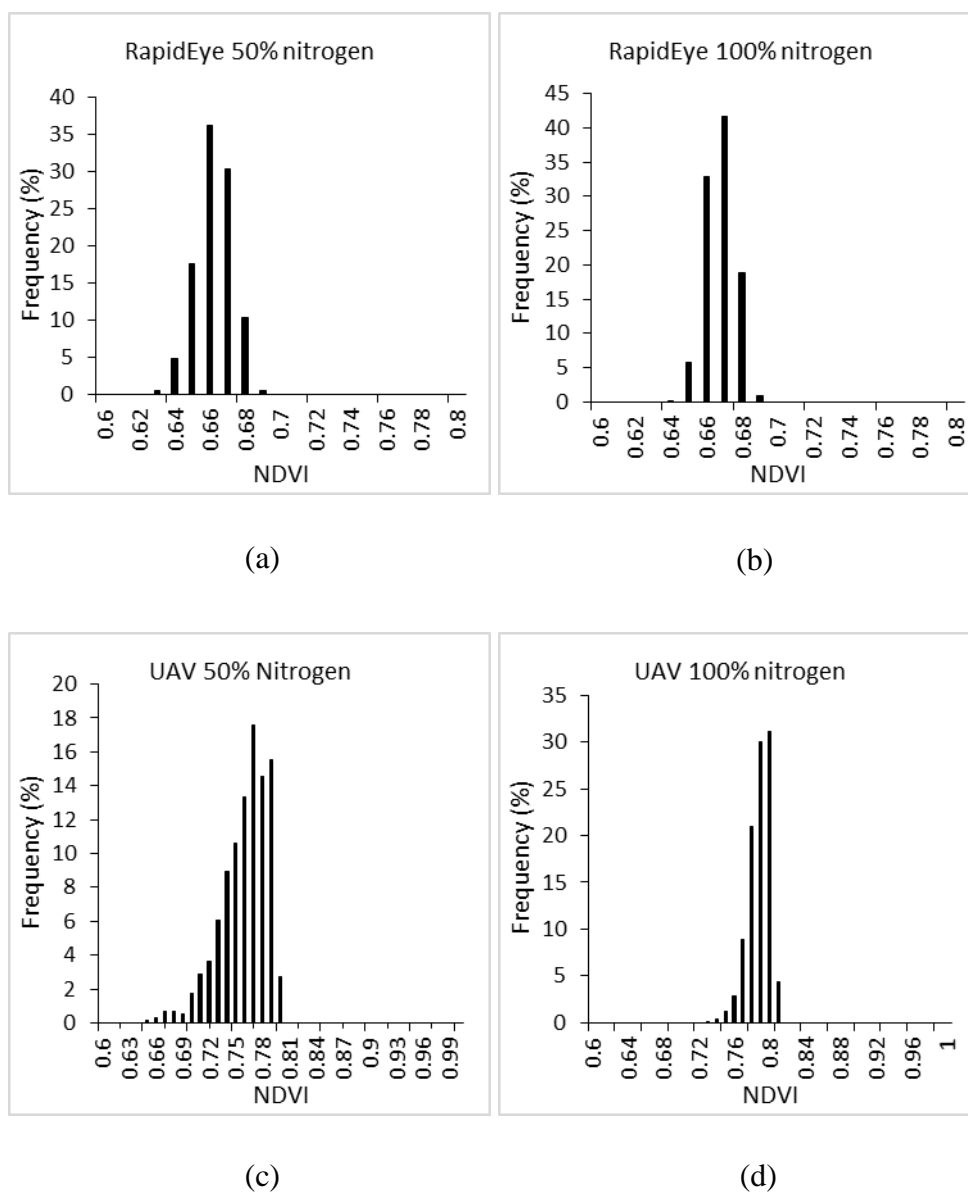
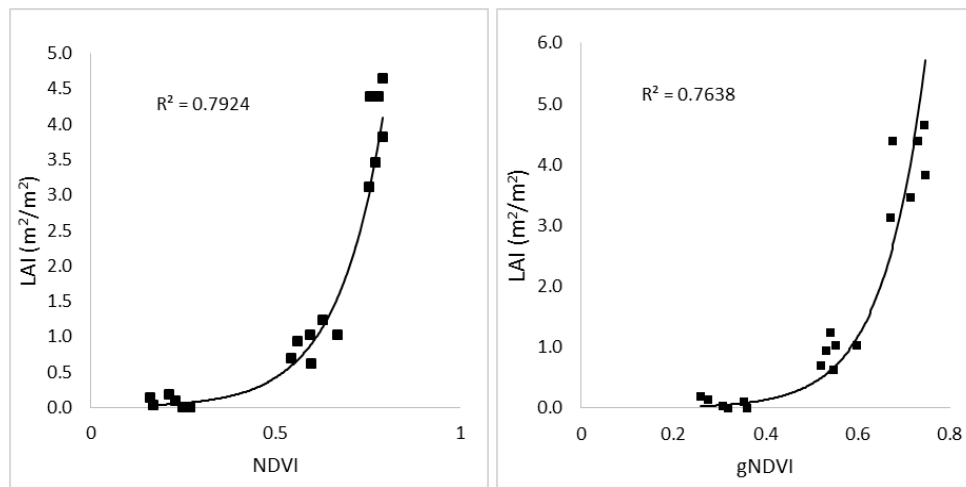


**Figure 2.10 NDVI histogram for 50% and 100% nitrogen treatment zones in the UAV and RapidEye imagery. (a) NDVI histogram for 50% N treatment zone of RapidEye, (b) NDVI histogram for 100% N treatment zone of RapidEye, (c) NDVI histogram for 50% N treatment zone of UAV, (d) NDVI histogram for 100% N treatment zone of UAV.**

### 2.3.3 Comparison of LAI and biomass between UAV and RapidEye imagery

In this study, the maximum ground LAI measurement was  $4.65 \text{ m}^2/\text{m}^2$  recorded on July 24 at corn reproductive stage. The scatterplots of the NDVI, gNDVI, and MTVI2 against the LAI showed these indices had a saturation problem when LAI is greater than  $3 \text{ m}^2/\text{m}^2$  (Figure 2.10, a, b, and c) and they exhibited an exponential distribution. VIs of NDVIre, SR, and SRre showed no saturation for LAI throughout the entire growing season which showed a clear linear distribution against the LAI field measurements. Likewise, these three vegetation indices kept showing a continuous increase when LAI value is greater than  $3 \text{ m}^2/\text{m}^2$ . The best coefficient of determination ( $R^2$ ) between LAI and VIs was 0.93 with the SRre.



(a)

(b)

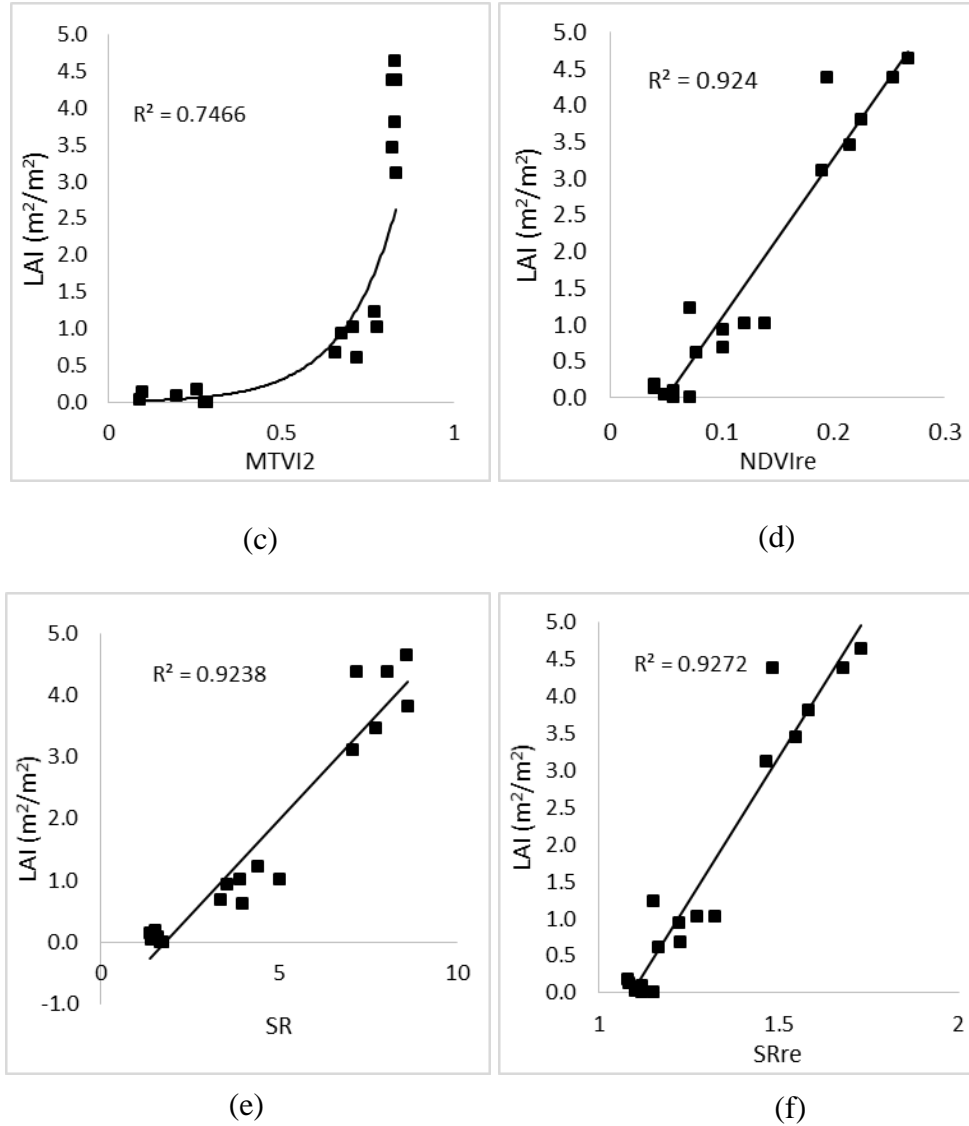
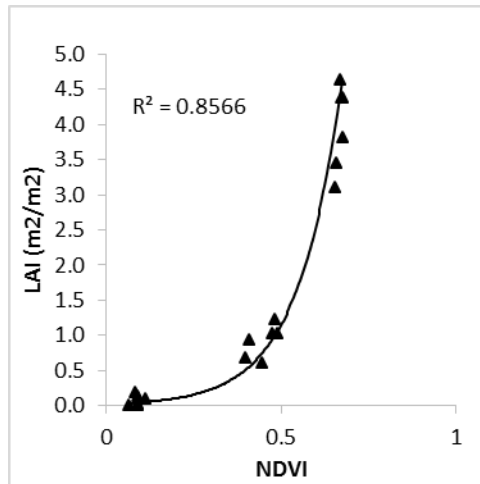


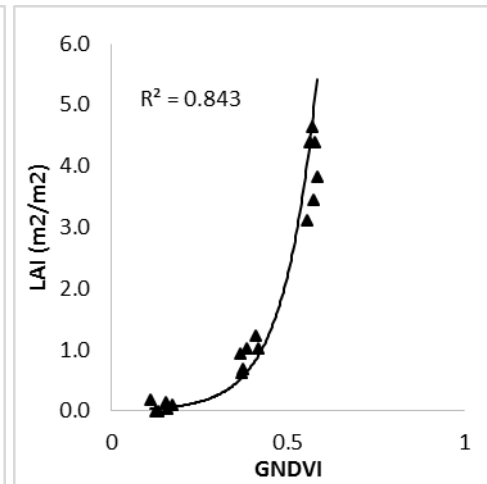
**Figure 2.11 Scatterplot between LAI (m<sup>2</sup>/m<sup>2</sup>) and UAV derived vegetation indices: (a) NDVI, (b) gNDVI, (c) MTVI2, (d) NDVIre, (e) SR, (f) SRre. The solid line is the best-fit function between all LAI measurements and vegetation indices.**

According to the VIs results of RapidEye images, the best fit function for the RapidEye derived NDVI, gNDVI, MTVI2 and NDVIre was exponential, but all these indices exhibited saturation when the LAI was greater than 3m<sup>2</sup>/m<sup>2</sup> in this study (Figure 2.11). The same was true for the UAV derived NDVI, gNDVI, and MTVI2. Both the RapidEye derived SR and SRre had linear best fit functions; the SR showed a saturation when LAI greater than 3m<sup>2</sup>/m<sup>2</sup>, and the SRre showed no saturation for the entire LAI range.

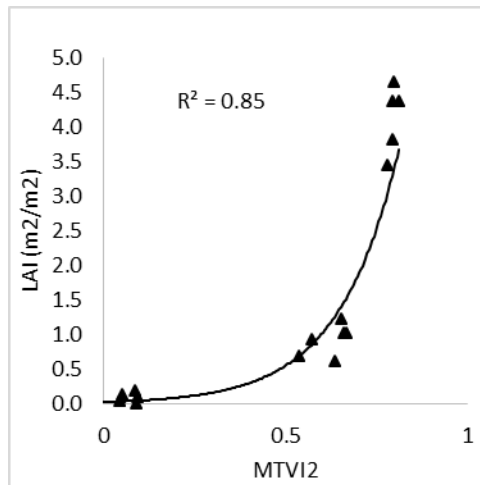




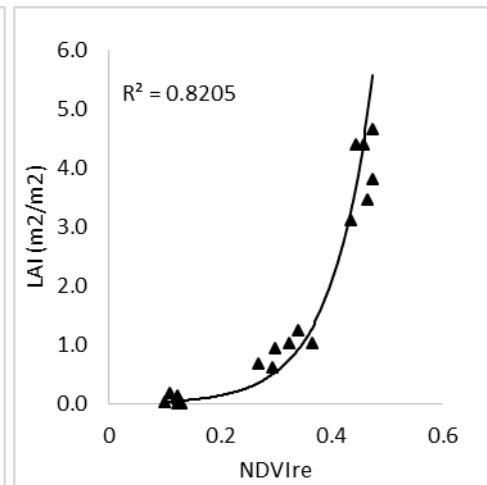
(a)



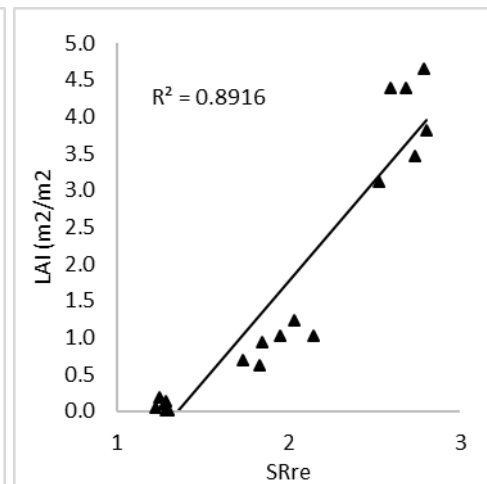
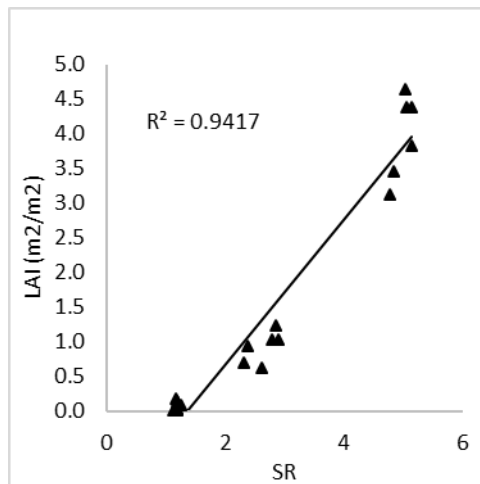
(b)



(c)



(d)



(e)

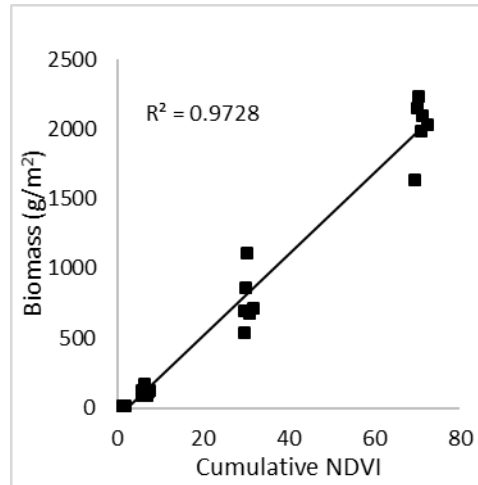
(f)

**Figure 2.12 Relationship between LAI ( $\text{m}^2/\text{m}^2$ ) and RapidEye derived vegetation indices: (a) NDVI, (b) gNDVI, (c) MTVI2, (d) NDVI<sub>re</sub>, (e) SR, (f) SR<sub>re</sub>. The solid line is the best-fit function between all LAI measurements and vegetation indices.**

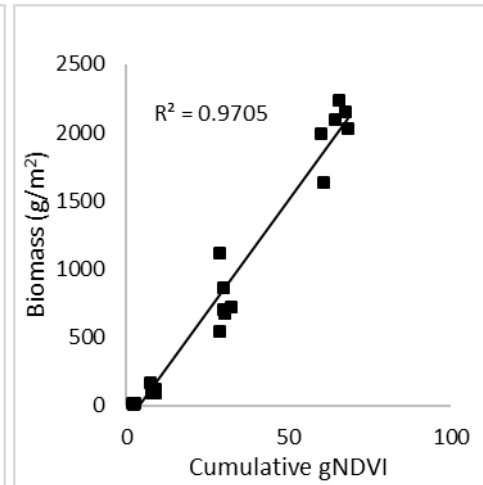
In contrast, the UAV derived NDVI, gNDVI, MTVI2, and SR had lower coefficient of determination than that of the RapidEye NDVI, gNDVI, MTVI2, and SR. Since the high spatial resolution UAV-based imagery had the capability to detect the slight difference of reflectance values changes which was affected by backs of leaves under wind action in a small area, minor changes on crop canopy could provide different results on VIs calculation, specifically on visual bands which had smaller values than red-edge and NIR bands. Meanwhile, although both the UAV and RapidEye multispectral imagery had similar band selection, the bands in the Tetracam camera, sensor on our UAV system had different bandwidth with the RapidEye, in this case it might provide different VIs results. The red-edge band selection for Tetracam (735-745nm) was different with the RapidEye bands (690-730nm) in this study. The UAV derived NDVI<sub>re</sub> and SR<sub>re</sub> showed no saturation and a higher coefficient of determination than that of RapidEye. In addition, these two VIs had a showed a linear relationship for the entire range of LAI measurements. These results demonstrated the red-edge band selection on Tetracam had the capability on long-term intra-field LAI estimation specifically on corn reproductive stage.

The cumulative VIs were used to estimate the dry biomass in this study which could provide a reasonable results based on crop growth principle. Because of biomass is the cumulative production of plant photosynthesis during the growing season, when LAI reached the maximum value and started to decrease at maturity stage, the biomass continuously increased. All cumulative vegetation indices showed a linear relationship with the corn total biomass (Figure 2.12). Although the UAV derived cumulative gNDVI, NDVI<sub>re</sub> and SR<sub>re</sub> showed saturation when the total biomass was greater than  $500\text{g}/\text{m}^2$ , they became sensitive again when the total biomass was greater than  $1500\text{g}/\text{m}^2$ . These three VIs were not sensitive to the difference of biomass at the end of July when biomass

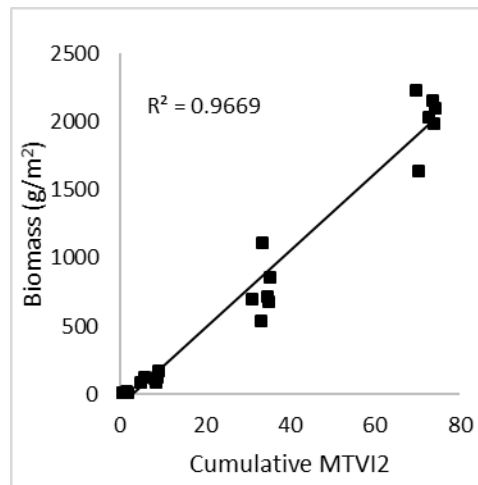
of corn had a larger variation range. The UAV derived cumulative NDVI and MTVI2 showed biomass saturation when it was greater than 500g/m<sup>2</sup>, and was invariant when the total biomass was greater than 1500g/m<sup>2</sup>. The UAV derived cumulative SR showed no saturation throughout the entire total biomass measurements in this study.



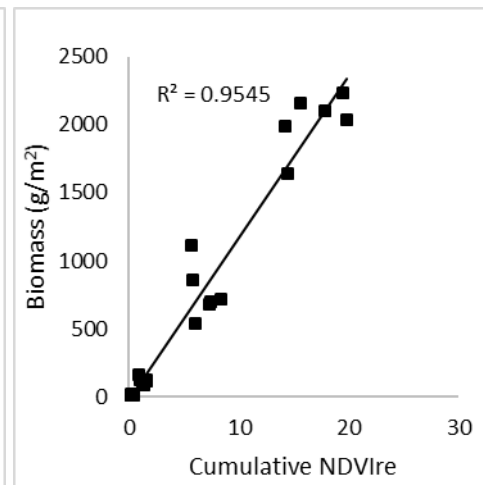
(a)



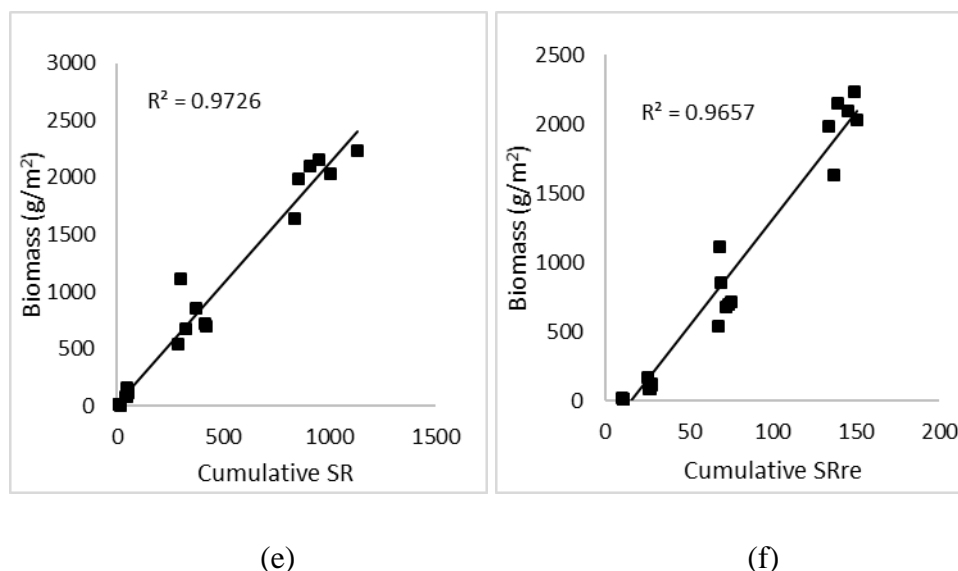
(b)



(c)

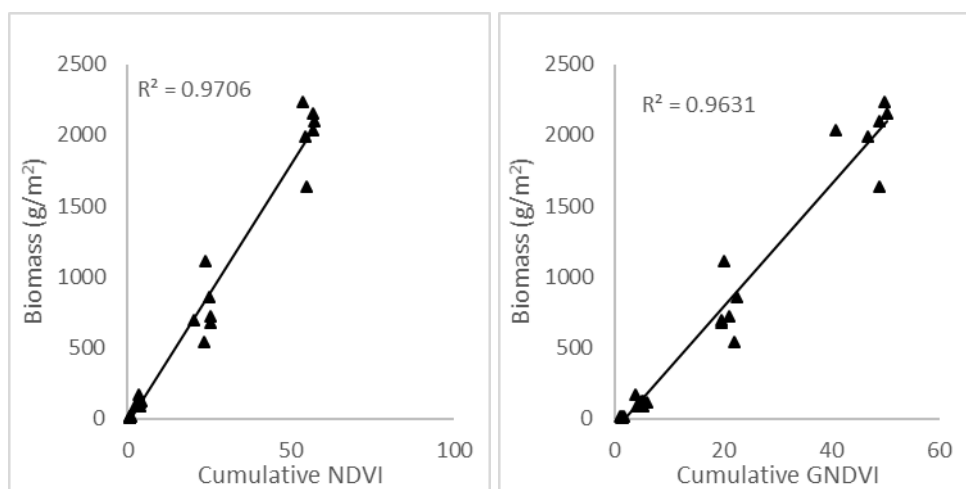


(d)



**Figure 2.13 Relationship between biomass and UAV cumulative vegetation indices: (a) cumulative NDVI, (b) cumulative GNDVI, (c) cumulative MTVI2, (d) cumulative NDVIre, (e) cumulative SR, (f) cumulative SRre. The solid line is the best-fit function between all biomass measurements and cumulative vegetation indices.**

Similar to UAV derived cumulative vegetation indices, the best fit function for RapidEye cumulative VIs was linear (Figure 2.13). Additionally, the RapidEye cumulative NDVI and MTVI2 has an invariant when the total biomass was greater than 500g/m<sup>2</sup> along the entire biomass measurement period. The RapidEye cumulative gNDVI, NDVIre, SR, and SRre showed saturation when total biomass was greater than 500g/m<sup>2</sup> but regained sensitivity when the total biomass reached greater than 1500g/m<sup>2</sup>.



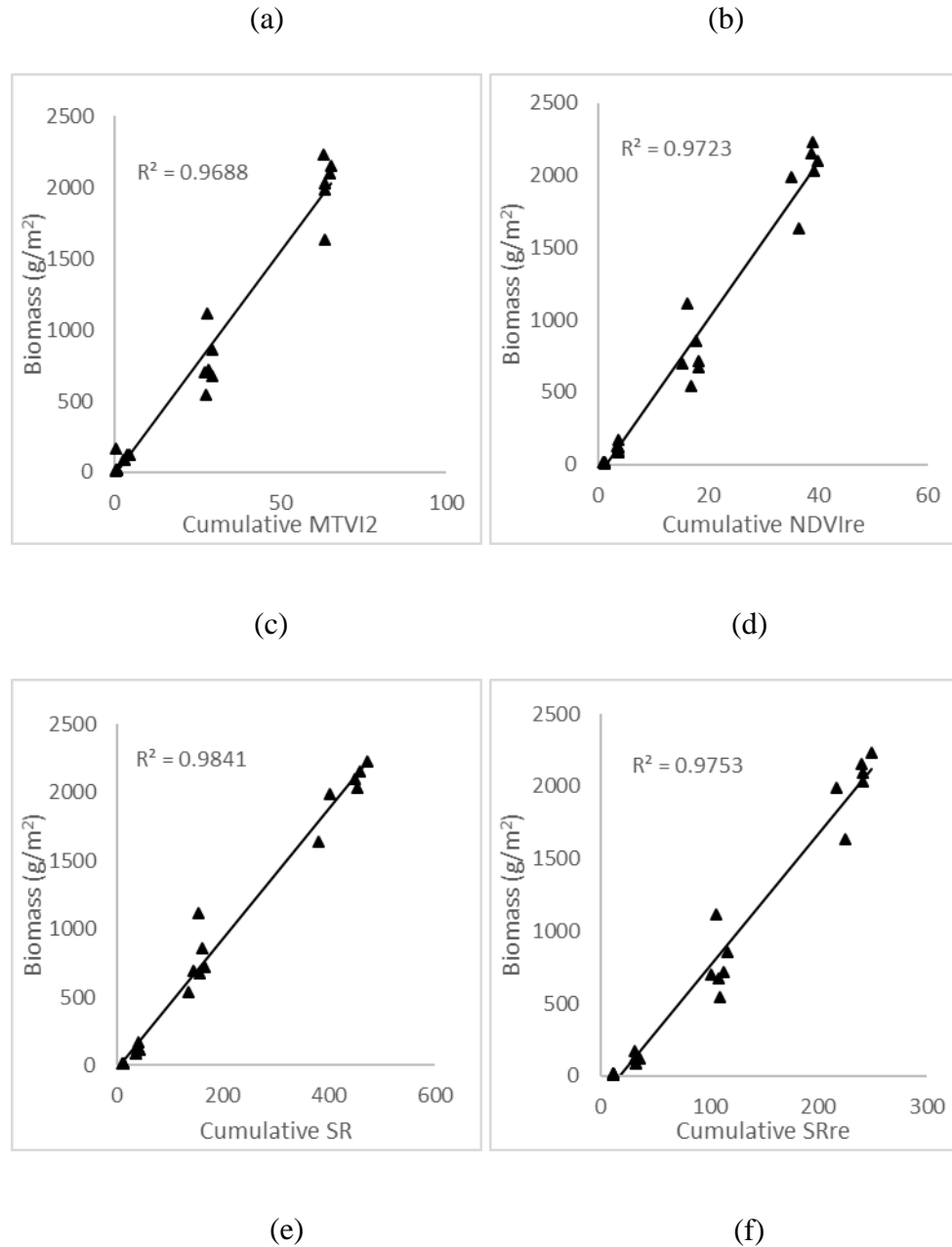


**Figure 2.14 Relationship between biomass and RapidEye cumulative vegetation indices: (a) cumulative NDVI, (b) cumulative GNDVI, (c) cumulative MTVI2, (d) cumulative NDVIre, (e) cumulative SR, (f) cumulative SRre. The solid line is the best-fit function between all biomass measurements and cumulative vegetation indices.**

Comparing with RapidEye cumulative VIs, the UAV derived cumulative VIs had similar performance against the biomass measurement during the crop growth from June to

September. Most of the UAV and RapidEye derived VIs had invariance responses to biomass when biomass was  $500 \text{ g/m}^2$ . Although, some of the VIs regained the sensitivity when biomass was greater than  $1500 \text{ g/m}^2$ , these VIs may provide an inaccurate biomass estimation at corn early growth stages. The UAV derived SR was sensitive along the entire biomass measurement from June to September. It demonstrated the UAV imagery could be used on corn biomass estimation and had better performance than the RapidEye with cumulative SR. All vegetation indices and cumulative vegetation indices results as shown in Appendix D.

## 2.4 Conclusions

This study provided a comprehensive temporal UAV-based multispectral imagery processing approach for corn field monitoring in eastern Ontario. An empirical line method was used to convert DNs to reflectance in UAV-based imagery. Afterwards, a single date NDVI comparison of the UAV-based and RapidEye imagery was calculated and used to demonstrate that UAV-based imagery can capture the intra-field variability in corn field. Meanwhile the red-edge indices of UAV-based imagery had a better potential in long-term LAI and biomass estimation for corn during the entire growth season. In contrast to the RapidEye derived NDVI results when corn was at reproductive stage in July, the UAV derived NDVI had a greater range of NDVI values and higher CV values which could provide more detail and information on corn real-time monitoring. Additionally, the UAV imagery captured the variation (NDVI) of the two (50% and 100%) nitrogen treatment zones well.

Both the UAV and RapidEye derived VIs against corn LAI value had good correlation. However, most of VIs, except RapidEye derived  $\text{SR}_{\text{re}}$  and UAV derived  $\text{NDVI}_{\text{re}}$ ,  $\text{SR}$ , and  $\text{SR}_{\text{re}}$ , had saturation problems when LAI was greater  $3 \text{ m}^2/\text{m}^2$ . The UAV derived  $\text{NDVI}_{\text{re}}$  and  $\text{SR}_{\text{re}}$  showed sensitivity to LAI from emergence to LAI up to  $5 \text{ m}^2/\text{m}^2$  and these two red-edge indices had a better coefficient of determination than that of the RapidEye. The cumulative vegetation indices performed well for the estimation of corn total dry biomass with both the UAV and RapidEye. Except for the UAV cumulative SR, most of the cumulative VIs saturated when the total biomass was around  $500 \text{ g/m}^2$ . The

UAV cumulative SR showed no saturation for the entire biomass measurement in this study. The better performance on remote sensing products of LAI and biomass revealed that the UAV-based imagery had a greater sensitivity to crop biophysical variables compared with the RapidEye imagery throughout the entire growing season. Likewise, the broader range of NDVI values and higher coefficient of variance showed the UAV-based imagery had a greater detection capability than that of the RapidEye imagery. In summary, there is great potential in using the UAV for intra-field variability detection and seasonal crop growth monitoring.

## 2.5 References:

- Agüera, F., Carvajal, F., & Pérez, M. (2012). Measuring sunflower nitrogen status from an Unmanned Aerial Vehicle-based system and an on the ground device. *ISPRS - International Archives of the Photogrammetry, Remote Sensing and Spatial Information Sciences*, XXXVIII-1/, 33–37. <http://doi.org/10.5194/isprsarchives-XXXVIII-1-C22-33-2011>
- Bendig, J., Bolten, A., Bennertz, S., Broscheit, J., Eichfuss, S., & Bareth, G. (2014). Estimating biomass of barley using crop surface models (CSMs) derived from UAV-based RGB imaging. *Remote Sensing*, 6(11), 10395–10412. <http://doi.org/10.3390/rs61110395>
- Berni, J. A. J., Zarco-Tejada, P. J., Suárez, L., González-Dugo, V., & Fereres, E. (2009). Remote sensing of vegetation from UAV platforms using lightweight multispectral and thermal imaging sensors. *Int. Arch. Photogramm. Remote Sens. Spatial Inform. Sci.*, 38, 6 pp. <http://doi.org/10.1007/s11032-006-9022-5>
- Berni, J., Zarco-Tejada, P. J., Suarez, L., & Fereres, E. (2009). Thermal and narrowband multispectral remote sensing for vegetation monitoring from an unmanned aerial vehicle. *IEEE Transactions on Geoscience and Remote Sensing*, 47(3), 722–738. <http://doi.org/10.1109/TGRS.2008.2010457>
- Buchhorn, M., Petereit, R., & Heim, B. (2013). A manual transportable instrument platform for ground-based spectro-directional observations (ManTIS) and the resultant hyperspectral field goniometer system. *Sensors (Switzerland)*, 13(12), 16105–16128. <http://doi.org/10.3390/s131216105>
- Chen, P., Haboudane, D., Tremblay, N., Wang, J., Vigneault, P., & Li, B. (2010). New spectral indicator assessing the efficiency of crop nitrogen treatment in corn and wheat. *Remote Sensing of Environment*, 114(9), 1987–1997. <http://doi.org/10.1016/j.rse.2010.04.006>
- Coast, G., McCabe, M. F., Houborg, R., & Rosas, J. (2015). The potential of unmanned



- aerial vehicles for providing information on vegetation health. *21st International Congress on Modelling and Simulation*, 1399–1405.
- Dean, C., Warner, T. A., & McGraw, J. B. (2000). Suitability of the DCS460c colour digital camera for quantitative remote sensing analysis of vegetation. *ISPRS Journal of Photogrammetry and Remote Sensing*, 55(2), 105–118.  
[http://doi.org/10.1016/S0924-2716\(00\)00011-3](http://doi.org/10.1016/S0924-2716(00)00011-3)
- Gevaert, C. M., Tang, J., Suomalainen, J., & Kooistra, L. (2014). *Combining Hyperspectral UAV and Multispectral FORMOSAT-2 Imagery for Precision Agriculture Applications (Published master thesis)*. Lund University, Lund, Sweden.
- Gunlu, A., Ercanli, I., Baskent, E. Z., & G., C. (2014). Estimating aboveground biomass using landsat TM imagery: A case study of Anatolian Crimean pine forests in Turkey. *Annals of Forest Research*, 57(2), 289–298.  
<http://doi.org/10.15287/afr.2014.278>
- Haboudane, D., Miller, J. R., Pattey, E., Zarco-Tejada, P. J., & Strachan, I. B. (2004). Hyperspectral vegetation indices and novel algorithms for predicting green LAI of crop canopies: Modeling and validation in the context of precision agriculture. *Remote Sensing of Environment*, 90(3), 337–352.  
<http://doi.org/10.1016/j.rse.2003.12.013>
- Hou, X., Gao, S., Niu, Z., & Xu, Z. (2014). Extracting grassland vegetation phenology in North China based on cumulative SPOT-VEGETATION NDVI data. *International Journal of Remote Sensing*, 35(9), 3316–3330.  
<http://doi.org/10.1080/01431161.2014.903437>
- Huang, J., Wang, X., Li, X., Tian, H., & Pan, Z. (2013). Remotely sensed rice yield prediction using multi-temporal NDVI data derived from NOAA's-AVHRR. *PLoS ONE*, 8(8), 1–13. <http://doi.org/10.1371/journal.pone.0070816>
- Huete, A. R. (1988). A soil-adjusted vegetation index (SAVI). *Remote Sensing of Environment*, 25(3), 295–309. [http://doi.org/10.1016/0034-4257\(88\)90106-X](http://doi.org/10.1016/0034-4257(88)90106-X)

- Hunt, E. R., Hively, W. D., et al.. (2008). Remote sensing of crop Leaf Area Index using Unmanned Airborne Vehicles. *October, 17*, 18–20. Retrieved from <http://www.asprs.org/publications/proceedings/pecora17/0018.pdf>
- Jin, Y., Yang, X., Qiu, J., Li, J., Gao, T., Wu, Q. et al.. (2014). Remote sensing-based biomass estimation and its spatio-temporal variations in temperate Grassland, Northern China. *Remote Sensing*, 6(2), 1496–1513. <http://doi.org/10.3390/rs6021496>
- Kalisperakis, I., Stentoumis, C., Grammatikopoulos, L., & Karantzalos, K. (2015). Leaf area endex estimation in vineyards from UAV hyperspectral Data, 2D emage mosaics and 3D canopy surface models. *ISPRS - International Archives of the Photogrammetry, Remote Sensing and Spatial Information Sciences*, XL-1/W4, 299–303. <http://doi.org/10.5194/isprsarchives-XL-1-W4-299-2015>
- Kelcey, J., & Lucieer, A. (2012). Sensor correction of a 6-band multispectral imaging sensor for UAV remote sensing. *Remote Sensing*, 4(5), 1462–1493. <http://doi.org/10.3390/rs4051462>
- Kross, A., McNairn, H., Lapen, D., Sunohara, M., & Champagne, C. (2015). Assessment of RapidEye vegetation indices for estimation of leaf area index and biomass in corn and soybean crops. *International Journal of Applied Earth Observation and Geoinformation*, 34(1), 235–248. <http://doi.org/10.1016/j.jag.2014.08.002>
- Lelong, C. C. D., Burger, P., Jubelin, G., Roux, B., Labbé, S., & Baret, F. (2008). Assessment of unmanned aerial vehicles imagery for quantitative monitoring of wheat crop in small plots. *Sensors*, 8(5), 3557–3585. <http://doi.org/10.3390/s8053557>
- Levin, N., Ben-Dor, E., & Singer, a. (2005). A digital camera as a tool to measure colour indices and related properties of sandy soils in semi-arid environments. *International Journal of Remote Sensing*, 26, 5475–5492. <http://doi.org/10.1080/01431160500099444>

- Liu, J., Miller, J. R., Pattey, E., Haboudane, D., Strachan, I. B., & Hinthner, M. (2004). Monitoring Crop Biomass Accumulation Using Multi-temporal Hyperspectral Remote Sensing Data. *Geoscience and Remote Sensing Symposium, 2004. IGARSS '04. Proceedings. 2004 IEEE International*, 3(C), 1637–1640. Retrieved from [http://ieeexplore.ieee.org/xpl/articleDetails.jsp?tp=&arnumber=1370643&contentType=Conference+Publications&searchField=Search\\_All&queryText=Remote+Sensing+agriculture+food](http://ieeexplore.ieee.org/xpl/articleDetails.jsp?tp=&arnumber=1370643&contentType=Conference+Publications&searchField=Search_All&queryText=Remote+Sensing+agriculture+food)
- Nebiker, S., Annen, A., Scherrer, M., & Oesch., D. (2008). A light-weight multispectral sensor for micro uav – opportunities for very high resolution airborne remote sensing. *The International Archives of the Photogrammetry, Remote Sensing and Spatial Information Sciences*, XXXVII, 1193–1200.
- Nguy-Robertson, A., Gitelson, A., Peng, Y., Vi??a, A., Arkebauer, T., & Rundquist, D. (2012). Green leaf area index estimation in maize and soybean: Combining vegetation indices to achieve maximal sensitivity. *Agronomy Journal*, 104(5), 1336–1347. <http://doi.org/10.2134/agronj2012.0065>
- Shang, J., Liu, J., Ma, B., Zhao, T., Jiao, X., Geng, X., ... Walters, D. (2015). Mapping spatial variability of crop growth conditions using RapidEye data in Northern Ontario, Canada. *Remote Sensing of Environment*, 168, 113–125. <http://doi.org/10.1016/j.rse.2015.06.024>
- Wang, C., & Myint, S. W. (2015). A simplified empirical line method of radiometric calibration for small unmanned aircraft systems-based remote sensing. *IEEE Journal of Selected Topics in Applied Earth Observations and Remote Sensing*, 8(5), 1876–1885. <http://doi.org/10.1109/JSTARS.2015.2422716>
- Weidner, V. R., & Hsia, J. J. (1981). Reflection properties of pressed polytetrafluoroethylene powder. *Journal of the Optical Society of America*, 71(7), 856–861. <http://doi.org/10.1364/JOSA.71.000856>
- Zarco-Tejada, P. J., González-Dugo, V., & Berni, J. A. J. (2012). Fluorescence, temperature and narrow-band indices acquired from a UAV platform for water stress

detection using a micro-hyperspectral imager and a thermal camera. *Remote Sensing of Environment*. 117.

## Chapter 3

### 3 Estimation of Intra-field Winter Wheat Nitrogen Weight and Yield Using UAV-Based Imagery and Ground Calculated Biomass

#### 3.1 Introduction

Precision farming is an approach to agriculture management that achieves maximum efficiency with appropriate fertilizer and water applications (Krishna, 2013). One of the requirements for successful precision farming is the accurate monitoring of nitrogen content and prediction of yield from models based on early growth stage parameters. With the development of remote sensing technology, satellite imagery has been analyzed in numerous studies to monitor nitrogen content and predict crop yield (Clevers, 1997; Doraiswamy et al., 2003; Jing-feng Huang et al., 2002). The use of traditional optical satellite remote sensing techniques on small farm fields to determine intra-field variation has several disadvantages that are discussed, and in this study, a new solution for remote sensing monitoring and prediction using Unmanned Aerial Vehicle (UAV)-based imagery is introduced.

Nitrogen is an essential plant nutrient during the growing season for crops and is the largest agricultural input in current cropping systems (Adam K. et al., 2007). The timing and amount of nitrogen fertilizer application affect the final production and economic benefits (Fageria, 2014). Traditional analysis of crop nitrogen requirements uses chemical methods, such as plant and soil sample combustion methods in the laboratory, which are time consuming and costly. Additionally, with these methods, instantaneous and wide-range monitoring of crops is difficult to achieve. For an on-the-go method to monitor crop nitrogen, many studies attempted to use remote sensing to collect images for a large area (Clevers A.A., 2012; D.G. Sullivan P.L. Mask, D. Rickman, J. Luvall and J.M. Wersinger, 2004; E. Raymond Hunt JR. Craig S.T. Daughtry, James McMurtrey III, and Charles L. Walthall, 2005). Nitrogen is a primary component of chlorophyll that has strong absorption in blue and red light. Therefore, remote sensing studies can use spectral

vegetation indices to evaluate the concentration of chlorophyll, thereby calculate nitrogen content.

Common remotely sensed nitrogen analysis focuses on vegetation indices derived from optical multispectral and hyperspectral images such as ratio vegetation index (RVI), nitrogen reflectance index (NRI), and double-peak canopy nitrogen index (DCNI) (Chen et al., 2010). Typically, multispectral satellite imagery provides limited band combinations on crop nitrogen monitoring in remote sensing studies. Different vegetation indices and methodologies were developed to estimate the nitrogen content in different stages of crop growth in past studies (D.G. Sullivan P.L. Mask, D. Rickman, J. Luvall and J.M. Wersinger, 2004)(Caturegli et al., 2015). Hyperspectral imagery provides the ideal data for crop monitoring in remote sensing studies because this imagery has a higher spectral resolution and provides more spectral information on plants (Sims & Gamon, 2002)(Hansen & Schjoerring, 2003). In many studies, crop N was evaluated at a specific wavelength at the scale of the leaf (Hansen & Schjoerring, 2003; Rodriguez, Fitzgerald, Belford, & Christensen, 2006), and many vegetation indices have also been developed to estimate plant N and chlorophyll based on ground hyperspectral measurements (Barnes et al., 2000; Gitelson & Merzlyak, 1994).

Estimation of crop yield is an important issue in food security, and these estimates help determine crop prices and manage crop production. In the USA, the Large Area Crop Inventory Experiment (LACIE) was conducted to estimate wheat production worldwide using the Landsat Multispectral Scanner (MSS) system (Erickson, 1984). In addition to global monitoring and estimation of crop yields with remote sensing, most studies focused on a specific area and crop and used different remote sensing technologies. Although the prediction of crop yields has been developed, the application of early yield prediction is still restricted by remote sensing data collection and crop types. When satellite imagery is used to monitor nitrogen, requirements of intra-field monitoring for a small-scale farm field are difficult to achieve. Hyperspectral imagery is expensive and therefore highly frequent monitoring in one crop season is not practical. Most studies that monitor crop nitrogen using hyperspectral imagery are ground-based methods. However, for multispectral satellite imagery, the problem is revisit timing and cloud cover during

monitoring because optical satellite data cannot “see through” clouds. Thus, the availability is largely affected by weather conditions and time monitoring of crops (weekly) may be impossible. With satellite data, spatial resolution is also reduced for a small-scale field, which is not adequate for within-field crop monitoring. With the current methods based on multispectral and hyperspectral data, monitoring crop nitrogen using remote sensing techniques is possible, but the application is difficult in real time and for field-scale management of crops.

In general, optical remote sensing methods for crop yield estimation are divided into two primary groups in terms of the data resource. One group combines crop growth and plant physiological models with remote sensing data to develop a crop yield model (Baez-gonzalez, Chen, Tischarena-lopez, & Srini, 2002; Fang, Liang, & Hoogenboom, 2011; Johnson, 2014; Prasad, Chai, Singh, & Kafatos, 2006; Rojas, 2007). To apply this method, the entire crop growth season must be observed to collect the agrometeorological and plant physiological parameter data. Additionally, the application of this method requires an understanding of remote sensing data processing and also an in-depth background in plant physiology. The other group uses remote sensing data and crop yields to produce a direct mathematical relation to estimate crop yield, which is based on the assumption that the vigor of the crop canopy has a simple, direct relation to crop yield (Hamar, Ferencz, Lichtenberger, Tarcsai, & Ferencz-Arkos, 1996)(Hamar et al., 1996). This method is more convenient and it has the advantages of an easier process of data collection. However, this method still requires the collection of temporal series of data and is not universally applicable to different crops and years. Collection of multiple remote sensing data is a difficult process in a weather complicated region, such as our test area of Melbourne, Ontario, Canada, which had many days covered by clouds. Moreover, both methods are applied in large-scale predictions of crop yield. Predicting crop yield is difficult in a small-scale farm because the intra-field variation is difficult to determine by low resolution satellite images. Meanwhile, the common ground yield data was made up by many single farms yield data which is hard to represent intra-field yield variations. Although, the spatial yield distribution data collected by farmers’ harvester has been applied in precision farming management to help farmer to monitor the intra-field yield

distribution, this type of spatial yield distribution data has not been addressed in remote sensing study in yield prediction yet.

The UAV has been developed rapidly in recent years. Depending on the different types of sensor attached to an UAV, there are many different applications. The UAV has many advantages for agriculture research: 1) the UAV provides higher spatial and temporal resolution than satellite images; 2) the UAV can obtain results under cloud cover, whereas satellite images are limited by cloud visibility, and 3) the entire UAV system is cheaper than satellite images. Because of these advantages, the UAV has a great potential for remote sensing applications to collect high spatial and temporal imagery in agriculture to achieve intra-field crop monitoring. The UAV has been used in many studies to determine vegetation indices, monitor crops health status and predict crop yield with one-day optical imagery collected by the UAV system; some studies demonstrated the potential of the UAV to estimate crop LAI and yield in practices and capability of intra-field monitoring (E. Raymond Hunt JR. Craig S.T. Daughtry, James McMurtrey III, and Charles L. Walthall, 2005; Lelong et al., 2008; Swain, Thomson, & Jayasurya, 2010). The well-developed UAV technique turns the sensor into the key element for the application of the UAV in agriculture. Currently, modified digital and array multispectral cameras are the primary portable and light sensors used with UAV system. Modified digital cameras have broader bands that can only acquire a few simple vegetation indices, whereas array multispectral cameras are much more complicated in operation and too expensive currently to be widely used by individual farmers. Moreover, the images captured by both camera will need image normalization process or radiometric correction to ensure the data can be used in temporal crop analysis. Therefore, in order to develop an approach for individual farms' intra-field farm management with the UAV system, a practicable and affordable modified digital camera was used to collect UAV-based blue-green-NIR imagery in this study.

Additionally, the ground reference measurements will need a large number of samples to estimate and validate the model to represent the relationship between nitrogen content or final yield and the vigor of crop canopy directly within a small area,. An alternative approach is to estimate plant biomass using a calculated model with a set of plant



structural parameters including fractional vegetation cover (fCover), plant height and plant bulk density. This alternative approach has been investigated and evaluated in many previous studies (Krebs et al., 2003; Muukkonen et al., 2006; Rottgermann, Steinlein, Beyschlag, & Dietz, 2000), and a linear relationship is found between the fraction of cover and biomass or LAI for low, open arctic vegetation (Wenjun et al., 2009). Instead of a time consuming and destructive biomass measurements, this biomass estimation method could provide a large number samples to validate the total nitrogen weight and yield prediction model using UAV-based blue-green-NIR imagery.

## 3.2 Materials and Methods

### 3.2.1 Study sites

The study sites were four winter wheat fields located in Melbourne, Ontario, Canada. Three wheat fields belonged to Brenair Farm Inc., and one winter wheat field belonged to Brent Farm INC. These two farm companies are the clients of A&L Canada Laboratories Inc., which provides complete soil and plant analyses and fertilization recommendations for farmers and fertilizer dealers in Ontario, Quebec, Alberta, Saskatchewan and Manitoba. According to soil analyses, the soil type and nutrient levels were similar at the four sites; therefore, these two farm companies adopted the identical fertilization recommendations for winter wheat in this study.

Map of four wheat study sites in Melbourn, Southwestern Ontario

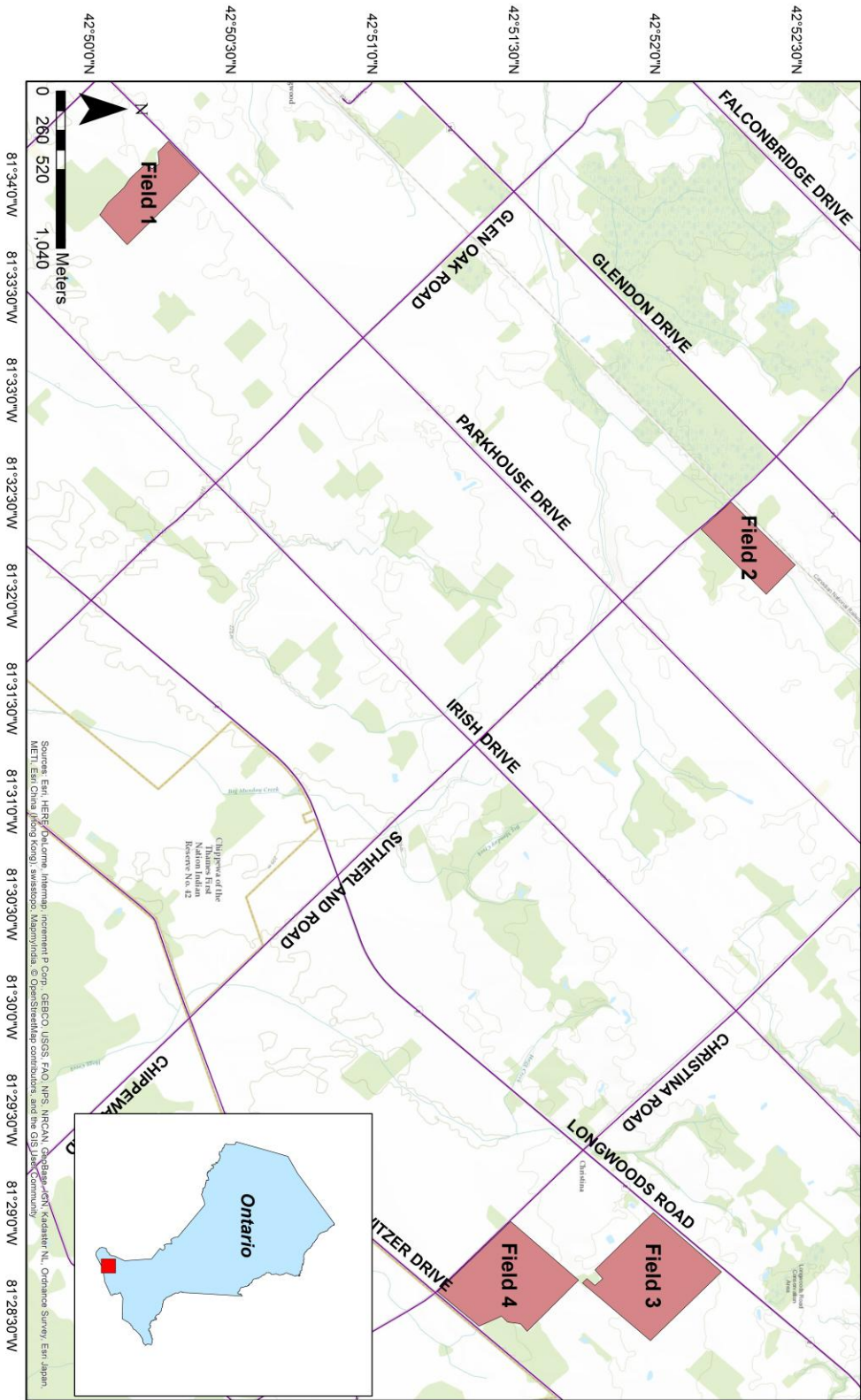


Figure 3.1 Map of four wheat study sites.

The four winter wheat fields were planted to soybean in 2014. In 2015, no-till farming was used at the study sites, with the identical seed density and a row distance of 18 centimeter. Eight points were sampled in each field, and the distance between each sampling point was greater than 50 m. Figure 3.1 shows the location of each study site. Field data were collected at our study sites from early May to early July on four dates: May 21, May 29, June 19, and July 2. The test period covered the phenology of winter wheat growth stage BBCH between 40 and 99. BBCH officially stands for “Biologische Bundesanstalt, Bundessortenamt und Chemische industrie.” Which is a scale used to identify the phenological development stages of a plant. The complete data set included aerial images captured by an UAV with a modified digital camera, wheat foliage nitrogen content, plant leaf area index, plant height, and wheat biomass.

### 3.2.2 Field data collection

Three height measurements were recorded at each sample point, with the average height representing the height of plants at each point. Biomass was measured four times in each study site on the identical day as the UAV flight and was determined by destructive sampling in a 0.5 m by 0.5 m area at each sample point. Plant biomass was measured after samples were oven-dried at 80°C for 72 h, with the values rescaled to g per m<sup>2</sup>.

Wheat tissue samples were collected on four days: May 21, May 29, June 19 and July 2. At each sample point, 20 random wheat leaves and stem tissue samples were collected within a 2 m radius. All samples were sent to A&L Canada Laboratories on the identical day as the sampling for total nitrogen analysis. Tissue samples were oven-dried overnight at 80°C and ground with a cyclone grinder to pass through a 1 mm sieve. Sample powders were analyzed with a LECO (Laboratory Equipment Corporation) FP628 Nitrogen Determinator using a combustion method to measure the total nitrogen content. Nitrogen content was expressed as a percentage.

Plant area index (PAI) and fractional vegetation cover (fCover) were calculated by an indirect method that used hemispherical canopy photography at each sample point. The hemispherical wheat canopy photographs were acquired with a Nikon S300s DLSR camera and a 10.5 mm fisheye lens. At each sample point, two rows of images contained

7 images for each row; images were captured at a height of one meter above the wheat canopy. The digital photos were analyzed with CANEYE version 6 (INRA-UAPV, France) to calculate PAI and fCover. All data shows in Appendix E.

### 3.2.3 UAV-based blue-green-NIR imagery processing

UAV flights were on three days: May 21, June 19 and July 2 in 2015. A modified digital Canon PowerShot S110 12 megapixel camera was used to capture blue-green-NIR images. The camera was fitted on a fixed wing UAV that was developed by A&L Canada Inc. to collect images for entire fields. The UAV was controlled to follow a pre-programmed flight route generated by the ground control software Mission Planner (Appendix F). The UAV collected blue-green-NIR geo-tagged digital images at the altitude of 150 m above ground level (AGL) with a 1 second interval between image capture. The images were collected between 10:00 a.m. and 2:00 p.m. under cloud-free conditions. To obtain high quality orthomosaic images for future analyses, the degree of overlap in the route direction was greater than 80%; the overlap degree in the lateral direction was greater than 60% for each test flight. After collection, images were mosaicked by image processing software Agisoft (Appendix G) and imported into ArcGIS for future processing of images to calculate the Green Normalized Difference Vegetation Index (GNDVI) (Equation 3.1) (Merzlyak, 1998).

$$GNDVI = (DN_{NIR} - DN_{green}) / (DN_{NIR} + DN_{green}) \quad \text{Equation 3.1}$$

The total sample numbers in this study are shown in Table 3.1. Four aerial images for the four test wheat field as shown in Figure 3.2. The aerial images were composited by blue, green and NIR bands.

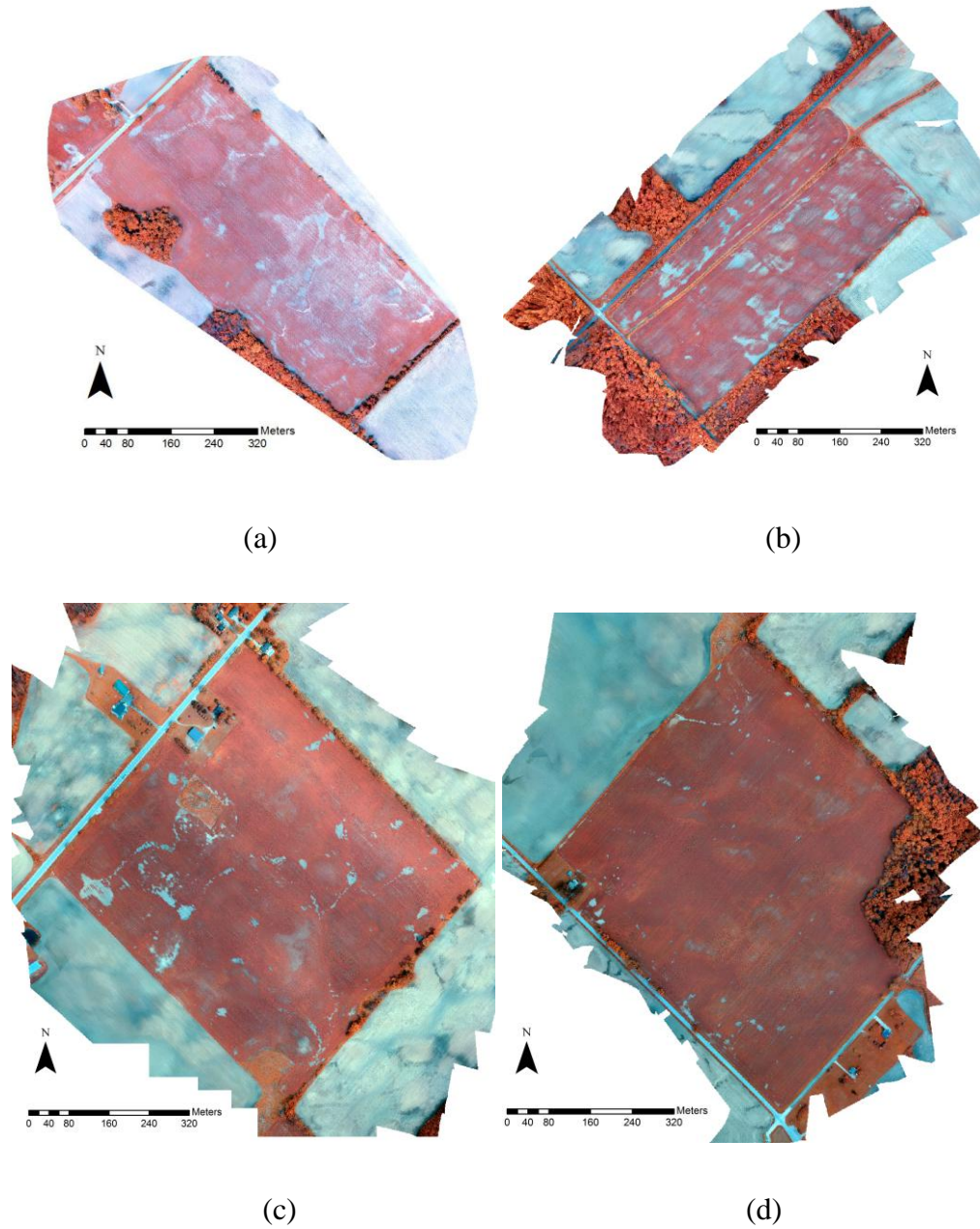


**Figure 3.2 Mosaicked UAV-based aerial images (NIR shows as red, blue shows as blue, green shows as green) for all test field, (a) field one, (b) field two, (c) field three, (d) field four.**

**Table 3.1 Date and total sample number for data collection.**

<b>Date</b>	<b>PAI</b>	<b>Plant Height</b>	<b>Nitrogen Content</b>	<b>Dry biomass</b>	<b>UAV imagery</b>
<b>21-5-2015</b>	34	34	34	4	444
<b>29-5-2015</b>	32	-	32	-	334
<b>19-6-2015</b>	33	33	25	4	357
<b>2-7-2015</b>	33	33	25	8	336

### 3.2.4 Spatial yield distribution

Brent and Brenair Farm companies provided spatial variable yield data at the end of the wheat harvest. A grain yield monitor was used to collect spatial yield data which display the yield distribution in a spatial color coded map. This device was installed on a combine harvester and is designed to measure the harvested mass flow, moisture content, and geographic information, in addition to providing high resolution and accurate yield data. The wheat spatial yield was a composite of many points, with the wheat yield in units of bushels/acre. The red points near the boundary were caused by a second measurement with the combine harvester (Figure 3.3). The spatial yield data were composed of many points that contained the yield value. All data were processed in ArcGIS for removal of duplicate points, resampling, and data extraction.



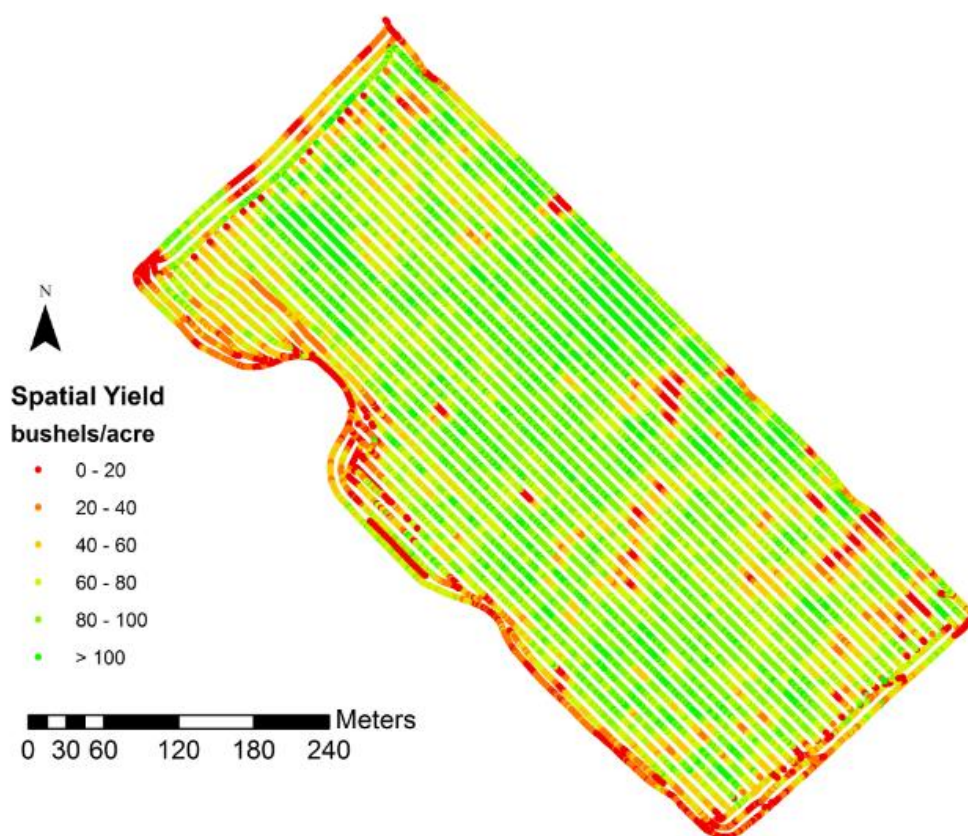


**Figure 3.3 Map of spatial yield. All data were in a point format, with the unit bushels/acre.**

### 3.2.5 Model development

Past study has demonstrated to plant height and plant structure were strongly correlated with plant dry biomass for arctic vegetation (Wenjun et al., 2009). Therefore, we tested for correlations between wheat plant height  $\times$  wheat leaf properties and biomass at our study sites. We then used biomass and wheat foliage nitrogen content to calculate the total nitrogen weight per unit area. We collected data on wheat height and dry biomass and captured hemispherical photographs in our four wheat field for this method.

GNDVI was used to monitor the greenness of vegetation, with the greenness of plant leaves determined by the concentration of chlorophyll, the green pigment of plants. Additionally, chlorophyll contains four nitrogen atoms that form bonds to magnesium.

(Noyd R. et al. 2016) Therefore, GNDVI was used to determine nitrogen content in this study. Additionally, a linear relationship between wheat dry biomass and fraction of cover  $\times$  plant height (biomass<sub>fCover</sub> model) was described by the following equation:

$$Y = \alpha \times H \times fCover, \quad \text{Equation 3.2}$$

and a linear relationship between wheat dry biomass and PAI  $\times$  plant height (biomass<sub>PAI</sub> model) was described by the following equation:

$$Y = b \times H \times PAI \quad \text{Equation 3.3}$$

These models were analyzed and tested in this study.

In the models,  $H$  is plant height in m,  $PAI$  is plant area index in  $m^2/m^2$ ,  $fCover$  is fractional vegetation cover as a %, and  $\alpha$  and  $b$  is the slope of the linear relationship with a 0 intercept and also represents biomass bulk density (Wenjun et al., 2009). After analyses, a simple regression method was applied to determine the relationship between GNDVI and biomass  $\times$  N content to determine total nitrogen content per unit area.

To determine the possibility of predicting winter wheat final yield using GNDVI values, the relationships between GNDVI and biomass<sub>fCover</sub> and between GNDVI and biomass<sub>PAI</sub> were determined. Temporal biomass data were derived from temporal GNDVI data. Then, multiple linear regression was performed to determine the relationship between temporal GNDVI from May to June and the final spatial yield. Figure 3.4 shows the overall flowchart for data processing and models establishment.



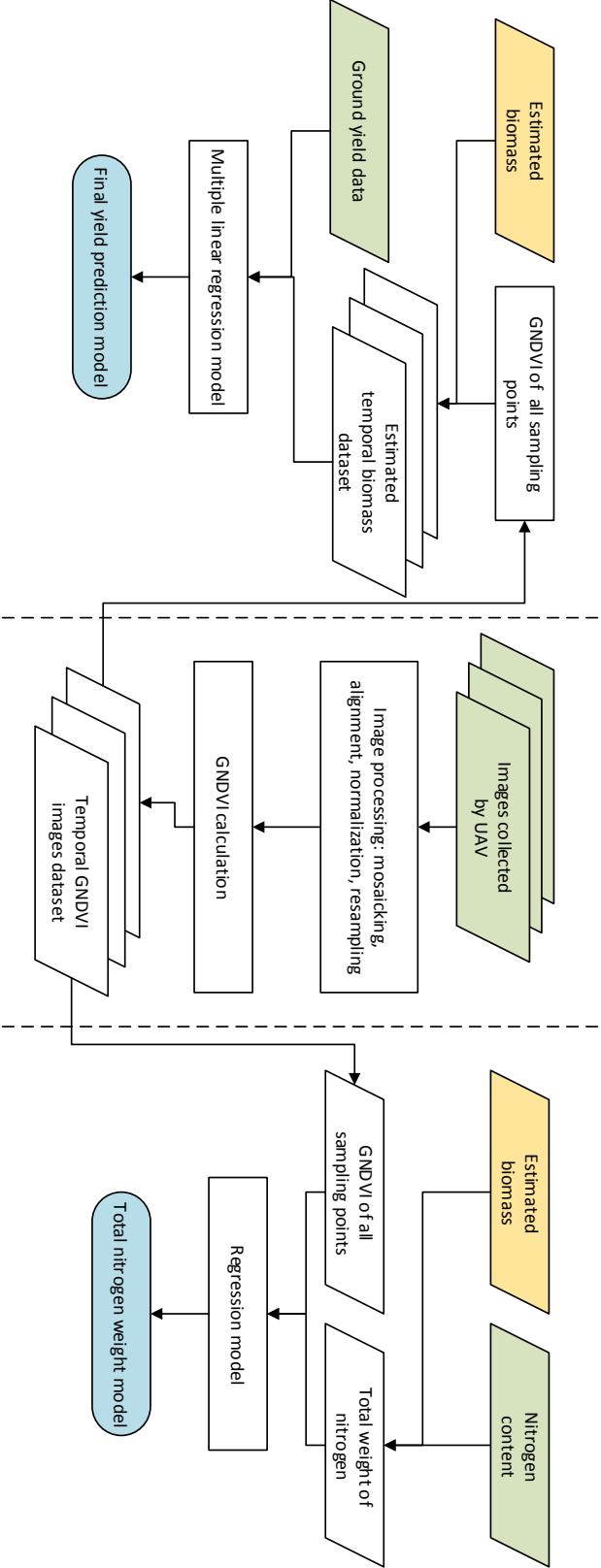
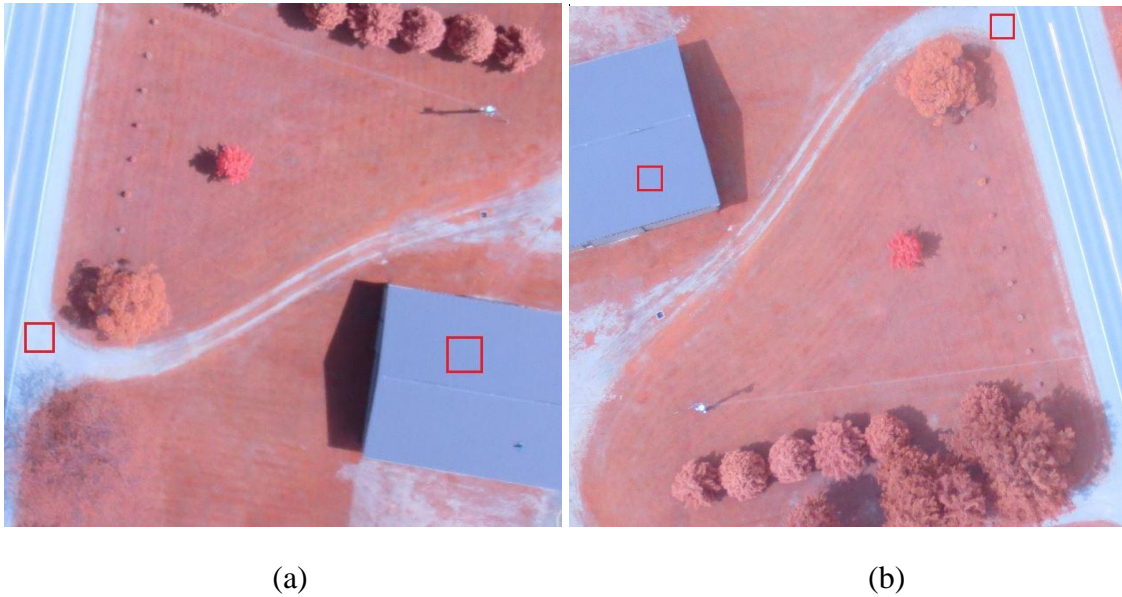


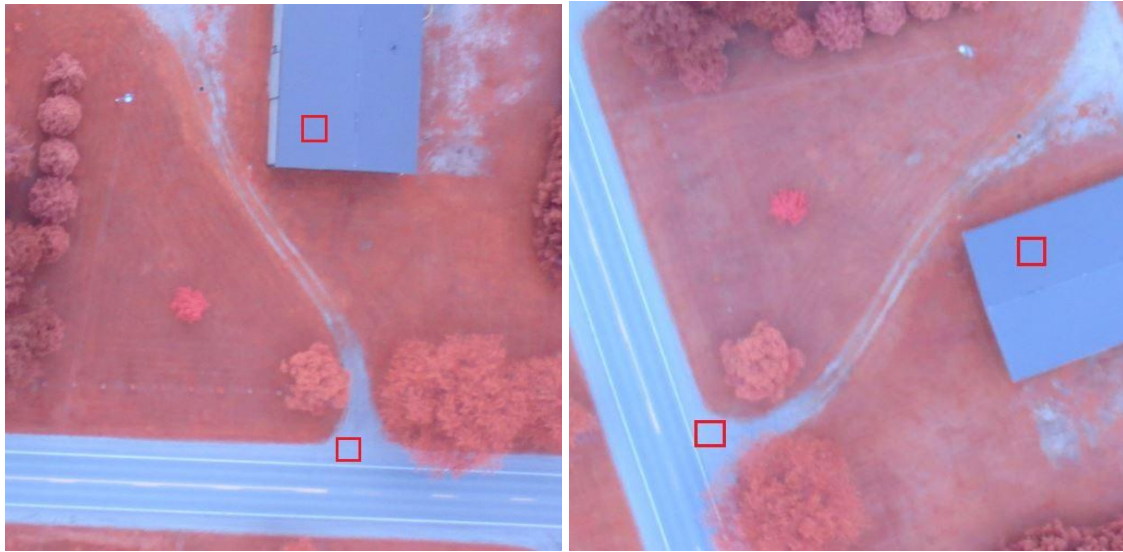
**Figure 3.4 The flowchart for data processing and models establishment. Left side is flowchart of yield prediction model; middle is general images processing; right side is flowchart of total nitrogen weight model.**

### 3.3 Results

#### 3.3.1 UAV-based imagery normalization and GNDVI calculation

The same camera may provide different DNs on the images for the same area at different time with the influence of different illumination. An image normalization process will convert all multi-temporal images to the same scale to represent at the same object. The optical satellite imagery will be converted to a reflectance value before the calculation of vegetation indices. For the UAV-based imagery, a ground reference will be needed to measure the reflectance value by the ASD in order to convert DNs to reflectance. In this study, the data provided by A&L Lab is missing the reflectance measurements. Therefore, an image normalization process was used to rescale all multi-temporal images at the same value to represent the same object. The road and the roof of a house in the field were used as reference targets to normalize the UAV-based imagers (Figure 3.5).





(c)

(d)

**Figure 3.5 Ground reference targets, roof and road (red boxes) selection in the UAV-based imagery. (a) image captured on May 21, (b) image captured on May 29, (c) images captured on June 19, (d) image captured on July 2.**

All images used data on June 19 as the reference value to normalize. After the image normalization, the GNDVI images were calculated for all multi-temporal UAV-based images. Figure 3.6 shows the GNDVI images on May 29 before and after images normalization. In the images, the range of GNDVI values had a minor change.

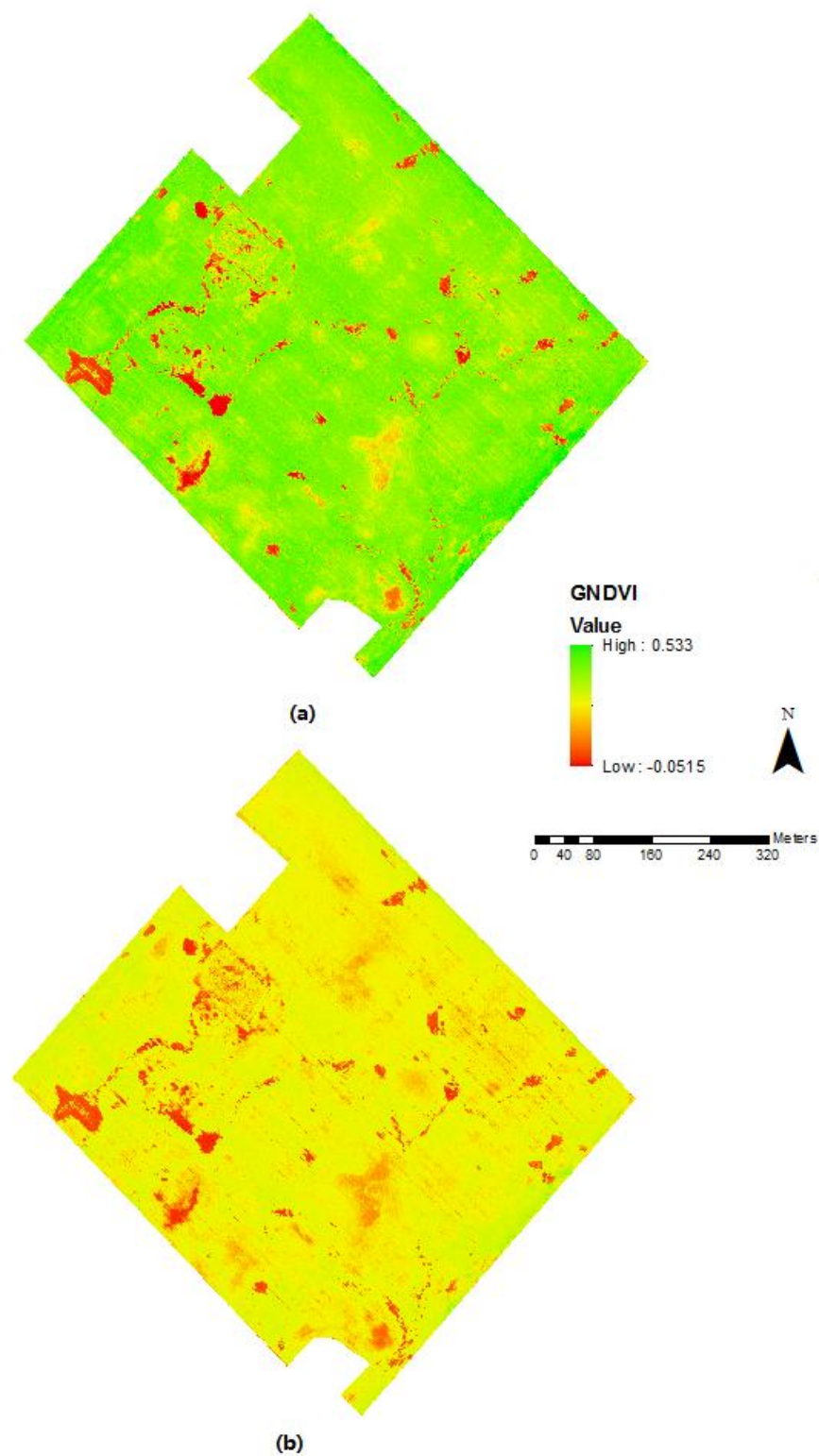


**Figure 3.6 GNDVI images before and after image normalization on May 29. (a) GNDVI image before normalization, (b) GNDVI image after normalization.**

### 3.3.2 Winter wheat biomass vs. plant height and fCover and PAI

A simple linear regression model was developed between reference dry biomass and plant height  $\times$  fCover that was evaluated by the coefficient of determination ( $R^2 = 0.9222$ ) (Figure 3.7). A simple linear regression model was also developed between measured dry biomass and plant height  $\times$  PAI that was evaluated by the coefficient of determination ( $R^2 = 0.8758$ ) (Figure 3.8).

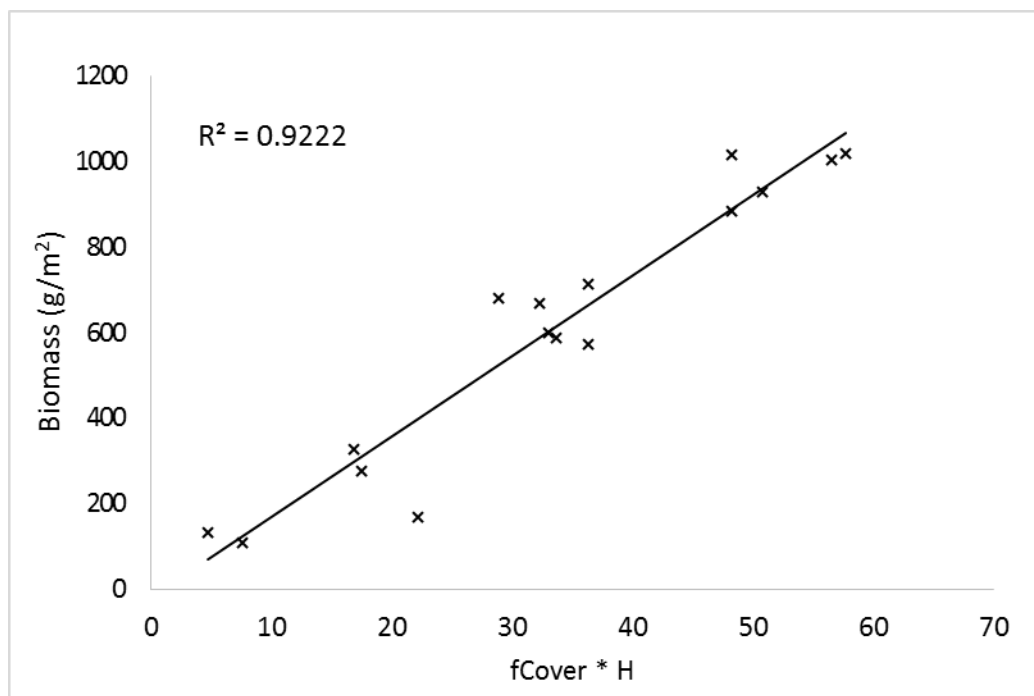


**Figure 3.7 Scatter plot for fCover and reference dry biomass for all samples in wheat collected during the entire season ( $n = 16$ ).  $R^2$  is the coefficient of determination.**

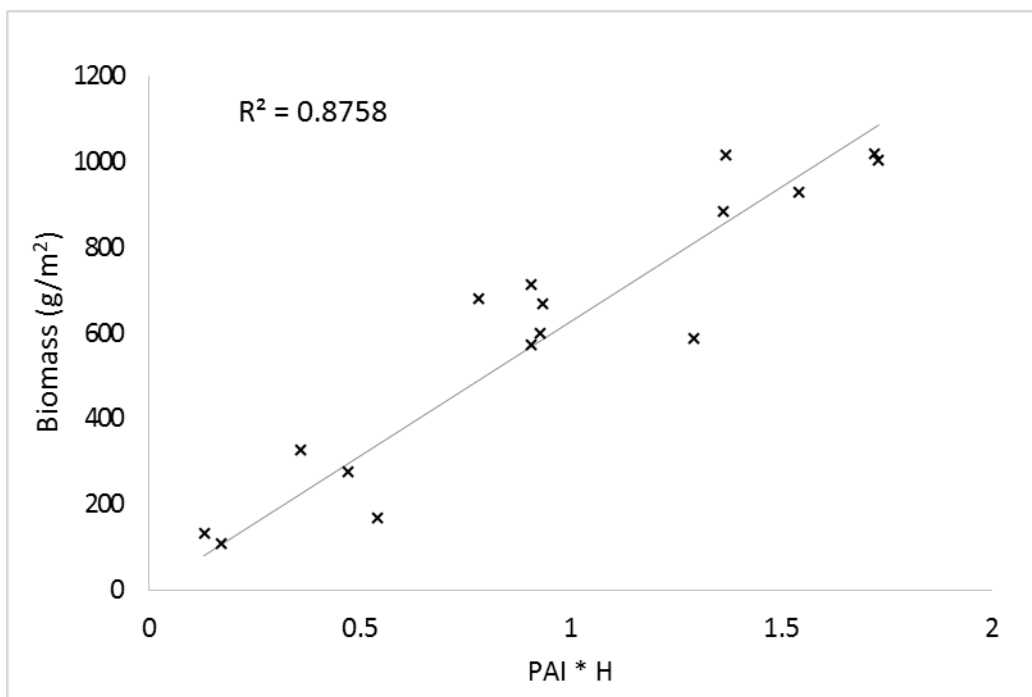


**Figure 3.8 Scatter plot for PAI and reference dry biomass for all samples in wheat collected during the entire season (n = 16).  $R^2$  is the coefficient of determination.**

As shown in these two figures, dry biomass was strongly correlated with plant height and plant leaf properties, i.e., fCover and PAI in winter wheat, respectively. Therefore, winter wheat plant dry biomass could be represented by the biomass calculated model which includes parameters of plant height, plant area index and fCover. In this study, the correlation between wheat plant cover fraction  $\times$  plant height and dry biomass resulted in a higher  $R^2$  value.

### 3.3.3 Relationship between winter wheat foliage nitrogen and GNDVI; total nitrogen weight and GNDVI

A simple regression model was used to evaluate the correlation between wheat foliage nitrogen and GNDVI; however, the relation is weak, with  $R^2 = 0.0361$ .

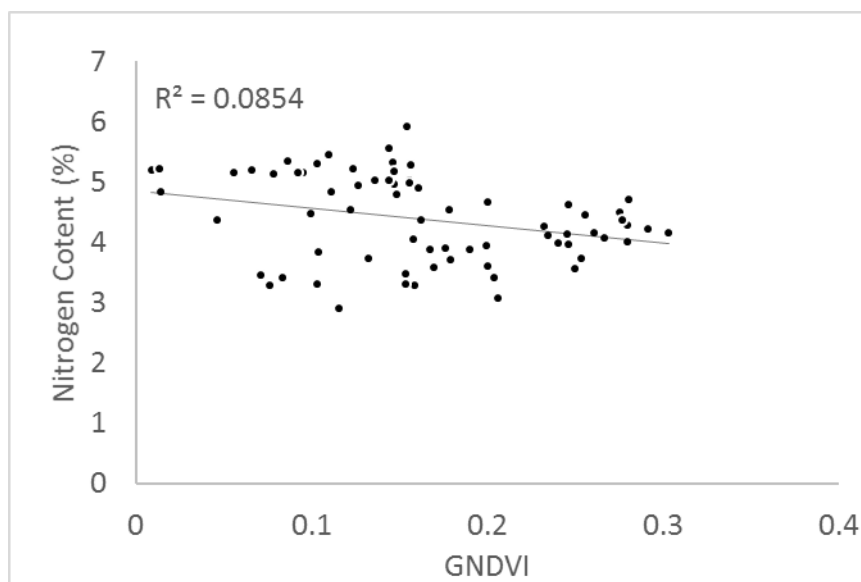


**Figure 3.9 Scatter plot for GNDVI and nitrogen content for all sample points in wheat (n = 113).**

Because of the poor correlation between wheat foliage nitrogen content and GNDVI, total foliage nitrogen content was difficult to determine from GNDVI directly. Hence, we multiplied estimated dry biomass by foliage nitrogen content to represent the estimated total nitrogen weight of wheat canopy per unit area. Then, as a first step, a simple regression model was used to analyze the relationship between GNDVI and estimated nitrogen content for all data from May to July. The  $R^2$  values for these models with fCover and PAI were 0.5396 and 0.5860, respectively.

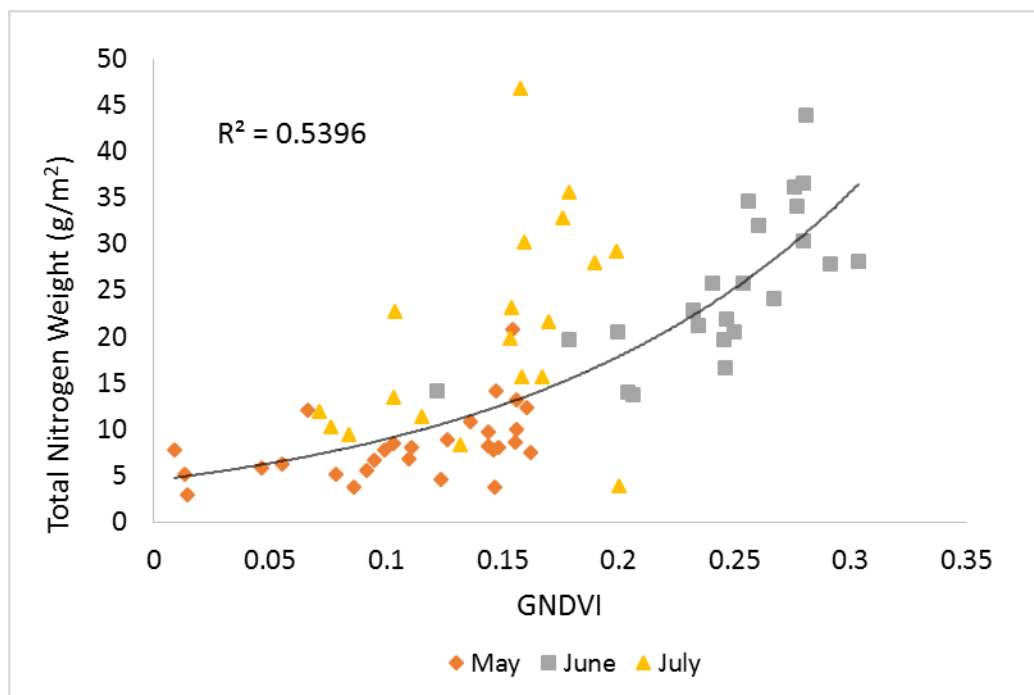


**Figure 3.10** Scatter plot for GNDVI and estimated nitrogen weight with fCover (n = 71).

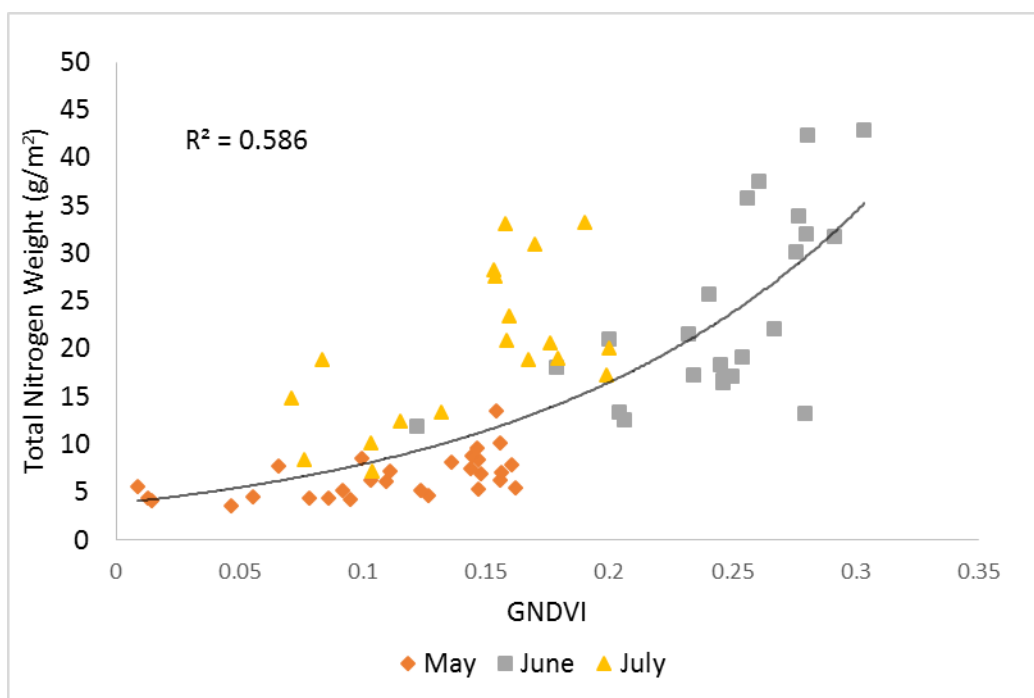


**Figure 3.11** Scatter plot for GNDVI and estimated nitrogen weight with PAI (n = 71).



We removed the data collected in July since it contributed the most outliers, and exponential regression models were applied to GNDVI and estimated nitrogen weight with fCover and PAI data in May and June only. These regression models were established with 41 points, and 11 of the points were used to estimate the accuracy of the model (Figure 3.12 and 3.13). The coefficient of determination ( $R^2$ ) for the fCover model and that for the PAI model was 0.7931 and 0.8229, with RMSEs of 5.54 g/m<sup>2</sup> and 3.79 g/m<sup>2</sup>, respectively.

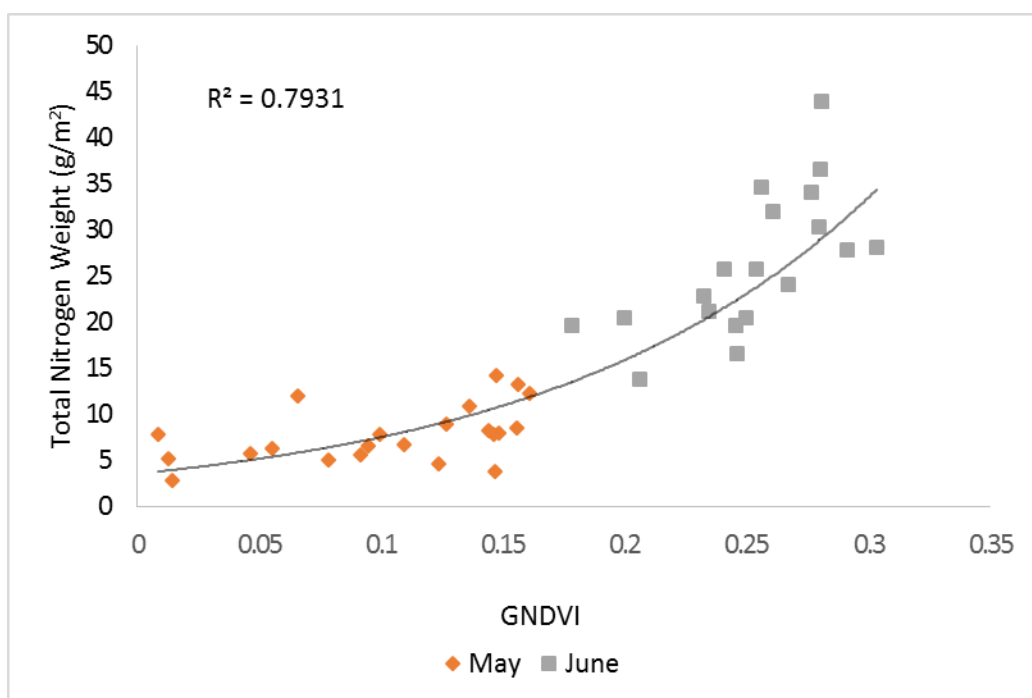


**Figure 3.12 Scatter plot for GNDVI and estimated nitrogen weight with fCover in wheat (n = 41).**

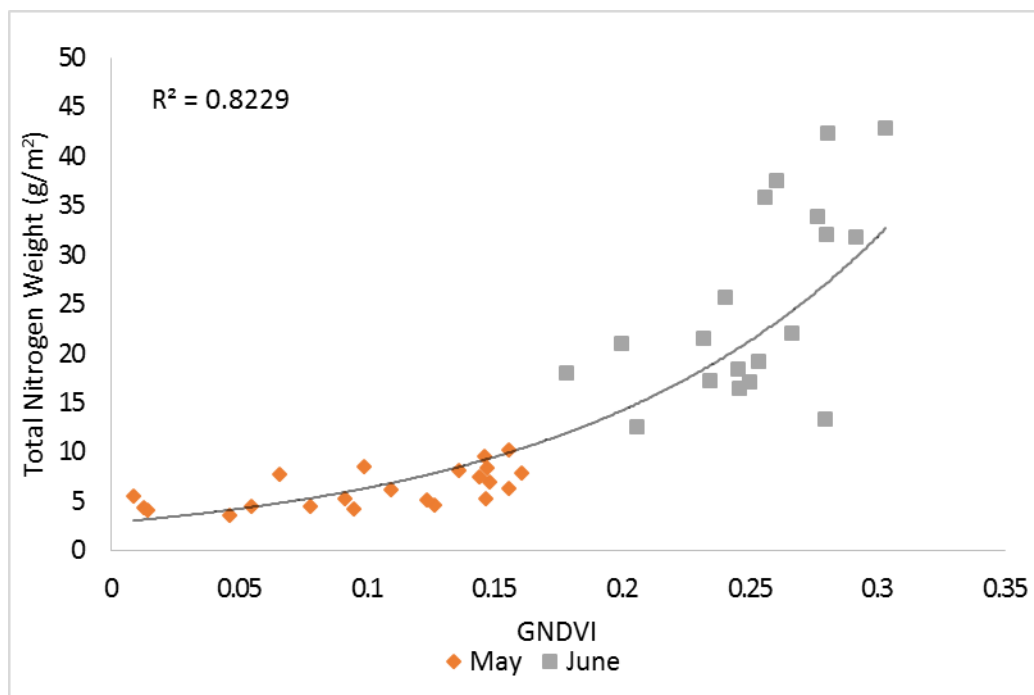


**Figure 3.13 Scatter plot for GNDVI and estimated nitrogen weight with PAI in wheat (n = 41).**

We applied the  $\text{PAI} \times \text{plant height}$  total nitrogen weight model in our test field using GNDVI to calculate the estimated nitrogen weight; this model was selected because of the higher coefficient of determination and lower RMSE. The map of total nitrogen weight for one of our test sites is shown in Figure 3.14. The range of total nitrogen weight was from  $1.55 \text{ g/m}^2$  to  $25.81 \text{ g/m}^2$ , with a corresponding color scale ranging from red (low) to green (high).

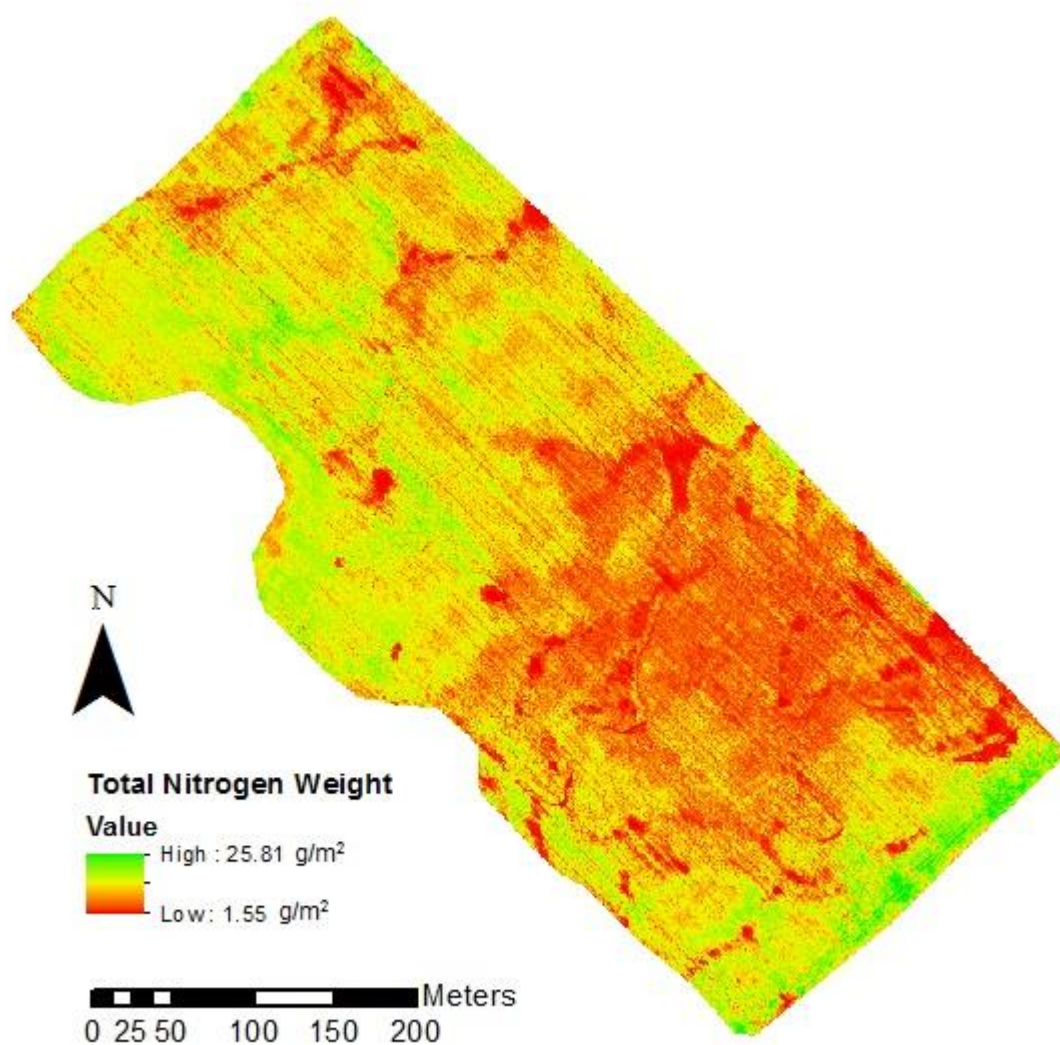


**Figure 3.14 Map of total nitrogen weight for test field one.**

### 3.3.4 Estimation of winter wheat final yield using temporal GNDVI

An exponential regression was used to determine the relationships between GNDVI and estimated  $\text{biomass}_{f\text{Cover}}$  and  $\text{biomass}_{\text{PAI}}$ . The coefficient value of  $R^2$  was 0.8049 and 0.8302 for the  $f\text{Cover}$  model and the PAI model, respectively (Figures 3.15 & 3.16).

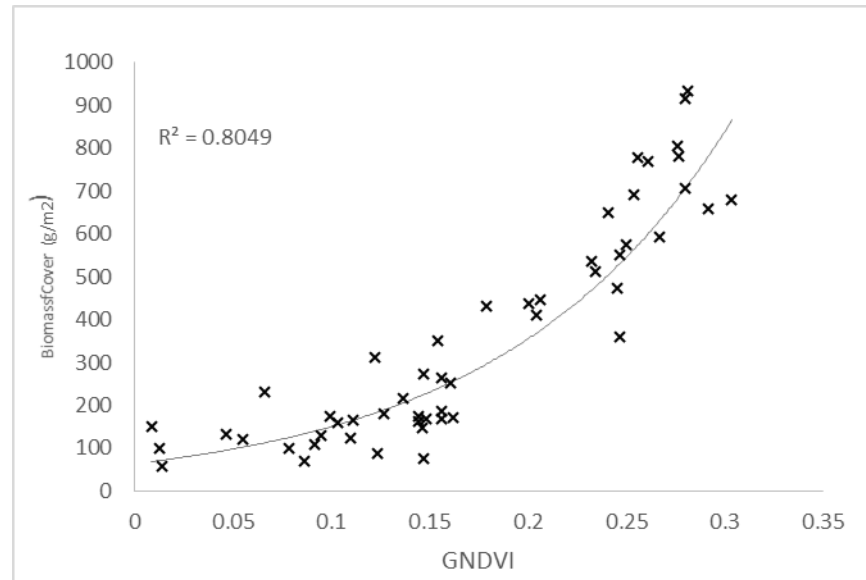


**Figure 3.15 Scatter plot for GNDVI and estimated biomass<sub>fCover</sub>.**

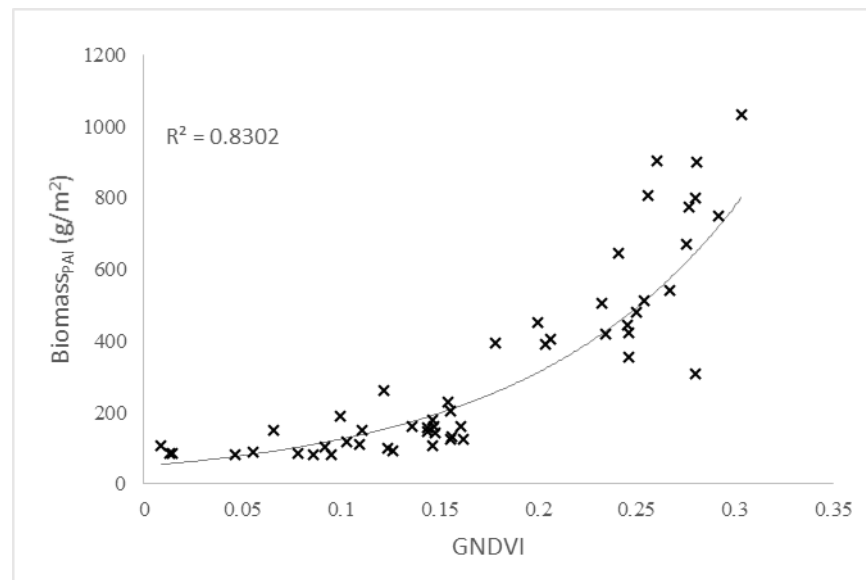


**Figure 3.16 Scatter plot for GNDVI and estimated biomass<sub>PAI</sub>.**

In this study, 466 samples were selected, which were separated into two groups. The first group contained 350 sample points that were used to build the models, and the second group contained 116 samples that were used for verification. A comparison between different combinations of single and multi-temporal biomass data were carried out in this study to determine the best combination of multi-temporal data in yield prediction. The

combinations are shown in the table below, including the coefficient of determination for each model.

**Table 3.2 Data combinations and results using linear regression**

	21-May	29-May	19-Jun	R <sup>2</sup>
<b>Combination</b>				0.35
				0.76
				0.65
				0.79
				0.68
				0.78
				0.81

According to the results in Table 3.2, the best R<sup>2</sup> result comes from the combination of May 21, May 29, and June 19. The combinations of date May 21 and May 29, May 29 and June 19 have very similar R<sup>2</sup> results, 0.78 and 0.79 respectively. Multiple linear regression was applied to three date estimated biomass, which was derived from the fCover model, and final yield data; the correlation value R was 0.8972 (Figure 3.17). The RMSE for our yield model was 11.8 bushels/acre, which was significant at  $p < 0.0001$ . Multiple linear regression was also applied to determine the relationship between estimated multi-temporal biomass results, which was derived from the PAI, and final yield data; the correlation of R was 0.8971, the RMSE was 11.85 bushels/acre, and  $p < 0.0001$  (Figure 3.19). Because some bare area with no wheat coverage in the wheat field produced outliers in these models, data for bare area were removed, and the correlation between reference yield and predicted yield improved to 0.9040 and 0.9039, and the RMSE improved to 11.5 bushels/acre and 11.53 bushels/acre, respectively (Figures 3.18 & 3.20). By using the improved models, maps of predicted yield were generated based on the multiple linear regression models (Figure 3.21).

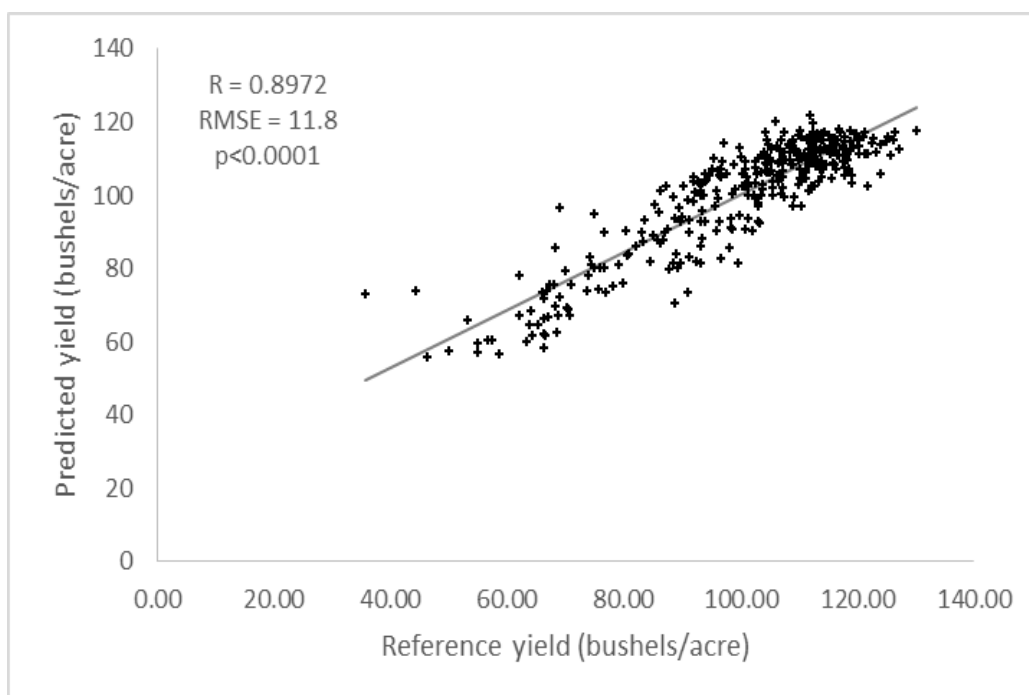


**Figure 3.17** Scatter plot for predicted yield and reference yield map using the fraction vegetation cover model.

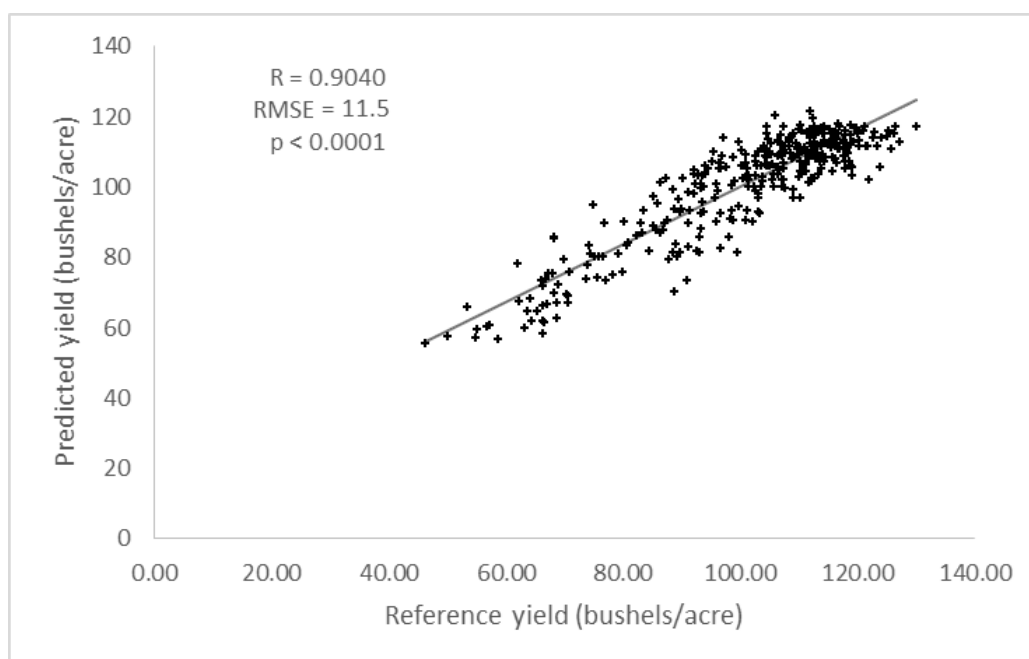


**Figure 3.18** Scatter plot for predicted yield and reference yield map using the fraction vegetation cover model, with bare area removed.

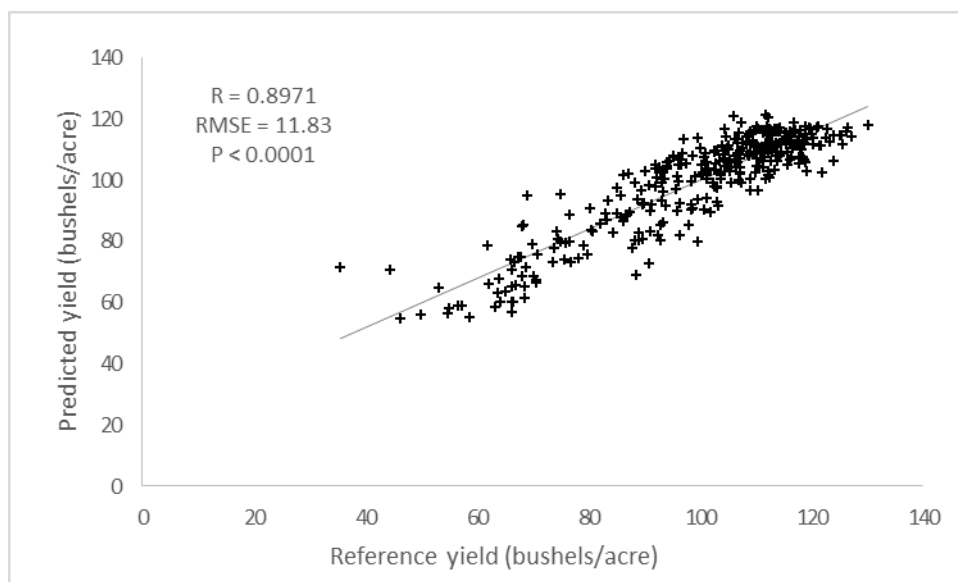


**Figure 3.19 Scatter plot for predicted yield and reference yield using the PAI model.**

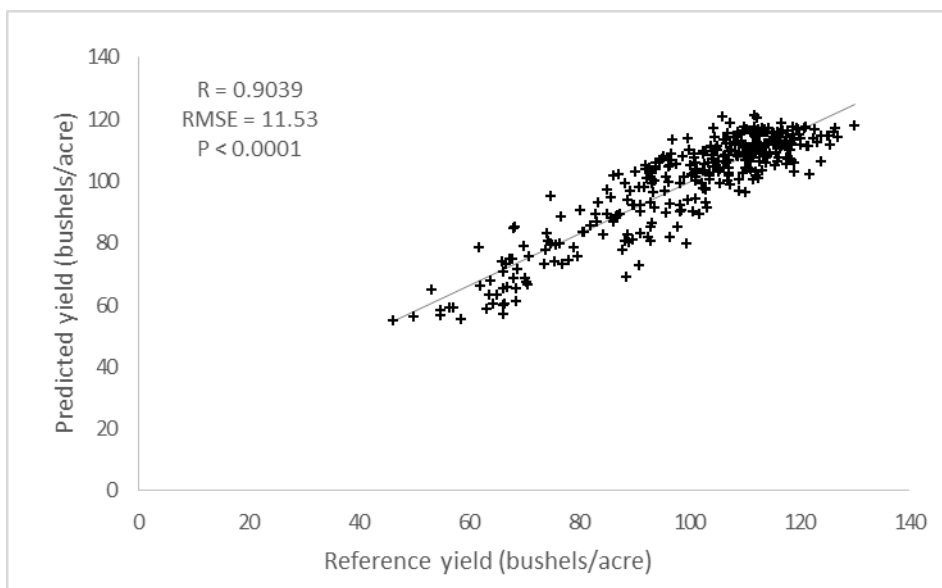


**Figure 3.20 Scatter plot for predicted yield and reference yield map using the PAI model, with bare area removed.**

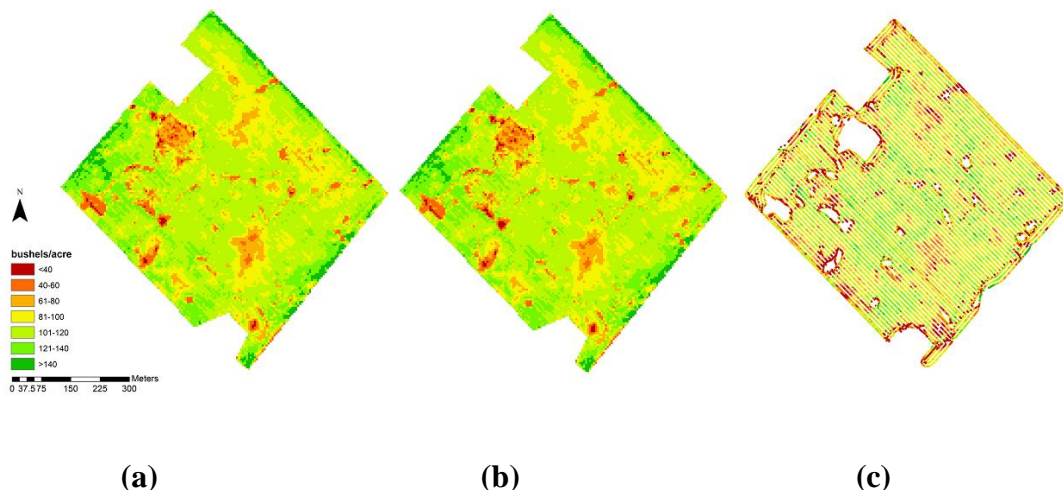


**Figure 3.21 Map of predicted yield and true spatial yield (bushels/acre), (a) fCover model, (b) PAI model, (c) True spatial yield. The blank part in (c) were bare area in the wheat field for which the harvester had no measurements.**

## 3.4 Discussion

### 3.4.1 Relationship between Nitrogen content and GNDVI

In the first part of this study, we determined the relationship between wheat foliage nitrogen and the remote sensing results GNDVI. The GNDVI was correlated weakly with the reference wheat foliage nitrogen content measurements ( $R^2 = 0.085$ ). Wheat foliage nitrogen content ranged from 3% to 6%, with a trend for nitrogen content to decrease from May to July, possibly caused by mechanisms of nitrogen distribution and transformation in wheat. In the tillering and stem extension stage, wheat absorbed much nitrogen from soil to produce chlorophyll, and therefore, the two measurements in May were the highest for nitrogen content. From stem extension to the heading stage, the transfer of nitrogen in leaves to grain was initiated, and the foliage nitrogen content rapidly declined. Therefore, we calculated the total weight of foliage nitrogen using a physical dry biomass estimation method to evaluate the relationship between total weight of foliage nitrogen and GNDVI.



### 3.4.2 Nitrogen weight model with May and June data

According to the relationship between reference biomass and fCover or PAI, the estimated  $\text{biomass}_{\text{fCover}}$  or  $\text{biomass}_{\text{PAI}}$  multiplied by the nitrogen content per unit area represented the total nitrogen weight per unit area. Exponential regressions were used to evaluate the relations between estimated  $\text{biomass}_{\text{fCover}}$  and  $\text{biomass}_{\text{PAI}}$  and total nitrogen weight, with coefficient values of  $R^2$  of 0.585 and 0.5385, respectively. As shown in Figures 3.10 and 3.11, most outliers were found in the data collected in July. Therefore, we used the data from May and June to establish the total weight nitrogen models. The coefficient values of  $R^2$  between GNDVI and total nitrogen weight per unit area increased significantly for both models.

From May to June, wheat growth stage was at BBCH 40 to 69, which is the primary period for wheat structural change as the wheat awns develops and stems elongate (White, 2007). In May, wheat growth extended from late tillering to stem extension stages. In June, wheat growth passed from the stem extension stage to the heading stage. As a result, from May to June, the fCover, PAI and plant height increased significantly; therefore, total nitrogen weight models were sensitive to data from May and June. In July, wheat growth passed from the heading stage to the ripening stage, with wheat grains generated and formed in this period, and the nitrogen content decreased as the nitrogen in foliage transferred to grain. Values of GNDVI from UAV-based images decreased when wheat leaves turned yellow from green in July, although little change occurred in plant structure and height in July. Therefore, these nitrogen weight models were more strongly correlated with GNDVI in May and June. In Figure 3.22(d), for example, although the wheat had started to turn yellow, the height was (c) identical to that in June. Because of the high correlation between GNDVI and total nitrogen weight in May and June, these nitrogen weight predicted models can be used for early and mid-season wheat nitrogen monitoring and mapping for farmers on decision making and variable fertilizer application.

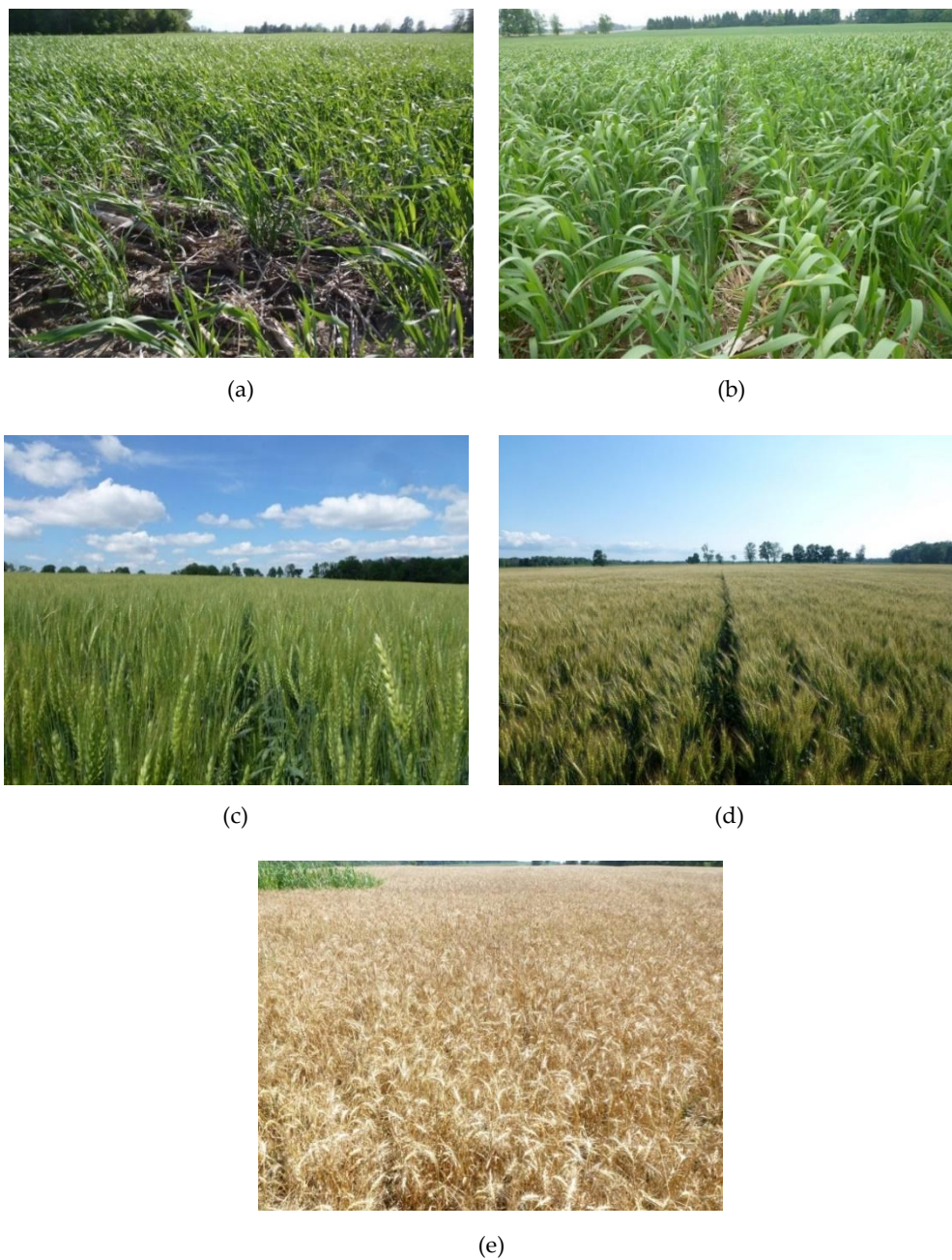


**Figure 3.22 Photographs of wheat fields at different BBCH. (a) May 21 at BBCH 42; (b) May 29 at BBCH 48; (c) June 19 at BBCH 65; (d) July 2 at BBCH 79; (e) July 27 at BBCH 99.**

### 3.4.3 PAI vs. fCover for biomass estimation

Because fCover and PAI represented plant structure and leaf density, the comparison between biomass estimation models derived from fCover and PAI was given in this study. These two models all had similar values for the coefficient of determination. When we used plant height multiplied by fCover and PAI to calculate the estimated biomass<sub>fcover</sub> and biomass<sub>PAI</sub> of wheat plants, the coefficient value of  $R^2$  was 0.9222 and 0.8758 for fCover  $\times$  plant height and for PAI  $\times$  plant height, respectively. Both parameters were strongly correlated with wheat dry ground reference biomass. However, in the both prediction models for total nitrogen weight and final yield, the coefficient of determination was lower in the models with fCover than in those with PAI. This difference might be caused by a basic difference between the calculation principles of fCover and PAI. The fCover is the planer projection of all plant leaves and stems and is a measure of the fraction of ground covered by green vegetation, whereas PAI is the total area of leaves and stem in a spatial area that is calculated based on one side of green leaf area per unit ground area. Additionally, PAI provides a three-dimensional distribution of plant leaves, with plant height included as a factor in the calculation. Therefore, when we compared the correlations between reference biomass and fCover  $\times$  plant height and reference biomass and PAI  $\times$  plant height in linear regression models, the coefficient of determination was higher in PAI model than that in fCover model. We used exponential regression to establish the model for wheat total nitrogen weight, with the PAI model providing a higher coefficient of determination because plant height was considered twice. As a reasonable model, the total nitrogen weight model with fCover should be used in practice. In the wheat yield prediction models, both fCover and PAI were used to predict the biomass on May 21, May 29 and June 27. With multiple linear regression models, the trend of biomass change was used to predict the final yield. The effect of overestimated biomass from using fCover was insignificant in the model. The predicted yield provided from yield prediction models with fCover and PAI both had similar correlation values, 0.9040 and 0.9039, respectively to the reference yield.

### 3.4.4 Discussion of estimated yield data

A relationship between GNDVI and estimated biomass which was calculated based on the plant structural properties  $\times$  plant height was evaluated in this study. From Figures 3.15 and 3.16, GNDVI was strongly correlated with estimated biomass in winter wheat, with coefficient values of 0.8049 and 0.8302 for estimated biomass<sub>fCover</sub> and biomass<sub>SPAI</sub>, respectively. Therefore, we used multi-temporal estimated biomass values derived from GNDVI to build a multiple linear regression model to predict the final winter wheat yield. A total 466 sample points were selected from the four random areas in four wheat fields, with 350 points used to establish the model and the other 116 points used to validate our model. In order to select the best dataset to apply in multiple linear regression model, seven combinations of dataset were applied in linear regression model. The correlation between predicted biomass on May 29 and reference yield is higher than those data on May 21, and June 19. Additionally, for all predicted biomass combinations that contain data on May 29, the correlation between predicted multi-temporal biomass and reference yield is higher than that without data on May 29. These results showed that the data on May 29 strongly influence the accuracy in the yield estimation model. At this period, the wheat growth stage is at BBCH 48 which is after the flag leaf sheath opens and before the first awns are visible. With the fully developed wheat canopy, the GNDVI results had a better performance on wheat status monitoring without the interference from soil background and wheat yellow awns. This is the prime time for winter wheat monitoring in order to predict the final yield.

The multiple linear regression model built with data from May 21 and 29 and June 19 had a correlation of  $R = 0.8972$ . However, GNDVI on July 2 was a poor representation of wheat plant structure because wheat leaves started to turn yellow and wheat heading on the top of the canopy covered most leaves; therefore, the multiple linear regression model used data for May and June only. Additionally, some bare areas without plants occurred in wheat fields in May. In June and July, these spots were covered by alfalfa, which provided a high GNDVI in images from June and July. For example, in Figure 3.22(e), green alfalfa is visible in the left top of this image, whereas the wheat had matured completely. In Figures 3.17 & 3.19, the scatter plots of predicted yield vs. reference yield

are shown with models built by data from May 21 and 29 and June 19. Some outliers occurred with low reference yields of approximately 30 bushels/acre and predicted yields of 70 bushels/acre. These outliers were caused by bare areas in wheat fields, which changed the GNDVI irregularly during the growth of wheat plants. In May, no plants were in these spots, and the GNDVI value was as low as the soil, whereas in June, these spots began to be covered by other vegetation such as alfalfa, with high GNDVI values. Figure 3.23 shows the wheat empty spots (blue circles) were covered by alfalfa on June 19. Therefore, we removed the sample points from these empty spots and rebuilt our model; the coefficient value of R increased to 0.9040, the RMSE was 11.5 bushels/acre, and  $p < 0.0001$ .

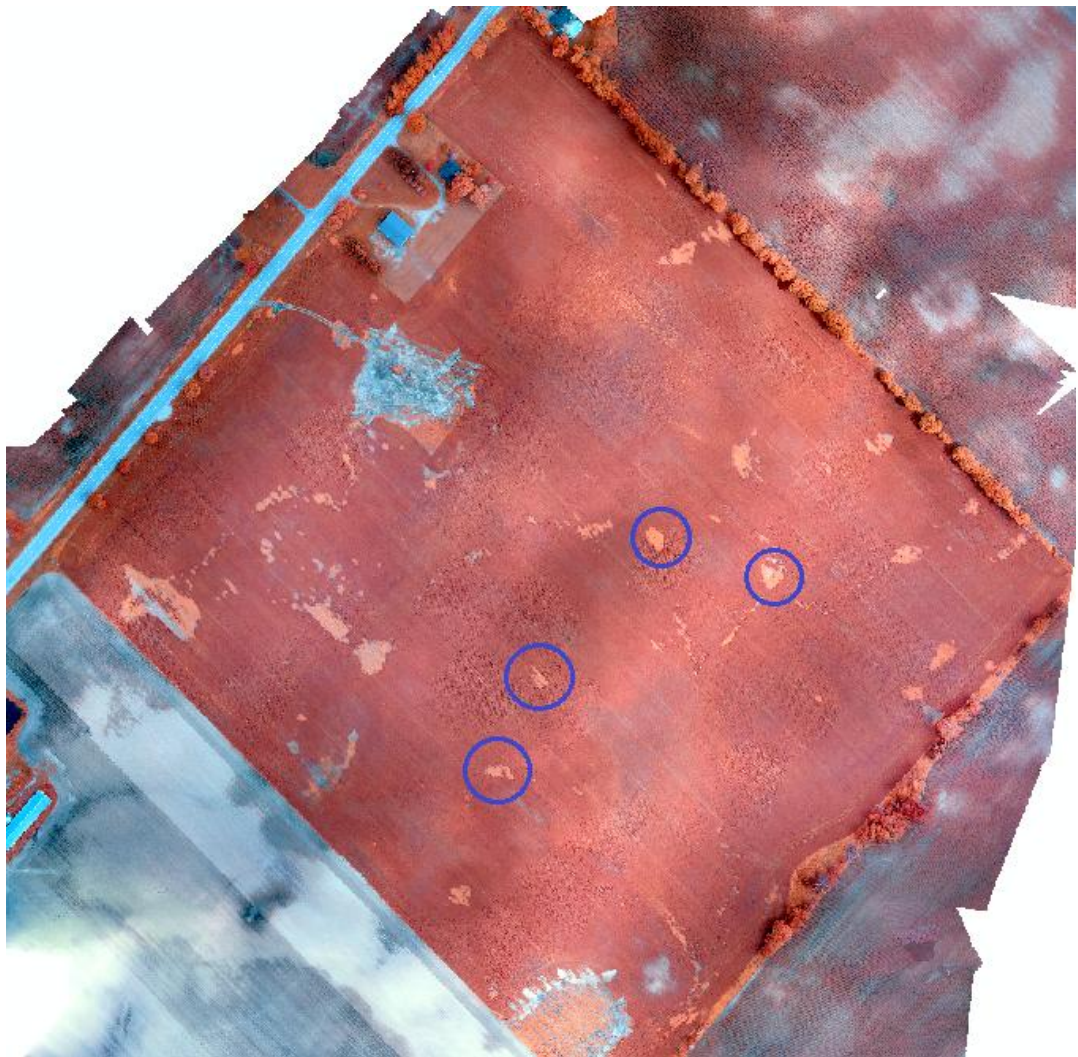


**Figure 3.23 Bare areas in wheat field.**



### 3.5 Conclusions

The UAV-based remote sensing information of GNDVI was used to predict the wheat nitrogen weight ( $\text{g/m}^2$ ) and final yield in this study. Both methods provides a predicted mapping for intra-field nitrogen and predicted yield spatial distribution. Both fCover and PAI were used to establish the nitrogen and yield prediction models and assess which nitrogen prediction models had better performance for wheat early growth stages at BBCH 40-69 between tillering to heading stages. With the GNDVI values derived from the multi-temporal UAV-based remotely sensed images and the measurements of the ground reference included PAI, fCover, plant height, and foliage nitrogen content, the best yield prediction time was indicated in this study.

We used the relationship between biomass and plant structure  $\times$  plant height to introduce a simple method for estimating total nitrogen weight in wheat leaves and a combined multi-temporal dataset method for predicting wheat final yield based on GNDVI values derived from UAV-based blue-green-NIR optical images. We first determined the relationship between GNDVI and ground total nitrogen weight per unit area from May to June. Based on the coefficient of determination ( $R^2 = 0.7742$ ), GNDVI could be used to monitor and predict total nitrogen status in early and mid-season wheat, BBCH 40-69. This period, which is important for wheat growth and final grain production, affected the final biomass and yield production. Within field mapping of nitrogen was generated in this study, these results could help farmers in quantitative spatially variable fertilizer application. Instead of laboratory plant analysis, the UAV-based imagery method provides a real-time and entire field nitrogen prediction. Second, the yield prediction model was developed based on the strong correlation between GNDVI and biomass. A multiple linear regression model was applied using temporal series GNDVI data to build a wheat yield prediction model and generate a yield spatial distribution map. The best yield prediction time for winter wheat was determined to be wheat BBCH stage 48 before awns appear. This results provides almost a two month early winter wheat prediction for farmers, this could effectively help farmers to make better decision on wheat management.

UAV-based remote sensing can provide more temporal images for a crop field than traditional satellite images. Additionally, UAVs provide very high-resolution images for a study area. In this study, the resolution of UAV images was 0.50 m per pixel, which was sufficient to identify bare areas in wheat fields. By contrast, with traditional satellite images, obtaining a sufficient level of detail in a small-scale field is difficult. The combination of high-resolution UAV-based blue-green-NIR images and high-resolution spatial yield data provided many sample points. The yield prediction model that was established with these many sample points provided reliable predictions. In this study, we selected 460 total points to build and test our model.

Improvements are required for multispectral image collection using UAV systems and also for the frequency of image capture. A multispectral camera could collect more information at different wavelengths. The UAV imagery in this study was conducted by image normalization process to rescale all image; the future research could analyzed by using reflectance values to study the nitrogen variation in different years. Additionally, the method in this study could include more vegetation indices in the monitoring of other crops. As demonstrated in this study, a collection of high-frequency, UAV-based images could help determine the best period to monitor crops for nitrogen and yield predictions. With consideration of farmer concern about plant health status within their farms, this model could help farmers easily achieve within field nitrogen monitoring and final yield prediction. Furthermore, as demonstrated in this study, UAV-based images can provide intra-field crop yield prediction with its high spatial and temporal imagery. Further tests on yield prediction should include environmental factors, such as rainfall, temperature and solar radiation, because this information could improve the model to determine yearly variation in yields.

### 3.6 References:

- Adam K. Tilling Jelle G. Ferwerda, Simon D. Jones, Glenn J. Fitzgerald, Daniel Rodriguez, Robert Belford, G. J. O. (2007). Remote sensing of nitrogen and water stress in wheat. *Field Crops Research*, 104, 77–85.
- Baez-gonzalez, A. D., Chen, P., Tischarena-lopez, M., & Srini, R. (2002). Using satellite and field data with crop growth modeling to monitor and estim ..., 1949, 1943–1949.
- Barnes, E., Clarke, T., Richards, S., Colaizzi, P. D., Haberland, J., Kostrzewski, M., ... Moran, M. S. (2000). Coincident detection of crop water stress, nitrogen status and canopy density using ground-based multispectral data. *Proceedings of the Fifth International Conference on Precision Agriculture*. Retrieved from [http://www.cprl.ars.usda.gov/wmru/pdfs/Barnes-coincident detection.pdf](http://www.cprl.ars.usda.gov/wmru/pdfs/Barnes-coincident%20detection.pdf)
- Caturegli, L., Casucci, M., Lulli, F., et al..(2015). GeoEye-1 satellite versus ground-based multispectral data for estimating nitrogen status of turfgrasses. *International Journal of Remote Sensing*, 36(8), 2238–2251.  
<http://doi.org/10.1080/01431161.2015.1035409>
- Chen, P., Haboudane, D., Tremblay, N., Wang, J., Vigneault, P., & Li, B. (2010). New spectral indicator assessing the efficiency of crop nitrogen treatment in corn and wheat. *Remote Sensing of Environment*, 114(9), 1987–1997.  
<http://doi.org/10.1016/j.rse.2010.04.006>
- D.G. Sullivan P.L. Mask, D. Rickman, J. Luvall and J.M. Wersinger, J. N. S. (2004). Evaluating corn nitrogen variability via remote-sensed data. *Communications in Soil Science and Plant Analysis*, 35, 2465–2483.
- Doraiswamy, P. C., Moulin, S., Cook, P. W., & Stern, A. (2003). Crop Yield assessment from remote sensing. *Photogrammetric Engineering and Remote Sensing*, 69, 665–674. <http://doi.org/10.14358/PERS.69.6.665>



- Hunt, E. R. JR., Cavigelli, M., Daughtry, C. S.T., McMurtrey J. III, and Walthall C. L.(2005). Evaluation of digital photography from model aircraft for remote sensing of crop biomass and nitrogen status. *Precision Agriculture*, 6, 359–378.
- Erickson, J. D. (1984). *The LACIE Experiment in Satellite Aided Monitoring of Global Crop Production*. Scope
- Fageria, N. K. (2014). *Nitrogen Management in Crop Production*.CRC Press
- Fang, H., Liang, S., & Hoogenboom, G. (2011). Integration of MODIS LAI and vegetation index products with the CSM–CERES–Maize model for corn yield estimation. *International Journal of Remote Sensing*, 32(4), 1039–1065.  
<http://doi.org/10.1080/01431160903505310>
- Gitelson, a, & Merzlyak, M. N. (1994). Spectral reflectance changes associated with autumn senescence of aesculus-hippocastanum L. and acer-platanoides L. leaves - spectral features and relation to chlorophyll estimation. *Journal of Plant Physiology*, 143(3), 286–292. [http://doi.org/10.1016/S0176-1617\(11\)81633-0](http://doi.org/10.1016/S0176-1617(11)81633-0)
- Hamar, D., Ferencz, C., Lichtenberger, J., Tarcsai, G., & Ferencz-Arkos, I. (1996). Yield estimation for corn and wheat in the Hungarian Great Plain using Landsat MSS data. *International Journal of Remote Sensing*, 17(9), 1689–1699.  
<http://doi.org/10.1080/01431169608948732>
- Hansen, P. M., & Schjoerring, J. K. (2003). Reflectance measurement of canopy biomass and nitrogen status in wheat crops using normalized difference vegetation indices and partial least squares regression. *Remote Sensing of Environment*, 86(4), 542–553. [http://doi.org/10.1016/S0034-4257\(03\)00131-7](http://doi.org/10.1016/S0034-4257(03)00131-7)
- Huang, J., Tang, S., Ousama, A.-I., & Wang, R. (2002). Rice yield estimation using remote sensing and simulation model. *Journal of Zhejiang University SCIENCE*, 3(4), 461–466. <http://doi.org/10.1631/jzus.2002.0461>
- J.G.P.W. Clevers; A.A. Gitelson. (2012). Remote estimation of crop and grass chlorophyll and nitrogen content using red-edge bands on Sentinel-2 and -3.

- International Journal of Applied Earth Observation and Geoinformation*, 23, 344–351.
- J.G.P.W Clevers (1997). A simplified approach for yield prediction of sugar beet based on optical remote sensing data. *Remote Sensing of Environment*, 61(2), 221–228. [http://doi.org/10.1016/S0034-4257\(97\)00004-7](http://doi.org/10.1016/S0034-4257(97)00004-7)
- Johnson, D. M. (2014). An assessment of pre- and within-season remotely sensed variables for forecasting corn and soybean yields in the United States. *Remote Sensing of Environment*, 141, 116–128. <http://doi.org/10.1016/j.rse.2013.10.027>
- Krebs, C. J., Danell, K., Angerbjörn, A., Agrell, J., Berteaux, D., Bråthen, K. A., ... Wiklund, C. (2003). Terrestrial trophic dynamics in the Canadian Arctic. *Canadian Journal of Zoology*, 81(5), 827–843. <http://doi.org/10.1139/z03-061>
- Krishna, K. R. (2013). *Precision farming: Soil fertility and productivity aspects*, CRC Press.
- Lelong, C. C. D., Burger, P., Jubelin, G., Roux, B., Labbé, S., & Baret, F. (2008). Assessment of unmanned aerial vehicles imagery for quantitative monitoring of wheat crop in small plots. *Sensors*, 8(5), 3557–3585. <http://doi.org/10.3390/s8053557>
- Merzlyak, A. A. G. and M. N. (1998). Remote sensing of chlorophyll concentration in higher plant leaves. *Adv. Space Res.*, 22(5), 689–692.
- Muukkonen, P., Mäkipää, R., Laiho, R., Minkkinen, K., Vasander, H., & Finér, L. (2006). Relationship between biomass and percentage cover in understorey vegetation of boreal coniferous forests. *Silva Fennica*, 40(2), 231–245.
- Noyd, R.K., Krueger, J.A., Hill, K.M., (2016). Biology: Organisms and adaptations, media update, enhanced edition. *Brooks cole*, 417.
- Prasad, A. K., Chai, L., Singh, R. P., & Kafatos, M. (2006). Crop yield estimation model for Iowa using remote sensing and surface parameters. *International Journal of*

- Applied Earth Observation and Geoinformation*, 8(1), 26–33.  
<http://doi.org/10.1016/j.jag.2005.06.002>
- Rodriguez, D., Fitzgerald, G. J., Belford, R., & Christensen, L. K. (2006). Detection of nitrogen deficiency in wheat from spectral reflectance indices and basic crop eco-physiological concepts. *Australian Journal of Agricultural Research*, 57(7), 781–789. <http://doi.org/10.1071/AR05361>
- Rojas, O. (2007). Operational maize yield model development and validation based on remote sensing and agro-meteorological data in Kenya. *International Journal of Remote Sensing*, 28(17), 3775–3793. <http://doi.org/10.1080/01431160601075608>
- Rottgermann, M., Steinlein, T., Beyschlag, W., & Dietz, H. (2000). Linear relationships between aboveground biomass and plant cover in low open herbaceous vegetation. *Journal of Vegetation Science*, 11(1), 145–148. <http://doi.org/10.2307/3236786>
- Sims, D. A., & Gamon, J. A. (2002). Relationships between leaf pigment content and spectral reflectance across a wide range of species, leaf structures and developmental stages 2002.pdf. *Remote Sensing of Environment*, 81, 337–354.
- Swain, K. C., Thomson, S. J., & Jayasurya, H. P. W. (2010). Adoption of an unmanned helicopter for low-altitude remote sensing to estimate yield and total biomass of a rice crop. *Transactions of the ASABE*, 53(1), 21–27. Retrieved from <http://ddr.nal.usda.gov/handle/10113/41029>
- Wenjun, C., Junhua, L., Zhang, Y., et al.. (2009). Relating biomass and leaf area index to non-destructive measurements in order to monitor changes in Arctic vegetation. *Arctic*, 62(3), 281–294.
- White, J. & J. E. (2007). *Wheat Growth & Development*. NSW Department of Primary Industries. Retrieved from <http://rub.ruc.dk/soeg/kviksoeg/?query=9781403996015>

## 4 Conclusions

### 4.1 Summary

Remote sensing information is one of the important components in precision farming which provides an efficient and effective tool for crop monitoring. The precise and real-time crop nitrogen monitoring and yield prediction during the crop growth season help farmers to make better decisions and estimate profit in agricultural activities. This real-time information greatly depends on continuous remotely sensed crop monitoring.

The commonly available optical remote sensing data is not reliable to provide high quality temporal imagery during the entire crop growth season due to frequent cloud cover and rainy weather in Ontario. In addition, the spatial resolution of imagery restricts the application of optical remote sensing data in intra-field crop monitoring. The UAV-based imagery provides an alternative high spatial and temporal data source for crop monitoring with a greater detection capability compared with the traditional optical satellite for intra-field variations.

Chapter 2 presented a comparison in detection capability and sensitivities to LAI and biomass estimations between the UAV-based multispectral imagery and the RapidEye imagery for corn in eastern Ontario. The comparison including detection in spatial variations, sensitivity in various fertilizer treatment, and six vegetation indices in LAI and biomass estimation demonstrated that the UAV-based multispectral images had a great potential in intra-field variability detection and seasonal crop growth monitoring.

Chapter 3 developed models to estimate total nitrogen weight and final yield using UAV-based blue-green-NIR imagery in winter wheat in Southwestern Ontario. A biomass estimation method was used to establish the models of total nitrogen weight and final yield prediction in order to provide farmers nitrogen weight and prediction yield maps and help in nitrogen management in future farm activities.

## 4.2 Conclusion and results

The research presented in this thesis provided responses according to the research objectives in Chapter 1.

1. The UAV derived NDVI had a greater range of NDVI values and higher CV values when compared with RapidEye NDVI value to represent spatial variations in corn field. The UAV imagery had a better performance in capturing the crop status variation of the two nitrogen treatment zones than that of RapidEye. The UAV provided more details and information to identify the region of interest on real-time monitoring in corn field.
2. NDVI<sub>re</sub> and SR<sub>re</sub> derived from the UAV imagery showed a high sensitivity to LAI from emergence to LAI up to 5 m<sup>2</sup>/m<sup>2</sup>. The cumulative SR derived from the UAV imagery showed no saturation for the entire biomass measurement. The remote sensing products of LAI and biomass revealed that the UAV-based multispectral imagery had a greater sensitivity to crop biophysical variables.
3. The total nitrogen weight model derived from a calculated biomass model had a good performance for early growth stage of wheat at BBCH 40-69 which is after wheat rooting stage and before fruit development stage.
4. The final yield model was established based on early multi-temporal estimated biomass. The map of predicted yield was provided by this yield prediction model and the best yield prediction time was indicated when wheat growth stage is BBCH 48.

## 4.3 Research contributions

The main contributions of the research in chapter 2 are demonstrated in three aspects:

1. An operational procedure of reflectance conversion method had been provided for UAV-based multispectral image processing. Using this procedure, the reflectance was calculated based on two reference targets and some natural reference targets.
2. Two red-edge vegetation indices, NDVI<sub>re</sub> and SR<sub>re</sub>, were shown to have better performance in LAI estimation using UAV-based multispectral imagery.

3. The cumulative SR yielded a better performance in biomass estimation using UAV-based multispectral imagery than that of all RapidEye cumulative vegetation index.

The main contributions of research in Chapter 3 is that the total nitrogen weight model could provide farmers real-time nitrogen monitoring map for farmers in wheat early growth stage in Southwestern Ontario. The nitrogen weight prediction model has a better performance from May to June at wheat BBCH stages 40-69. The yield prediction model provides a yield spatial distribution map in this study that is two month earlier than harvest season. The wheat BBCH stage 48 is the prime time to monitor wheat status for final yield prediction. Meanwhile, Chapter 3 demonstrates the application capability of calculated biomass model in winter wheat biomass estimation. This biomass calculated model provides a non-destructive ground reference biomass measurement method which avoid time-consuming process and plant damaged during the field work.

## 4.4 Possible future research

### 4.4.1 Multispectral camera

Since the UAV system could provide flexible flight performance and high temporal and spatial resolution imagery, the ground-based methods on crop status measurement may be done on UAV system to achieve more accurate results than satellite images. The advantages of the multispectral camera were demonstrated in Chapter 2. It could provide some better vegetation indices in the estimation of plant biophysical parameters. Specifically the red-edge bands in multispectral camera could provide more vegetation indices combinations. Therefore, a multispectral camera could be applied in future research on wheat and corn total nitrogen and final yield estimation. Additionally, many researchers used ground based multispectral or hyperspectral imagery to monitor crop disease and water status. By using the Tetracam, the wavelength of each band can be adjusted to the requirements of different indices, these indices derived from ground based research could be measured with the UAV system and achieved for a large area monitoring.

#### 4.4.2 Plant height and fraction of vegetation cover

The winter wheat biomass was calculated based on plant height, fCover and plant bulk density in Chapter 3. Beside the multispectral information and fractional vegetation cover derived from remote sensing data, the plant height could be achieved from photogrammetry technology in remote sensing with a UAV system. The measurements of plant height using the photogrammetry technology can be achieved by a normal digital camera which also provides fractional vegetation cover data. With the plant height and fractional vegetation cover, the biomass of different plant could be calculated using different plant bulk density. Instead of using the optical data to estimate and represent crop status, this method avoids the reflectance correction of remote sensing data and measures the volume of the crop in the field. Without the image radiometric correction, the normal digital camera makes the UAV system operation on crop monitoring is much easier for individual farms and reduces the cost of the UAV system. Moreover, this would effectively reduce the time consumption and plant destruction during ground reference data collection, providing a real-time measurement of crop biomass and help individual farmers to monitor their fields.

## Appendices

### Appendix A Temporal UAV imagery in corn field

True color UAV image of corn field in St. Isidore on June 6, 2014

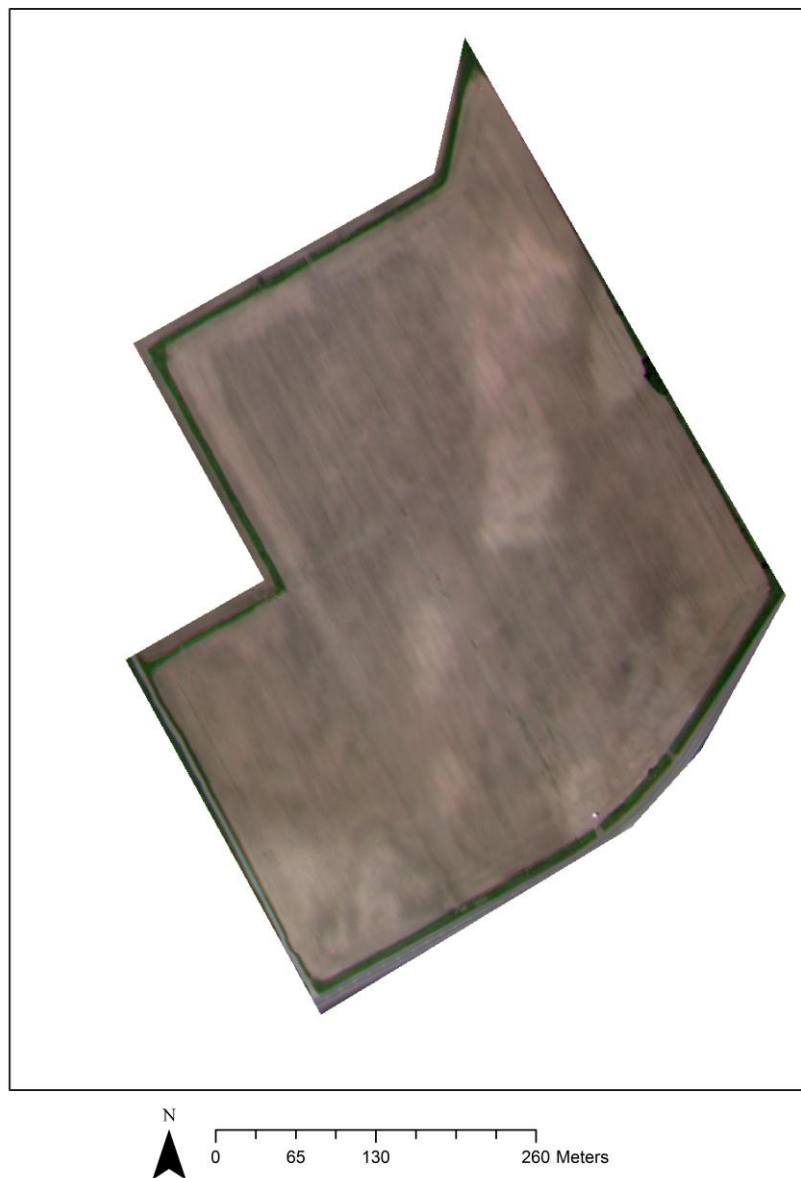


**Figure A-1 True color UAV image for corn field on June 9, 2014 in St. Isidore.**



True color UAV image of corn field in St. Isidore on June 23, 2014

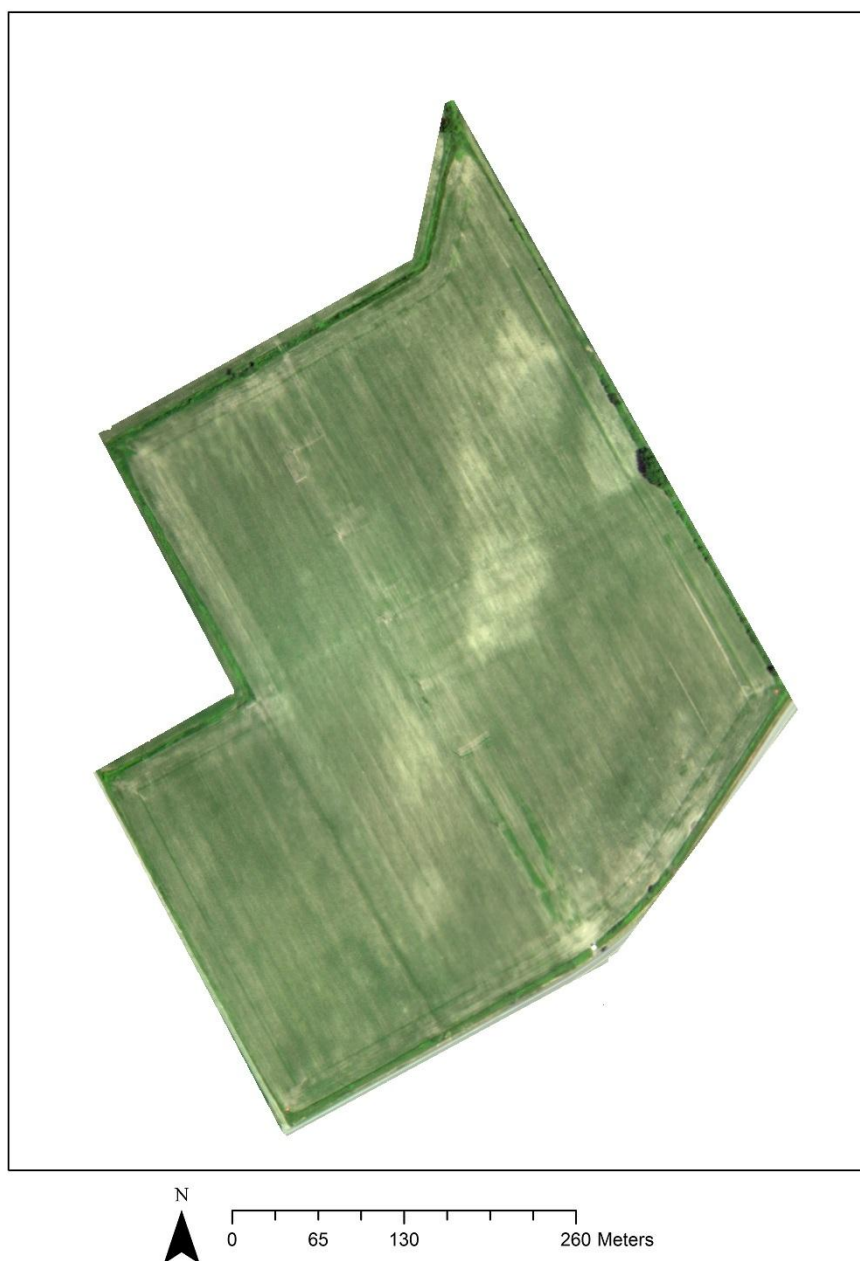


**Figure A-2 True color UAV image for corn field on June 23, 2014 in St. Isidore.**

True color UAV image of corn field in St. Isidore on July 24, 2014

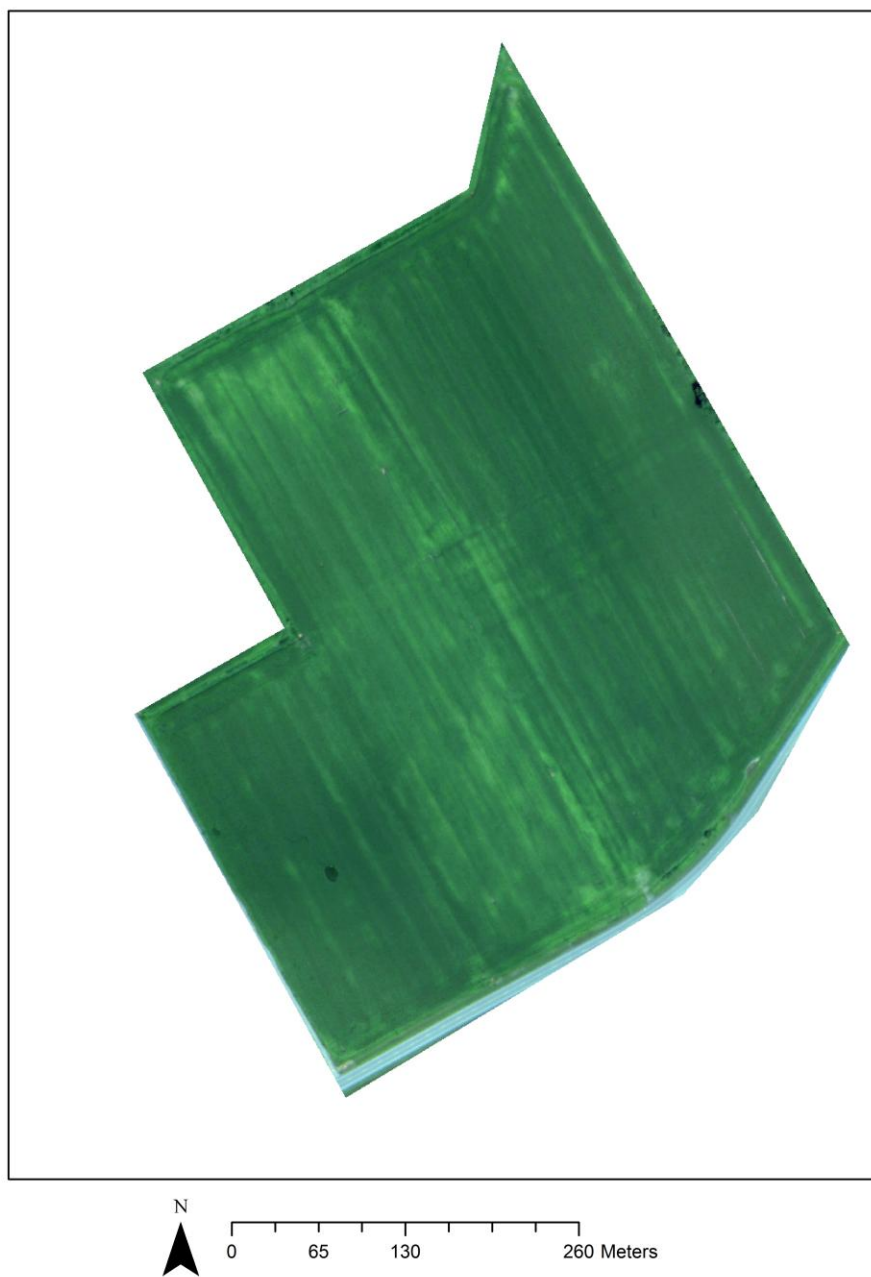


**Figure A-3 True color UAV image for corn field on July 24, 2014 in St. Isidore.**

True color RapidEye image of corn field in St. Isidore on May 31, 2014

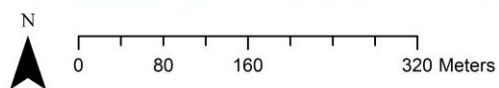


**Figure A-4 True color RapidEye image for corn field on May 31, 2014 in St. Isidore.**

True color RapidEye image of corn field in St. Isidore on June 19, 2014

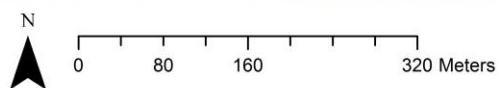


**Figure A-5 True color RapidEye image for corn field on June 19, 2014 in St. Isidore.**

True color RapidEye image of corn field in St. Isidore on July 25 , 2014

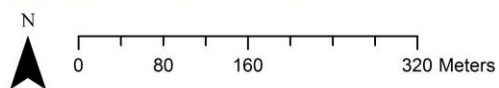
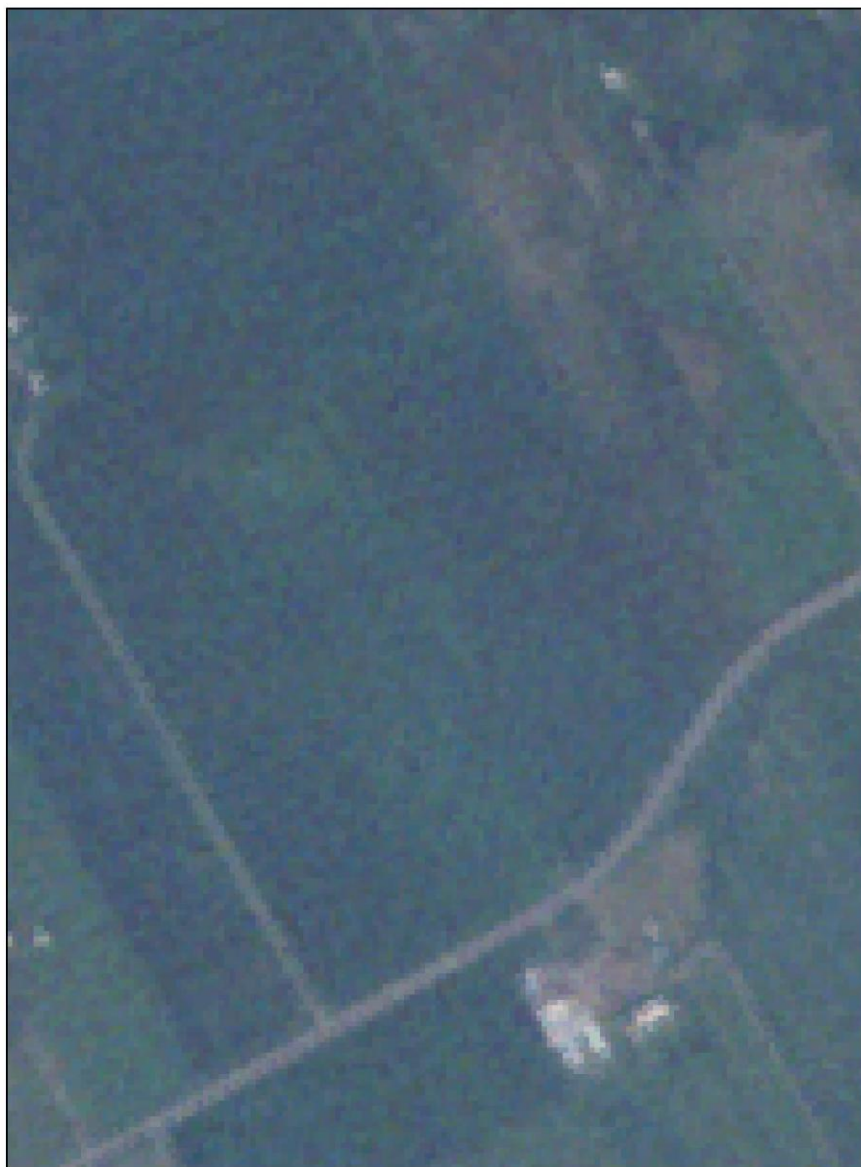


**Figure A-6 True color RapidEye image for corn field on July 25, 2014 in St. Isidore.**



## Appendix B UAV-based imagery calibration results

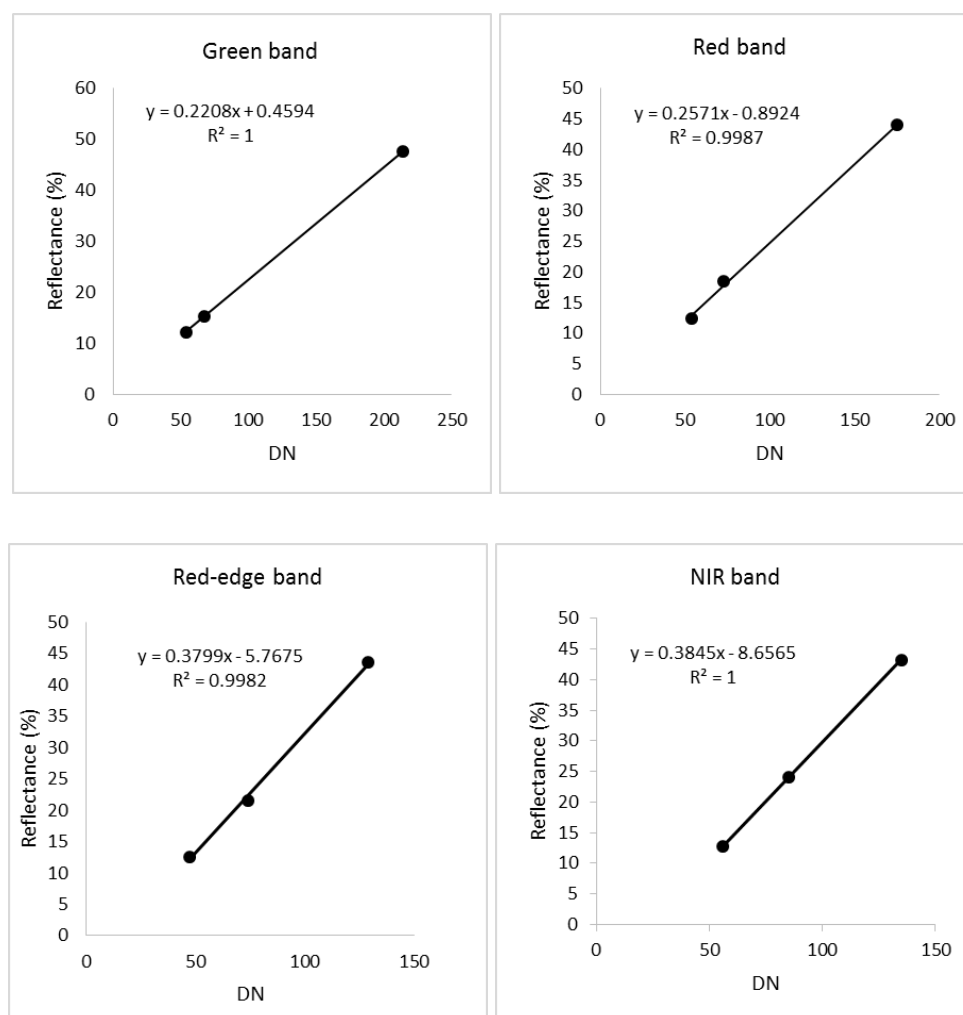


**Figure B-1 Relationship between reflectance and DNs for green, red, red-edge, and NIR band.**

By using the empirical line method to convert the UAV images from DN to reflectance, the relationship between DN and reflectance in each band had been shown above. The three reference points were asphalt road, bare soil and white tarp in the images. In green, red, red-edge and NIR bands, DN and reflectance had a simple linear correlation.

## Appendix C Cumulative Vegetation Index Theorem and Results

This theorem calculated cumulative biomass using cumulative vegetation index with logistic function was proposed by Zhang in 2003 (Zhang et al., 2003). This theorem is based on the early vegetation index distribution in a year can be fitted in a logistic function.

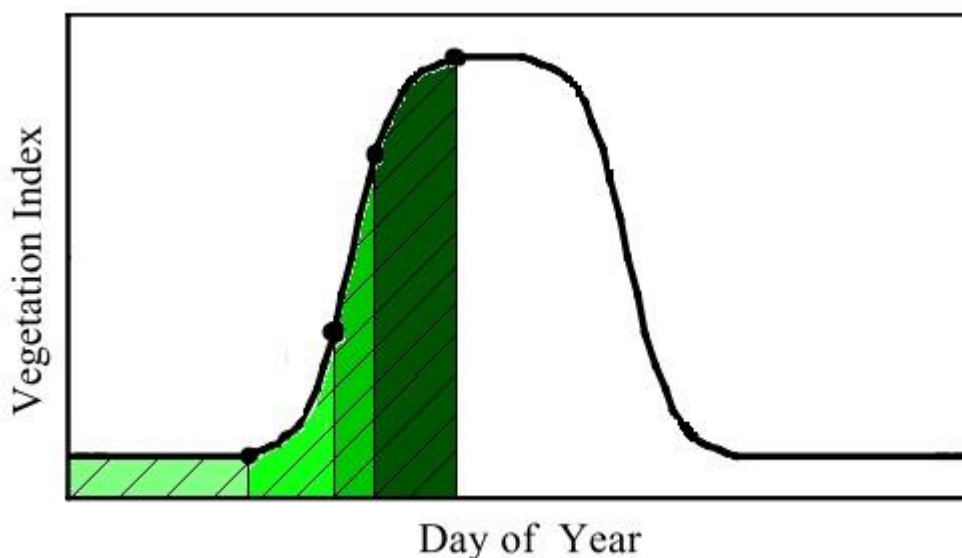


**Figure C-1 Annual vegetation index distribution curve.**

The left side of the center line, the curve represented the vegetation index distribution from emergency and mature states. The black dots are vegetation indices values. The striped area under the curve is cumulative vegetation indices values. This curve can be represented in a logistic function shown below:

$$VI(DOY) = \frac{c}{1 + e^{a + bDOY}} + d$$

where  $VI(DOY)$  is the fitted  $VI$  value at day of year ( $DOY$ ),  $a$ , and  $b$  are the fitting parameters,  $c + d$  is the maximum cumulative  $VI$  value, and  $d$  is the initial background  $VI$  value.

### Reference:

Zhang, X., Friedl, M. A., Schaaf, C. B., Strahler, A. H., Hodges, J. C. F., Gao, F., ...

Huete, A. (2003). Monitoring vegetation phenology using MODIS. *Remote Sensing of Environment*, 84(3), 471–475. [http://doi.org/10.1016/S0034-4257\(02\)00135-9](http://doi.org/10.1016/S0034-4257(02)00135-9)

## Appendix D Vegetation index and cumulative vegetation index for corn field in 2014

**Table D-1 UAV-based imagery Vegetation index values**

Date	Sample ID	UAV VI					
		NDVI	GNDVI	MTVI2	NDVIre	SR	Srre
9-Jun-16	CE_01	0.1600	0.2760	0.0970	0.0400	1.3820	1.0830
	CE_02	0.2310	0.3530	0.1960	0.0570	1.6010	1.1200
	CE_03	0.2710	0.3600	0.2850	0.0710	1.7420	1.1520
	CE_04	0.1710	0.3070	0.0900	0.0490	1.4120	1.1030
	CE_06	0.2480	0.3190	0.2760	0.0570	1.6610	1.1200
	CE_08	0.2120	0.2610	0.2550	0.0390	1.5390	1.0810
23-Jun-16	CE_01	0.5480	0.5480	0.7180	0.0770	3.9750	1.1680
	CE_02	0.5990	0.5990	0.7750	0.1380	5.0080	1.3210
	CE_03	0.5530	0.5530	0.7070	0.1200	3.9160	1.2740
	CE_04	0.5210	0.5210	0.6560	0.1010	3.3760	1.2250
	CE_06	0.5330	0.5330	0.6730	0.1010	3.5430	1.2240
	CE_08	0.5420	0.5420	0.7690	0.0710	4.3940	1.1530
24-Jul-16	CE_01	0.8400	0.7530	0.8790	0.1980	11.4880	1.4950
	CE_02	0.8740	0.8180	0.8760	0.2520	14.9200	1.6720
	CE_03	0.8510	0.7890	0.8680	0.2200	12.4430	1.5650
	CE_04	0.8840	0.8410	0.8730	0.2750	16.2060	1.7570
	CE_06	0.8380	0.7430	0.8840	0.1750	11.3750	1.4240
	CE_08	0.8580	0.7980	0.8700	0.2250	13.0820	1.5820
9-Sep-16	CE_01	0.8240	0.5980	0.9700	0.0920	10.3800	1.2030
	CE_02	0.8150	0.7760	0.8360	0.1670	9.8120	1.4010
	CE_03	0.8460	0.7180	0.9080	0.1860	12.0250	1.4580
	CE_04	0.8370	0.7510	0.8760	0.2030	11.2410	1.5090
	CE_06	0.7240	0.6820	0.7880	0.1240	6.2400	1.2830
	CE_08	0.7930	0.7130	0.8130	0.1520	8.9810	1.4590

**Table D-2 RapidEye imagery vegetation index values**

Date	Sample ID	RapidEye					
		NDVI	GNDVI	MTVI2	NDVIre	SR	Srre
9-Jun-14	CE_01	0.0900	0.1540	0.0490	0.1230	1.1970	1.2810
	CE_02	0.1120	0.1730	0.0910	0.1220	1.2520	1.2770
	CE_03	0.0890	0.1260	0.0880	0.1230	1.1950	1.2800
	CE_04	0.0890	0.1560	0.0440	0.1010	1.1950	1.2240



	CE_06	0.0610	0.1330	-0.0130	0.1300	1.1300	1.2980
	CE_08	0.0800	0.1090	0.0850	0.1090	1.1730	1.2440
23-Jun-14	CE_01	0.4460	0.3670	0.6330	0.2930	2.6090	1.8310
	CE_02	0.4880	0.4150	0.6580	0.3650	2.9060	2.1480
	CE_03	0.4730	0.3820	0.6660	0.3230	2.7950	1.9520
	CE_04	0.3950	0.3710	0.5360	0.2680	2.3080	1.7310
	CE_06	0.4090	0.3630	0.5700	0.2970	2.3850	1.8470
	CE_08	0.4800	0.4080	0.6510	0.3400	2.8450	2.0290
24-Jul-14	CE_01	0.6540	0.5540	0.7880	0.4330	4.7870	2.5280
	CE_02	0.6700	0.5760	0.7930	0.4570	5.0660	2.6800
	CE_03	0.6580	0.5710	0.7800	0.4650	4.8440	2.7350
	CE_04	0.6680	0.5690	0.7950	0.4720	5.0330	2.7890
	CE_06	0.6740	0.5600	0.8100	0.4440	5.1350	2.5970
	CE_08	0.6740	0.5810	0.7940	0.4740	5.1430	2.8020
9-Sep-14	CE_01	0.7180	0.6330	0.8120	0.4250	6.0920	2.4760
	CE_02	0.7680	0.7380	0.8010	0.5030	7.6270	3.0240
	CE_03	0.7890	0.7140	0.8420	0.5200	8.5000	3.1680
	CE_04	0.8110	0.7590	0.8390	0.5770	9.5930	3.7270
	CE_06	0.7490	0.6600	0.8310	0.4490	6.9560	2.6280
	CE_08	0.7770	0.6830	0.8490	0.4790	7.9680	2.8390

**Table D-3 UAV-imagery cumulative vegetation index values**

Date	Sample ID	UAV Cumulative Vis					
		NDVI	GNDVI	MTVI2	NDVIRE	SR	Srre
9-Jun-14	CE_01	1.1619	2.0715	0.6547	0.2138	14.0553	10.3069
	CE_02	1.5921	2.4449	1.1431	0.3319	13.2811	10.5936
	CE_03	1.7947	2.3872	1.6192	0.4036	14.5269	10.8097
	CE_04	1.2371	2.2622	0.6881	0.2275	12.8300	10.3307
	CE_06	1.5371	2.1925	1.7710	0.3506	14.3558	10.7659
	CE_08	1.4111	1.8959	1.4786	0.1590	13.0588	10.2690
23-Jun-14	CE_01	5.7443	7.8037	5.6450	1.0127	50.3515	25.7910
	CE_02	7.2836	8.9911	8.2417	1.6160	47.4704	27.4778
	CE_03	7.3748	8.6339	8.6646	1.6185	51.1677	27.5495
	CE_04	5.6524	7.8575	4.9426	1.1798	39.8821	26.0125
	CE_06	6.8290	9.0272	8.3947	1.3623	48.1282	26.9981
	CE_08	6.4420	7.3142	8.9239	0.8461	47.6975	25.5322
24-Jul-14	CE_01	30.3802	28.6549	33.3579	5.6426	301.8433	68.0564
	CE_02	31.9051	32.3859	34.7153	8.3291	411.6353	75.3305
	CE_03	30.8676	30.4885	35.0714	7.3637	321.6148	71.9679
	CE_04	29.8193	30.1024	31.2178	7.4777	416.9493	74.0721
	CE_06	29.8000	28.8702	33.3245	5.9839	288.6613	67.9091

	CE_08	30.1197	29.8485	35.4049	5.8098	372.6998	69.2274
9-Sep-14	CE_01	71.0655	59.8620	73.8368	14.2355	854.0733	134.0768
	CE_02	72.3756	68.2272	72.7620	19.8747	1004.1000	150.3733
	CE_03	71.2219	64.3253	74.1706	17.8349	907.0049	145.1810
	CE_04	70.5210	65.7979	69.7159	19.4263	1131.4000	148.8691
	CE_06	69.4358	60.9860	70.2327	14.4069	832.7562	136.9263
	CE_08	70.1623	67.5246	73.6409	15.5936	947.8225	139.1617

**Table D-4 RapidEye imagery cumulative vegetation index values**

Date	Sample ID	RapidEye Cumulated VI					
		NDVI	GNDVI	MTVI2	NDVire	SR	SRre
31-May-14	CE_01	0.6144	1.4254	0.3801	1.0888	11.1672	11.5228
	CE_02	0.9940	1.6967	0.8114	1.0840	12.4351	11.8226
	CE_03	0.7416	1.2426	0.7382	1.0863	11.5932	11.7812
	CE_04	0.6993	1.4970	0.3687	0.9588	11.0992	11.1417
	CE_06	0.5417	1.1755	-0.0469	1.1094	10.7532	11.6272
	CE_08	0.6536	0.9226	0.7300	0.9241	11.3716	11.1708
19-Jun-14	CE_01	4.3271	5.1226	3.7687	3.5107	38.2513	30.9913
	CE_02	3.8817	5.9238	4.0661	3.7075	43.0505	36.0759
	CE_03	3.6529	4.9024	4.6732	3.5967	40.4024	34.6824
	CE_04	3.8188	5.2896	2.8166	3.5926	36.0891	31.9265
	CE_06	2.4265	3.9973	2.9845	3.7548	36.0351	31.8176
	CE_08	3.5320	3.7959	0.4288	3.5561	40.4265	31.1575
25-Jul-14	CE_01	23.8516	20.0472	28.1032	16.2804	152.6934	106.4862
	CE_02	25.3393	21.1539	28.5155	18.2628	165.4867	112.8375
	CE_03	25.2619	19.7197	29.4267	18.1978	154.9695	107.7526
	CE_04	20.1413	19.7314	27.2961	15.1852	144.7499	100.8133
	CE_06	23.6214	22.1451	27.4287	16.8100	134.1870	109.3346
	CE_08	25.0994	22.4311	29.3153	17.7652	161.4435	115.9912
9-Sep-14	CE_01	54.5088	46.7825	63.2971	35.1520	400.8264	216.5742
	CE_02	56.7113	40.9588	63.5835	39.3740	453.6348	240.8751
	CE_03	57.3405	48.9725	65.1103	39.8590	448.7985	240.8046
	CE_04	53.6577	49.8607	63.2436	39.0626	473.5131	248.9617
	CE_06	54.9173	48.9719	63.5368	36.4512	380.4456	224.2625
	CE_08	57.0306	50.2447	65.4574	38.7324	457.5197	240.1152

## Appendix E Ground reference data

**Table E-1 Corn field ground reference data, LAI, average height and biomass, in 2014**

Date	Site	LAI (m <sup>2</sup> /m <sup>2</sup> )	Average height (cm)	Biomass (g/m <sup>2</sup> )
9-Jun-14	CE01	0.14	30.20	12.67
	CE02	0.10	35.80	13.33
	CE03	0.01	35.80	15.33
	CE04	0.04	32.60	11.33
	CE06	0.01	29.40	10.00
	CE08	0.19	34.20	18.00
23-Jun-14	CE01	0.62	70.00	124.00
	CE02	1.03	71.60	118.67
	CE03	1.03	80.40	120.67
	CE04	0.69	62.00	87.33
	CE06	0.94	65.80	88.00
	CE08	1.24	87.80	167.33
24-Jul-14	CE01	3.12	278.40	1113.33
	CE02	4.39	294.40	718.00
	CE03	3.46	288.20	676.67
	CE04	4.65	302.60	698.00
	CE06	4.39	276.20	540.67
	CE08	3.82	292.80	857.33
9-Sep-14	CE01	-	-	1356.00
	CE02	-	-	1245.33
	CE03	-	-	1847.33
	CE04	-	-	1570.00
	CE06	-	-	1186.00
	CE08	-	-	1576.00

**Table E-2 Wheat ground reference data, PAI and average height, vegetation cover fraction and nitrogen content in 2015**

Date	Sample ID	Average height (cm)	fcover (%)	PAI (m <sup>2</sup> /m <sup>2</sup> )	Nitrogen (%)
19-May-15	W33-09	0.32	6.50	0.31	5.32
	W33-08	0.35	-	0.21	5.51
	W33-07	0.34	19.30	0.41	5.17
	W33-06	0.33	12.50	0.51	4.96

		W33-05	0.36	14.80	0.38	5.14
		W33-04	0.35	11.00	0.38	5.35
		W33-03	0.30	10.93	0.16	5.15
		W33-02	0.40	12.20	0.40	5.22
		W115-14	0.26	28.30	0.51	4.37
		W115-13	0.27	25.70	0.48	5.16
		W115-12	0.29	20.60	0.57	5.15
		W115-11	0.31	26.70	0.56	5.20
		W115-10	0.29	18.50	0.46	5.22
		W115-09	0.33	31.00	0.65	5.28
		W115-08	0.35	27.40	0.73	5.57
		W115-07	0.30	22.40	0.60	5.46
		W112-15	0.30	42.10	0.80	5.19
		W112-14	0.33	27.70	0.60	5.04
		W112-13	0.32	24.60	0.89	5.33
		W112-12	0.32	28.50	0.72	4.80
		W112-11	0.35	33.20	0.73	5.03
		W112-10	0.30	29.20	0.63	5.30
		W112-09	0.30	29.90	0.79	4.84
		W112-04	0.32	27.50	0.73	5.02
		W108-08	0.40	23.50	0.75	4.49
		W108-07	0.41	35.50	0.80	4.99
		W108-06	0.45	30.40	0.57	4.90
		W108-05	0.43	35.00	0.61	5.17
		W108-04	0.43	44.40	0.85	5.93
		W108-03	0.42	22.40	0.48	4.36
		W108-02	0.39	25.30	0.39	4.95
		W108-01	0.40	8.10	0.34	4.85
	29-May-15	W33-10	0.30	12.80	0.36	5.15
		W33-09	0.27	13.60	0.52	4.91
		W33-08	0.29	-	0.29	4.93
		W33-07	0.36	29.10	0.91	5.09
		W33-06	0.37	25.90	0.90	4.57
		W33-05	0.30	25.10	0.51	4.85
		W33-04	0.36	27.90	0.75	5.22
		W33-03	0.43	31.10	0.76	4.73
		W33-02	0.35	26.80	0.83	4.83
		W115-14	0.41	23.50	0.60	4.66
		W115-13	0.31	38.30	0.67	5.00
		W115-12	0.31	42.90	0.84	4.92
		W115-11	0.35	44.70	0.58	5.14

	W115-10	0.36	38.10	0.61	5.02
	W115-09	0.39	36.80	0.64	5.11
	W115-08	0.39	38.00	0.70	4.96
	W115-07	0.35	43.00	0.77	5.10
	W112-15	0.40	33.20	0.80	4.44
	W112-14	0.43	38.30	0.60	4.73
	W112-13	0.49	19.80	0.89	4.92
	W112-12	0.42	20.40	0.72	4.36
	W112-11	0.41	22.40	0.73	4.65
	W112-10	0.42	12.50	0.63	4.98
	W112-09	0.35	23.50	0.79	4.66
	W108-08	0.55	27.50	1.27	4.58
	W108-07	0.56	21.10	1.09	4.73
	W108-06	0.58	23.30	1.11	4.58
	W108-05	0.45	22.80	0.98	4.18
	W108-04	0.50	23.50	0.96	4.90
	W108-03	0.59	25.60	1.04	4.39
	W108-02	0.50	24.70	0.98	4.50
	W108-01	0.55	32.70	0.74	4.35
	19-Jun-15	W33-10	0.49	48.30	1.30
W33-09		0.60	39.80	1.20	4.67
W33-08		0.56	30.30	0.75	4.55
W33-07		0.53	42.10	1.18	3.42
W33-06		0.57	42.70	1.14	3.08
W33-05		0.56	35.20	1.02	4.62
W33-04		0.58	50.00	1.38	4.27
W33-02		0.60	46.90	1.12	4.12
W33-01		0.58	44.80	1.23	4.14
W112-15		0.94	54.10	1.53	4.71
W112-14		0.91	48.40	1.18	4.50
W112-11		0.92	42.00	0.54	4.29
W112-10		0.78	53.70	1.85	4.16
W112-09		0.83	51.50	1.50	4.37
W112-04		0.90	47.10	1.43	4.45
W108-08		0.77	45.90	1.34	3.98
W108-07		0.85	43.70	1.95	4.15
W108-06		0.86	57.70	1.48	4.01
W108-05		0.60	50.40	1.13	3.96
W108-04		0.86	41.50	1.39	4.23
W108-03	0.81	39.90	1.07	4.07	
W108-02	0.77	49.20	1.07	3.73	

		W108-01	0.75	41.60	1.02	3.57
		W115-12	0.81	64.40	1.01	3.72
		W115-11	0.81	44.80	1.57	3.47
		W115-10	0.75	66.00	1.50	3.31
		W115-09	0.75	61.00	1.12	3.90
		W115-08	0.79	50.90	0.88	3.95
		W115-07	0.87	45.20	1.57	3.89
	2-Jul-15	W33-10	0.42	76.80	0.72	3.84
		W33-09	0.63	19.10	0.91	3.74
		W33-08	0.55	31.10	0.75	3.28
		W33-06	0.57	37.50	1.21	2.90
		W33-05	0.52	42.70	0.95	3.31
		W33-04	0.53	28.20	1.67	3.42
		W33-02	0.53	35.60	1.29	3.46
		W112-15	0.94	67.00	1.39	4.05
		W112-14	0.91	36.20	1.52	3.59
		W112-11	0.92	24.00	0.85	3.88
		W112-10	0.78	7.50	1.14	3.60
		W112-09	0.83	31.50	1.23	3.29
		W112-04	0.90	36.30	1.52	3.31

**Table E-3 Ground reference biomass for wheat fields in 2015**

Date	Sample ID	Biomass (g/m <sup>2</sup> )	Height (cm)	PAI (m <sup>2</sup> /m <sup>2</sup> )	PAI*H/100	fCover (%)	fCover*H/100
21-May-15	W33	132.00	35.00	0.37	0.13	13.46	4.71
	W08	326.00	60.00	0.60	0.36	28.08	16.85
	W115	169.00	73.00	0.74	0.54	30.34	22.15
	W112	109.00	30.00	0.57	0.17	25.08	7.52
19-Jun-15	W33	276.44	41.30	1.14	0.47	42.23	17.44
	W112	600.22	71.30	1.30	0.93	46.29	33.00
	W115	679.00	58.30	1.34	0.78	49.47	28.84
	W108	669.33	73.30	1.28	0.93	44.00	32.25
2-Jul-15	W108	1014.62	90.00	1.52	1.37	53.60	48.24
	W115	884.04	89.00	1.53	1.36	54.20	48.24
	W110	929.00	94.00	1.64	1.54	54.00	50.76
	W33	588.29	93.00	1.39	1.29	36.20	33.67
	W108	1017.14	86.00	2.00	1.72	67.00	57.62
	W115	1003.47	87.00	1.99	1.73	65.00	56.55
	W112	711.88	81.00	1.12	0.91	44.80	36.29
	W33	572.36	81.00	1.12	0.91	44.80	36.29

## Appendix F UAV system and ground station

The UAV-based imagery data were collected by a fixed wing UAV that was developed by A&L Canada Inc. to collect images for entire fields. This UAV has a maximum 500g payload and 40 minutes flight time. The maximum coverage of this UAV will depend on the flight height.



**Figure F-1 Fixed wing UAV for image collection in this study.**



The UAV was controlled to follow a pre-programmed flight route generated by the ground station software Mission Planner. All UAV flight parameters are shown in the software to help the operator control the UAV. The route can be setup based on the field size and image overlap requirement. As Figure G-3 shows, different image capture density was operated at the same field to achieve different image overlap.



**Figure F-2 Control panel of the Mission Planner software.**



**Figure F-3 Different flight path showed at the same field.**



## Appendix G Temporal UAV-based blue-green-NIR imagery processing

The UAV-based blue-green-NIR images were processed in the images mosaicking software Agisoft. All images have geo-tags which help to ensure the geometric accuracy of the final image. After the image mosaicking, the final blue-green-NIR image can be exported as a tiff file which can be processed in ENVI or ArcGIS, the resolution of the final image can be achieved as high as 10 center meters. The final mosaicked images for the wheat field are shown in Figure G 2-5.

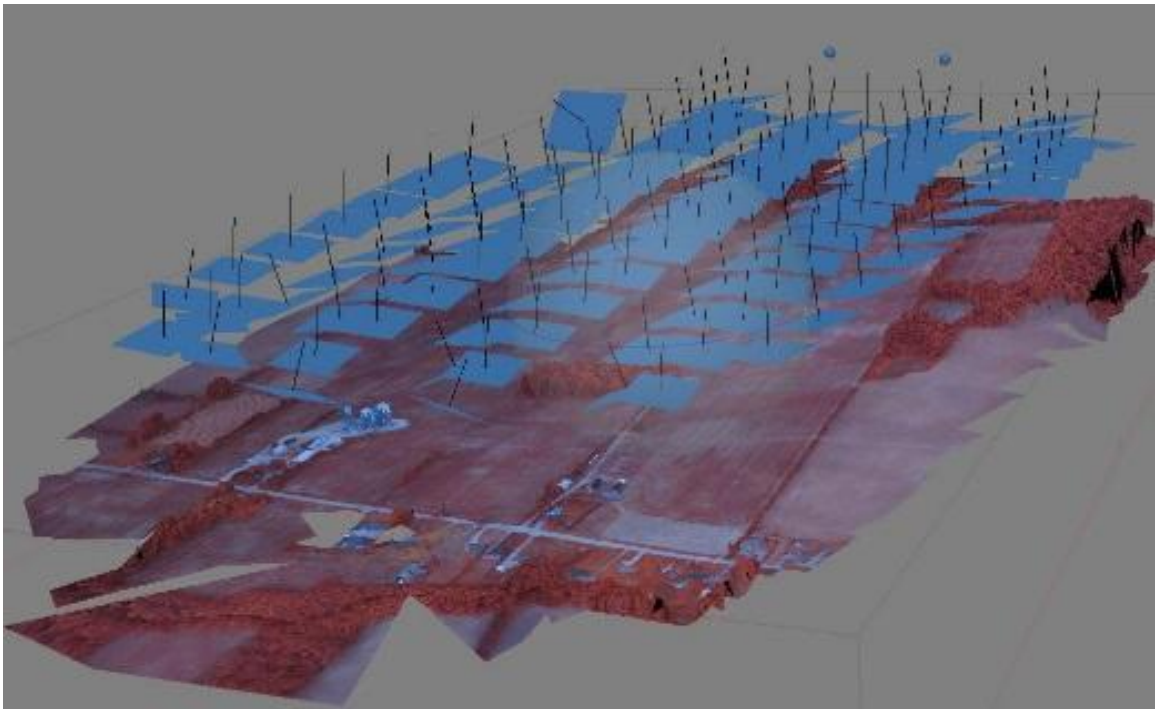


**Figure G-1 UAV-based images processing in Agisoft.**

UAV-based blue-green-NIR imagery for wheat field 118 on May 21, 2015

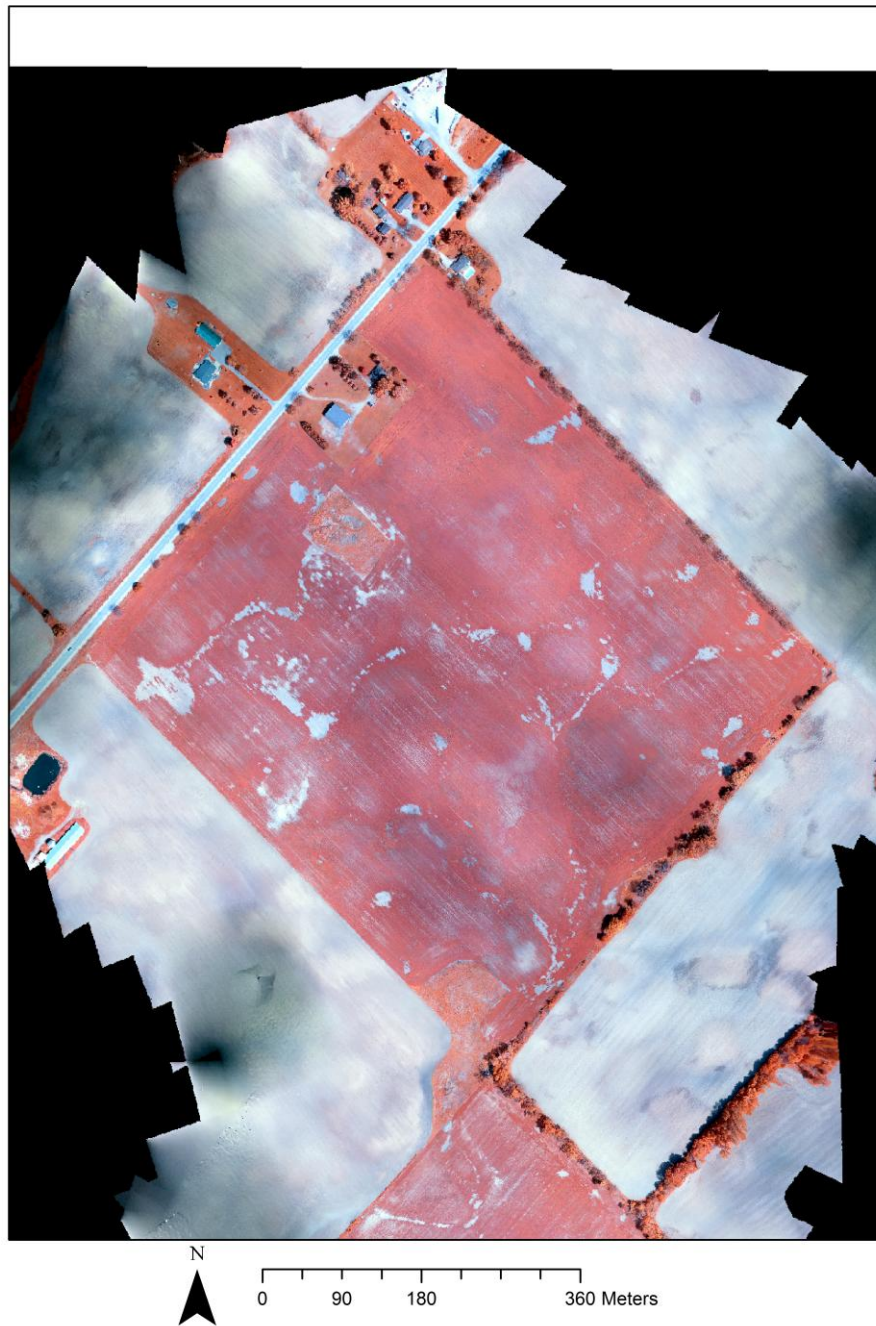


**Figure G-2 UAV-based blue-green-NIR imagery on May 21, 2015**

UAV-based blue-green-NIR imagery for wheat field 118 on May 29, 2015

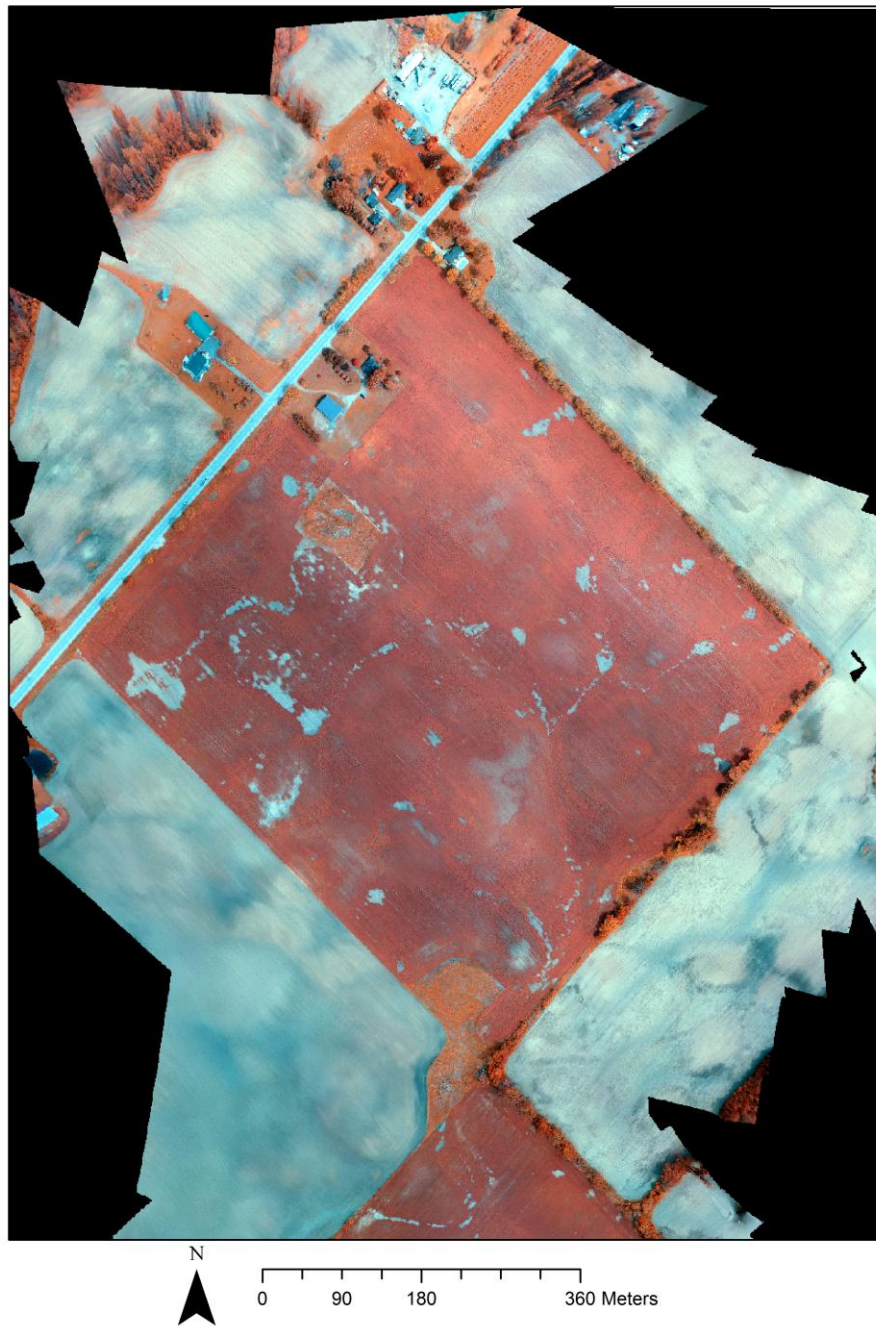


**Figure G-3 UAV-based blue-green-NIR imagery on May 29, 2015**



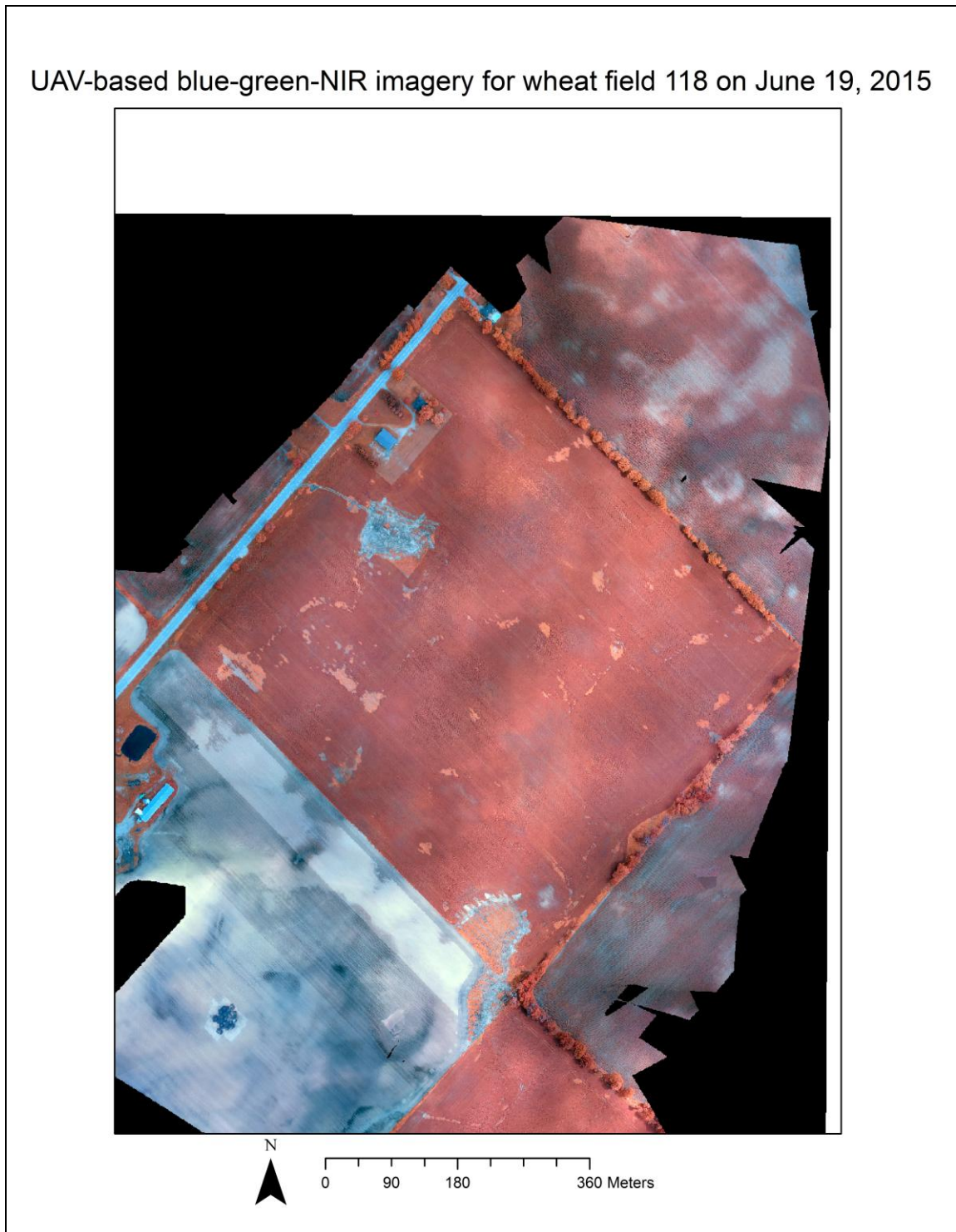


**Figure G-4 UAV-based blue-green-NIR imagery on June 19, 2015**

UAV-based blue-green-NIR imagery for wheat field 118 on July 2, 2015

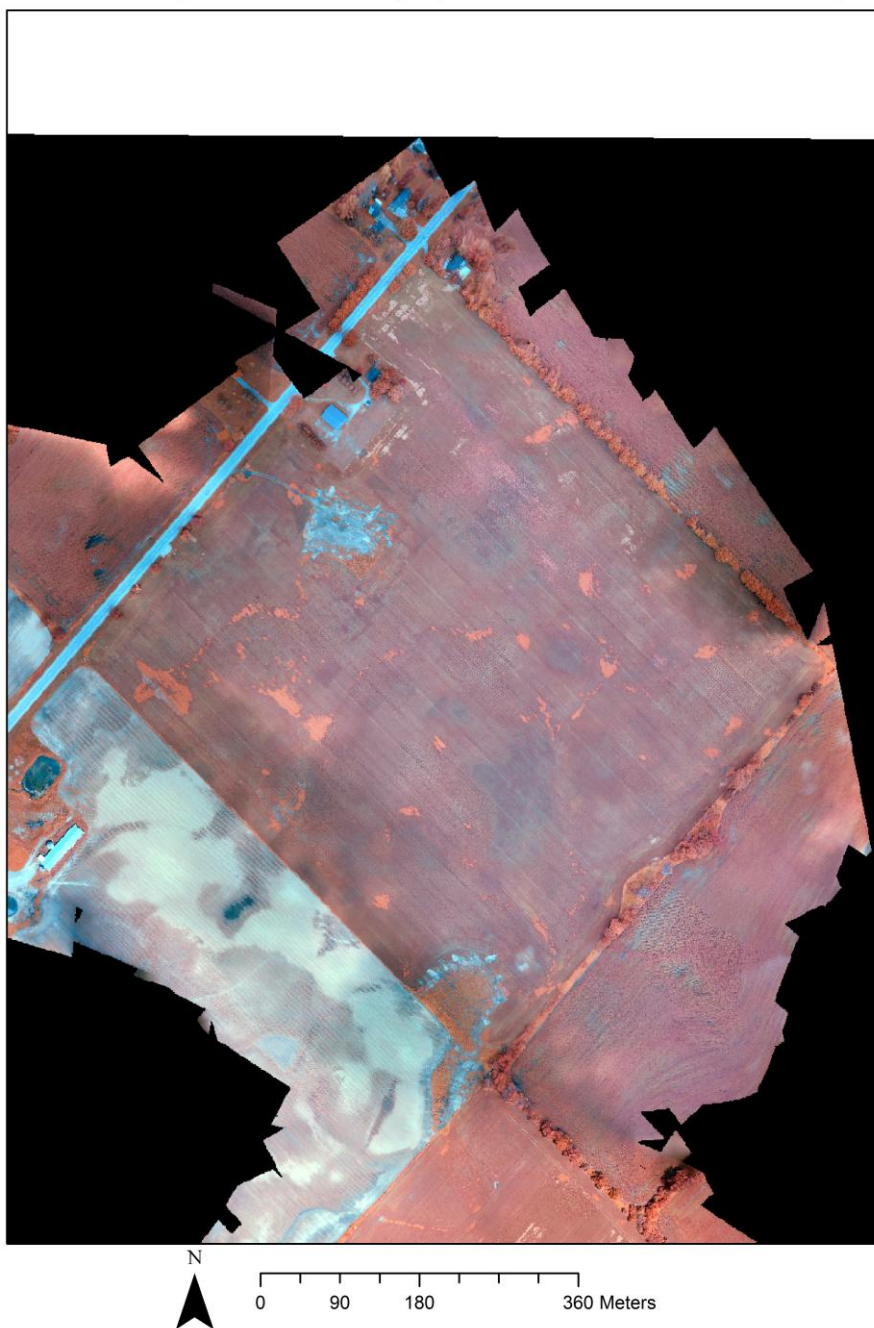


**Figure G-5 UAV-based blue-green-NIR imagery on July 2, 2015**

# Curriculum Vitae

**Name:** Yang Song

<b>Post-secondary Education and Degrees:</b>	Fanshawe College London, Ontario, Canada 2005-2008.
--	---

Royal Roads University  
Victoria, BC, Canada  
2012-2014 B.Sc.

The University of Western Ontario  
London, Ontario, Canada  
2014-2016 M.Sc.

<b>Honors and Awards:</b>	Western Graduate Research Scholarship 2014-2016
---------------------------	--

<b>Related Work Experience:</b>	Teaching Assistant	Undergraduate Courses
	Spatial Techniques; Geographic Information Science I; Ontario and Great Lake; Geography of Tourism.	
	The University of Western Ontario, Department of Geography	
	2014-2016	

Research Assistant NSERC-Engage Project  
 Estimation of Intra-field Winter Wheat Nitrogen Weight and Yield  
 Using UAV-Based Imagery  
 The University of Western Ontario, Department of Geography  
 2014-2016

Technician  
Agricultural sample analysis, field GIS information collection, field  
GIS report writing and analysis  
A&L Canada Laboratories Inc.  
2009-2014

<b>Conference</b>	Yang Song and Jinfei Wang, Soybean canopy Nitrogen monitoring
<b>Paper:</b>	and prediction using ground based multispectral remote sensing data. Proceedings of IEEE Geoscience and Remote Sensing Symposium (IGARSS) 2016, July 10-15, 2016, Beijing, China. 4 p.